공학박사 학위논문

Abatement of nitrogen oxide and light hydrocarbon emissions at low-temperature over Pd/Ce-based catalysts

Pd/Ce 기반 촉매에서 질소산화물 및 경질 탄화수소의 저온 배출 저감

2023년 2월

서울대학교 대학원

화학생물공학부

황 성 하

Abatement of nitrogen oxide and light hydrocarbon emissions at low-temperature over Pd/Ce-based catalysts

지도 교수 김 도 희

이 논문을 공학박사 학위논문으로 제출함
2023년 1월

서울대학교 대학원
화학생물공학부
황 성 하

황성하의 공학박사 학위논문을 인준함
2023년 1월

위 원 장 _____ 이 원 보 _____ (인)

부위원장 _____ 김 도 희 _____ (인)

위 원 _____ 강 종 헌 _____ (인)

위 원 _____ 김 지 만 _____ (인)

위 원 _____ 박 영 권 _____ (인)

Abstract

Abatement of nitrogen oxide and light hydrocarbon emissions at low-temperature over Pd/Ce-based catalysts

Sungha Hwang
School of Chemical and Biological Engineering
The Graduate School
Seoul National University

The abatement of pollutants in the exhaust gas is one of the most important social challenges. Accordingly, regulations related to exhaust gas emissions are being strengthened globally. After-treatment catalytic conversion technologies have been developed and widely used to meet these stringent regulations. Typically, catalytic converters such as three-way catalysts (TWC) are used in gasoline engine after-treatment systems. On the other hand, diesel oxidation catalysts (DOC) and selective catalytic reduction (SCR) catalysts are applied in the diesel engine after-treatment system. However, for these systems to operate properly, a temperature above a certain level (typically 200 °C) must be maintained. Therefore, when the vehicle is first started at room temperature, many pollutants, including NOx and hydrocarbons that did not undergo catalytic conversion, are released,

resulting in cold-start emissions.

Passive NOx adsorbers (PNAs) have been suggested as promising catalytic technologies for solving the problem of NOx emission during the cold start period in diesel engine operation. PNA can adsorb NOx at low temperatures and release NOx at high temperatures, allowing downstream catalytic converters to function correctly. Similarly, developing low-temperature hydrocarbon traps based on zeolite is being actively carried out. However, most of the research targets diesel engine applications. Since gasoline engine exhaust gas differs from diesel in many ways, such as operating method, temperature, and gas composition, it is not easy to effectively utilize zeolite-based hydrocarbon traps in terms of durability, and it is necessary to develop a new catalyst for gasoline engine application.

At first, the promoting effect of CO on the NOx adsorption ability of Pd/CeO_2 at low temperatures was investigated. The amount of NOx adsorbed significantly increased when CO was added to the feed gas. Specifically, during the first 10 min, the amount of adsorbed NOx increased more than six times in the presence of CO. A mechanism for the promoting effect of CO on low-temperature NOx adsorption was suggested by considering the decreased CO oxidation ability with the increasing amount of NOx adsorbed over Pd/CeO_2. The model proposes that NOx was readily adsorbed by the oxygen vacancies (V_Os) of CeO_2 adjacent to the Pd particles, which were generated during CO oxidation, increasing NOx adsorption. A

better understanding of the CO and NO interactions would contribute to developing ceria-based low-temperature NOx adsorption materials.

Next, a CeO_2-supported Pd catalyst was devised to achieve nearly zero NO emissions from gasoline vehicles. A significant amount of NO is emitted from advanced gasoline vehicles during preheating TWCs to operating temperature (>200 °C). Pd nanoparticles (NPs) loaded on CeO_2 are studied as a NO abatement material to mitigate NO emissions during the cold-start period. The air-fuel equivalence ratio is systematically switched from high to low while increasing temperature to promote NO storage below the operating temperature of TWCs and NO reduction at high temperature. Combined experimental and theoretical studies indicate that the Pd-NP–CeO_2 interface modified by V_Os plays an essential role in converting NO* to NO_2. NO_2 is captured by V_Os formed on the CeO_2 surface, enabling Pd/CeO_2 as a NO storage material. Consequently, NO emission decreases by 67.6% during the cold-start period under practical conditions, which has been unattainable with conventional TWCs, thus bringing us a step closer to zero harmful emissions.

Lastly, the possibility of applying Pd/CeO_2 to reduce the low-temperature propene emission for gasoline engines is studied to deal with future regulations on unburned light hydrocarbons. Propene is one of the most representative unburned hydrocarbons in gasoline engine exhaust gas. A mechanism for the propene adsorption on Pd/CeO_2 surface was carefully

suggested by considering experimental and characterization data. Furthermore, the thermal stability was improved by introducing Ce–Zr mixed oxide. Due to the characteristics of the trap located right after the engine, high thermal stability is required.

In this thesis, the Pd/CeO_2 catalyst was used to effectively store NOx and propene at low temperatures, and the roles of Pd and CeO_2 were established. Furthermore, based on these findings, a catalyst with better thermal stability and stability under a reducing atmosphere at high temperatures was designed. This study is expected to contribute to developing next-generation after-treatment systems dealing with low-temperature emissions.

Keywords: Nitrogen oxides; Light hydrocarbon; Pd/CeO_2; Cold-start emission; Adsorption site; After-treatment system

Student Number: 2017-28948

Contents

List of Tables

List of Figures

Chapter 1. Introduction

1.1. Emission standards and cold-start emissions

Concerns about environmental pollution from automobile emissions have led governments worldwide to tighten emission regulations for decades [1-3]. As a result, the automobile industry is striving to develop advanced after-treatment systems, including three-way catalysts (TWC) for gasoline engine vehicles, diesel oxidation catalysts (DOC), and selective catalytic reduction (SCR) for diesel engine vehicles [4]. However, although state-of-the-art catalytic converters can convert NO into N_2 and hydrocarbons (HCs) into H_2O and CO_2 at temperatures above 200 ˚C, stringent emission regulations do not allow pollutant emissions below 200 ˚C during the cold-start period [5]. Recently, studies on the removal of NO emitted during the cold-start of diesel vehicles have been actively conducted, but reflections for removing NO emitted during the cold-start period of gasoline vehicles have hardly been achieved [6].

TWC technology has been used in gasoline engine vehicles for over 50 years and has successfully met stringent emission standards by eliminating NO, CO, and HCs above 400 °C with nearly 100% conversion efficiencies [7, 8]. The emission temperature of conventional gasoline engines quickly exceeds 500 °C [9]. However, the time required to heat the

TWC to operating temperatures is significantly prolonged in gasoline vehicles, with downsized engines and turbochargers exhibiting improved fuel economy [10, 11]. In hybrid cars, the cold-start period is also extended with frequent shutdowns and startups. Accordingly, developing low-temperature NOx and HC abatement technology that can operate under gasoline exhaust gas conditions has become more critical.

1.2. Current status of low-temperature NOx and hydrocarbon control technology

Passive NOx adsorbers (PNAs) have been suggested as promising catalytic technologies for solving the problem of NOx emission during the cold start period in diesel vehicle applications. The concept that NOx is adsorbed on sorbent materials during the warm-up period of catalytic converters was first introduced in 1997 [12]. Since then, with tightening exhaust gas regulations, several pieces of research have been conducted to develop PNA materials. Platinum group metals (PGM) supported on metal oxides have been reported as candidate materials for PNA application [13, 14]. In addition, Pd/zeolites have also recently attracted attention due to their applicability as PNA materials [15, 16]. However, Pd/zeolite cannot be applied in engine vehicles due to reductive exhaust gas conditions containing high concentrations of reductants (e.g., CO, H_2, and HCs) [17].

The isolated Pd^{2+} sites, NO_x storage sites, is susceptible to the such reductive condition [18]. Such deactivation originated from the irreversible agglomeration of the isolated Pd^{2+} ions into Pd particles. As a result, Pd/CeO_2 is suggested in this study.

A technology to capture hydrocarbons at low temperatures is being studied for low-temperature HC abatement, similar to the NOx abatement case [19]. HC traps have been successfully applied in diesel engine vehicles due to their lean operating conditions and the ability to adsorb heavy molecules highly [5]. Beta and ZSM-5 are the most effective zeolites for trapping C_6 and higher HCs [20, 21]. However, current traps release the light HCs at temperatures far below the light-off (150 ˚C vs. 250–300 ˚C) [5]. In addition, zeolite-based HC traps are not stable at the high temperatures experienced in gasoline vehicles.

1.3. Objectives

The composition of exhaust gas consists of very complex components. In order to design a catalyst working under practical conditions, it is essential to understand the role of each catalyst component material and its interaction with exhaust gas components. As the role of Pd and CeO_2 in NOx adsorption under the presence of reductants has not yet been clearly established, it was not easy to rationally design a low-temperature NOx and

HC abatement catalyst for gasoline vehicle application. In this respect, this thesis mainly consists of understanding the role of Pd and CeO_2 as NOx storage materials and the NOx and HC adsorption mechanisms. Chapter 2 investigates the NOx adsorption ability of Pd/CeO_2 in the presence and absence of CO and the role of Pd and CeO_2. Based on the result in Chapter 2, Pd/CeO_2 was applied for gasoline engine application. Understanding the NOx adsorption mechanism and identifying the NOx adsorption site was focused on in Chapter 3. Finally, in Chapter 4, the propene adsorption ability of Pd/CeO_2 was investigated, and Ce-Zr mixed oxide was also investigated to overcome the deactivation at high temperatures. Throughout this thesis, a fundamental understanding of Pd/CeO_2 as NOx and C_3H_6 adsorber was provided. It is believed that Pd/Ce-based materials can be a potential material for NOx and C_3H_6 storage.

Chapter 2. Promoting effect of CO on low-temperature NOx adsorption

2.1. Introduction

Regulation of NOx emissions from different sources, mainly vehicles, are increasingly stringent because of growing human health and environmental concerns. Several catalytic converters have been developed to meet emission regulations [3, 5, 23]. In particular, diesel vehicles are equipped with after-treatment systems, such as the ammonia selective catalytic reduction (SCR) systems to reduce NOx emissions. State-of-the-art SCR catalysts effectively remove NOx during driving, although some challenges remain, including cold-start emissions [24]. SCR catalysts typically require temperatures above 200 °C to operate properly [6]. Below 200 °C, the decomposition of urea that supplies ammonia or catalytic reaction is not fully active [25, 26]. Therefore, when vehicles are first started at room temperature, a large amount of NOx that did not undergo catalytic conversion is released, resulting in cold-start emissions [6]. Passive NOx adsorbers (PNA) have been proposed to resolve cold-start emissions [14, 27, 28]. PNAs adsorb NOx at temperatures below 200 °C and release

[#] This chapter cites the author's published journal article: S. Hwang, Y. Kim, J. Lee, E. Lee, H. Lee, C. Jeong, C. H. Kim, and D. H. Kim, "Promoting effect of CO on low-temperature NOx adsorption over Pd/CeO_2 catalyst", Catalysis Today, 384-386 (2022) 88-96 [22].

them at high temperatures, and then downstream catalysts can convert the released NOx into N_2 [6, 29].

Pd-impregnated metal oxides and zeolites are the most active PNA materials [19, 29]. Pd/zeolites have attracted increasing attention because of their resistance to sulfur, and many studies have been conducted to improve their intrinsic NOx adsorption ability [16, 30, 31]. Pd-impregnated metal oxides, especially ceria-based metal oxides, exhibit PNA ability and demonstrate excellent oxidation ability and hydrothermal stability [13]. It has previously reported the differences in the NOx adsorption and desorption behaviors of Pd/CeO_2 and Pd/SSZ-13 and demonstrated that these two catalysts could perform the same NOx adsorption function but differed in their adsorption sites or mechanisms [32].

Recently, many studies have examined the effects of other exhaust gas components on low-temperature NOx adsorption over Pd/zeolite catalysts. In particular, several groups have reported that the presence of CO improved the NOx adsorption ability of Pd/zeolite [33-36]. Vu et al. [35] reported that CO increased the amount of NOx adsorbed over Pd/BEA at low temperatures and induced desorption at higher temperatures by lowering the oxidation state of Pd. Khivantsev et al. [33] reported that CO increased the NOx adsorption ability of Pd/SSZ-13 by forming Pd(II)(NO)(CO), a mixed carbonyl–nitrosyl complex, whereas water hampered the NOx adsorption ability. Consequently, CO and NOx could be

simultaneously abated over Pd/SSZ-13 during cold-start [37].

The effect of CO on the adsorption of NOx on Pd/CeO_2 or Pd/CeO_2-ZrO_2 has also been investigated. Theis and Lambert [38] observed that C_2H_4 and CO increased the NOx adsorption ability of Pd/CeO_2-ZrO_2. Furthermore, they first reported that the formation of –NCO groups during the reaction of NO and CO, which were identified using diffuse reflectance infrared Fourier-transform spectroscopy (DRIFTS), accounted for the improved NOx adsorption at low temperatures. Moreover, Theis and Lambert [39] reported that NO and CO interacted on PdO_x to produce chemical intermediates, thereby reducing PdO_x during NOx adsorption. Lean CH_4 oxidation was used to determine the average oxidation state of PdO_x in catalysts using sequential performance tests. When the oxidation state of PdO_x was low, the NOx adsorption ability was high. Recently, Kvasničková et al. [40] attributed the increase in NOx adsorption ability of PtPd/CeO_2-ZrO_2 in the presence of CO to the reduction of PdO nanoparticles because the reduced metal increased the NOx adsorption ability of the catalyst. However, the adsorption mechanism of NOx over Pd/CeO_2 in the presence of CO has not been well established.

In this study, it is investigated that the NOx adsorption ability of Pd/CeO_2 in the presence and absence of CO. The NOx adsorption ability of Pd/CeO_2 was significantly increased in the presence of CO. The effect of CO has been extensively studied by investigating the roles of Pd and CeO_2,

CO oxidation activity, and pretreatment conditions. Combining the results of the performance tests and DRIFTS analysis, a model was suggested that can explain the increase in NOx adsorption ability of Pd/CeO_2 in the presence of CO.

2.2. Experimental

2.2.1. Catalyst preparation

CeO_2 and γ-Al_2O_3 were obtained from Solvay and Sasol, respectively. Pd (2 wt%) was loaded onto CeO_2 and Al_2O_3 using the incipient wetness impregnation method. An aqueous solution of $Pd(NO_3)_2 \cdot 2H_2O$ (Merck) was used as the Pd precursor. The supported catalysts were dried overnight in an oven at 100 °C. Subsequently, the dried catalysts and bare CeO_2 were calcined at 500 °C for 2 h in a flow reactor under a 100 mL/min flow of 15 % O_2 balanced with N_2. Thus prepared catalysts were denoted as CeO_2, Pd/CeO_2, and Pd/Al_2O_3.

2.2.2. Catalyst characterization

X-ray diffraction (XRD) patterns were obtained using a Mode 1 Smartlab diffractometer (Rigaku, Japan) with Cu Kα radiation (40 kV and 30 mA) in the 2θ range of 10° to 80° at a step size of 0.02° and a rate of 2.5°/min. N_2 physisorption was conducted to measure the Brunauer–

Emmett–Teller (BET) surface areas and pore volumes using a BELSORP-mini II (MicrotracBEL, Japan) instrument. The samples were pretreated at 150 °C for 4 h under a vacuum. Cryogenic H_2 temperature-programmed reduction (H_2-TPR) experiments were conducted using a BELCAT II (MicrotracBEL, Japan) apparatus coupled with a thermal conductivity detector. Before measurements, 0.05 g of each catalyst was fully oxidized under 50 mL/min air at 500 °C. After cooling to -90 °C, the temperature was ramped to 900 °C at a rate of 10 °C/min under a 5 % H_2/Ar gas flow of 30 mL/min. Pulsed CO chemisorption was conducted using a BELCAT II (MicrotracBEL, Japan) apparatus to evaluate the dispersion and average particle size of Pd. Catalyst samples (0.05 g) were reduced using a 5 % H_2/Ar flow at 400 °C for 30 min, followed by He purging for 30 min and cooling to -78 °C. Subsequently, a 5 % CO/He pulse was introduced in the reactor. The stoichiometric factor was assumed to be 1. *In situ* DRIFTS profiles were obtained using a Nicolet 6700 (Thermo Fisher Scientific) Fourier-transform infrared (FTIR) spectrometer equipped with a mercury cadmium telluride (MCT) detector and a Praying Mantis (Harrick Scientific Products) diffuse reflectance cell. The sample loaded on the cell was first pretreated with a 10 % O_2/N_2 flow (50 mL/min) at 400 °C for 30 min to remove impurities. After cooling to 120 °C, 5 % H_2O was added using a syringe pump. The total flow did not change during the entire process. The sample background was obtained at 120 °C after stabilization before NOx adsorption. Thereafter, 500 ppm of NO was added to the feed, and a

spectrum was collected every 1 min. After 60 min, 5000 ppm of CO was added to the feed, and spectra were collected over 60 min.

2.2.3 Evaluation of NOx adsorption ability

Powdered catalyst samples were sieved to 150-180 μm. Catalyst samples (0.1 g) and α-Al_2O_3 beads (0.1 g) were added to a continuous-flow quartz reactor. NOx adsorption tests in the presence and absence of CO were performed according to the procedure illustrated in Figure 2-1. The total flow rate was maintained at 200 mL/min (gas hourly space velocity of 120 000 mL/(h·g_{cat})). A mixture of 10 % O_2, 5 % CO_2, and 5 % H_2O balanced with N_2 gas was continuously flown through the reactor during the experiment. During the pretreatment step, the catalyst was heated to 500 °C (ramping rate of 10 °C/min) under a gas mixture of 10 % O_2, 5 % CO_2, and 5 % H_2O for 30 min followed by cooling to 120 °C. NO (100 ppm) and CO (1000 ppm only for the tests in the presence of CO) were introduced in the reactor for 60 min, and the bypassed gas was analyzed using a Nicolet iS50 (Thermo Fisher Scientific) FTIR spectrometer equipped with an MCT detector. When 100 ppm NO was used, several ppm of NO_2 was naturally generated. The sum of the measured NO and NO_2 concentrations was reported as the NOx concentration. After NOx was adsorbed, temperature-programmed desorption experiments were performed. The reactor temperature was increased from 120 to 500 °C at a rate of 10 °C/min and

maintained for 30 min. The possibility of a reaction between NO and CO at 120 °C was excluded unless mentioned because the amounts of NOx adsorbed during the adsorption step and NOx desorbed during desorption were similar within the error range.

For the NOx adsorption performance test after H_2 pretreatment, the catalyst was exposed to 1 % H_2, 5 % H_2O, 5 % CO_2, and balance N_2 for 1 h at 120 °C and was purged for 30 min after pretreatment and before adsorption. The remaining adsorption and desorption steps were performed in accordance to the procedure illustrated in Figure 2-1.

2.2.4. Steady-state CO oxidation with NO pulse

For CO oxidation, the catalyst was added to the reactor using the same procedure utilized for the NOx adsorption test. After pretreatment, a gas feed comprising 1000 ppm CO, 10 % O_2, 5 % CO_2, and 5 % H_2O balanced with N_2 was introduced in the reactor at 120 °C. The concentration of bypassed CO was measured using a FTIR spectrometer. After the CO concentration reached a steady level, 100 ppm NO was injected for 100 s. NO pulse injection was repeated 12 times after the CO concentration reached a steady level for each pulse injection.

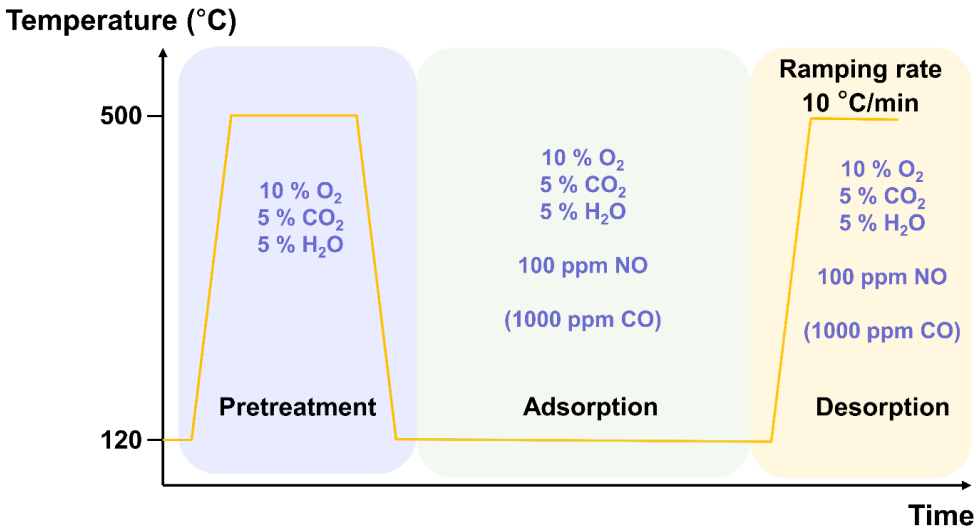

Figure 2-1. Experimental protocol for the NOx adsorption performance test.

2.3. Results and Discussion

The XRD patterns of Pd/CeO_2 and Pd/Al_2O_3 matched the characteristic crystallite peaks of the CeO_2 and γ-Al_2O_3 phases (Figure 2-2) [41, 42]. The characteristic peaks of PdO and metallic Pd were not observed in the XRD pattern of Pd/CeO_2, indicating that Pd was well-dispersed on the CeO_2 support. However, the PdO crystallite peak at 33.9° was observed in the XRD profile of Pd/Al_2O_3, indicating the presence of large PdO particles. These results were consistent with the average Pd particle size determined using CO chemisorption, as summarized in Table 2-1. The average sizes of Pd particles in Pd/Al_2O_3 and Pd/CeO_2 were 13.7 and 4.3 nm, respectively; this was mainly attributed to the strong interaction between Pd and CeO_2 [43].

Figure 2-3A illustrates the NOx profiles of Pd/CeO_2 during the NOx adsorption performance test conducted for 180 min. The NOx concentration was maintained slightly below the injected NOx concentration of 100 ppm and was gradually increased over time; this indicated that a small amount of NOx was continuously adsorbed during the test. A relatively large proportion of NOx was adsorbed during the initial 10 min. The increase in the amount of NOx adsorbed over time was confirmed using the NOx desorption curves as a function of time (Figure 2-3B). NOx desorption is indicated by the peaks at approximately 300 and 500 °C. As adsorption time increased, the high-temperature peak was unaffected, and the low-

temperature peak, which was attributed to the desorption of weakly adsorbed NOx, increased and shifted to lower temperatures. During the desorption step that occurred after adsorption for 30 min, additional NOx adsorption occurred at 180 °C. This extra adsorption was attributed to the desorption of water, which increased the number of active sites available for NO adsorption during temperature ramping. It has been reported that water interferes with NOx adsorption at low temperatures [13, 38]. As the water was desorbed with increasing temperature, NOx could be adsorbed at the sites initially occupied by water. The additional adsorption was not observed during the NOx adsorption test without water. This was also confirmed through DRIFTS analysis in which NOx adsorption increased as water desorbed while raising the temperature after adsorbing NO for 1 h (data not shown). However, this additional adsorption disappeared from the desorption curves after 80 and 180 min of adsorption. These results indicated that NOx adsorbed competitively with water on the surface of Pd/CeO_2, and the amount of NOx adsorbed could be increased by overcoming the interference of water over a sufficient time. However, the negligible effect of water on the adsorption of NOx over a long adsorption time is not desirable because a large amount of NOx should be adsorbed quickly to decrease NOx emission during cold-start. Under the reaction conditions in this study, after the initial 10 min, Pd/CeO_2 slowly adsorbed NOx over a long time, which is unsuitable for cold-start applications.

To increase the NOx adsorption ability of Pd/CeO_2 at low temperatures, the modification of the catalyst surface, increasing resistance to water, or addition of reducing agents have been suggested [39, 44, 45]. As presented in Figure 2-4, the initial NOx adsorption ability of Pd/CeO_2 can be significantly increased by adding reducing agents, such as CO, H_2, or C_3H_6. In particular, the amount of weakly adsorbed NOx species (desorbed at approximately 300 °C) was mainly increased by adding reducing agents to the catalyst. This was desirable because engine exhaust gas contains a certain amount of reducing agents, and NOx must be desorbed in an appropriate temperature range to be regenerated and reused. In the presence of CO, the NOx desorption peak shifted from 300 to 200 °C. Among the three reducing agents, CO presented the best efficiency in terms of desorption temperature and adsorption amount. During the initial 10 min, the amount of NOx adsorbed in the presence of CO increased more than six times (Table 2-2).

DRIFTS experiments were performed to elucidate the increase in the NOx adsorption ability of Pd/CeO_2 in the presence of CO. *In situ* DRIFTS profiles were obtained during the adsorption of NO in the absence (500 ppm NO, 10 % O_2, and 5 % H_2O; Figure 2-5A) and presence of CO (500 ppm NO, 5000 ppm CO, 10 % O_2, and 5 % H_2O; Figure 2-5B) to confirm the increase in the amount of NOx adsorbed in the presence of CO. The NOx adsorption peak appeared in the wavenumber range of 1700-1000

cm^{-1} and included NO_3^- (1331 and 1406 cm^{-1}), monodentate nitrates (1458 cm^{-1}), and bidentate nitrates (1530 and 1568 cm^{-1}) [13, 46, 47]. The most prominent peaks were those ascribed to bidentate nitrite at 1230 cm^{-1} and bridging nitro-nitrito at 1472 cm^{-1} [13, 46, 47]. During NO adsorption, the intensities of almost all the bands in the wavenumber range of 1800-800 cm^{-1} increased. When CO was added, the intensities increased more rapidly. These results were consistent with the rapid decrease in bypass NOx concentration during the NOx adsorption performance test in the presence of CO. Figure 2-5C illustrates the changes in the relative intensity of the peak at 1230 cm^{-1} with adsorption time. The peak intensity was normalized based on the spectrum collected at 60 min (Figure 2-5A). During the first 60 min, peak intensity increased linearly with increasing adsorption time. The relative intensity of the peak at 1230 cm^{-1} increased more than twice within 10 min when CO was added. This indicated that the increase in NOx adsorption ability upon adding CO was mainly attributed to the high NOx adsorption rate. Theis and Lambert [38] reported the presence of an –NCO peak at 2150 cm^{-1} caused by the reaction of NO and CO. However, this peak was not observed in our study, which could be attributed to the presence of water during the DRIFTS experiments.

NOx adsorption performance tests were conducted on bare CeO_2 and Pd/Al_2O_3 to differentiate the roles of CeO_2 and Pd. It was predicted that the roles of CeO_2 and Pd in Pd/CeO_2 would be elucidated by performing

similar NOx adsorption experiments over CeO_2 and Pd/Al_2O_3. The promoting effect of CO on the NOx adsorption ability was not as prominent for CeO_2 and Pd/Al_2O_3 as it was for Pd/CeO_2 (Figure 2-6). In other words, the CO-promoted NOx adsorption was activated only when Pd and CeO_2 coexisted. Therefore, it was deduced that both Pd and CeO_2 were involved in a series of NOx adsorption steps in the presence of CO. In Pd/Al_2O_3, slightly more NOx was adsorbed in the presence of CO for the first 10 min, although a smaller amount of NOx was desorbed during the desorption step. During the desorption process on Pd/Al_2O_3, additional adsorption only occurred at approximately 200 °C in the presence of CO. Theoretically, CO can interfere with NOx adsorption via competitive adsorption on the Pd surface [48, 49]. Therefore, if CO was oxidized to CO_2, which was desorbed with increasing temperature, NO could be adsorbed and stored on the Pd surface. The competitive adsorption of NO and CO on the Pd surface was confirmed through further experiments. Figure 2-7 illustrates the changes in NO and CO concentrations upon CO addition halfway through the NOx adsorption experiments performed at 120 °C over Pd/CeO_2 and Pd/Al_2O_3. After 60 min, 1000 ppm CO was added to the feed gas, and the concentrations of NOx and CO were measured for 60 min. Additional NOx adsorption occurred on Pd/CeO_2 (Figure 2-7A), whereas the adsorbed NOx was desorbed from Pd/Al_2O_3 (Figure 2-7B). This suggested that CO and NOx were competitively adsorbed on the Pd surface, and some adsorbed NOx was desorbed when CO was added. When bare CeO_2 was used as the

catalyst, the NOx concentration did not change when CO was added (data not shown). Therefore, it was inferred that the promoting effect of CO on the NOx adsorption on Pd/CeO_2 could be ascribed to the interaction between Pd and CeO_2 at the interface. To gain a deeper understanding of the phenomena that occurred at the Pd–CeO_2 interface, the change in CO concentration was investigated.

CO conversion was measured during the NOx adsorption performance test at 120 °C, and the results are summarized in Table 2-3. The CO oxidation ability of Pd/CeO_2 was higher than those of CeO_2 and Pd/Al_2O_3. The CO conversion of Pd/CeO_2 was higher than 80 % in the absence of NO and was only 18 % in the presence of NO. The steady-state CO oxidation activity of Pd/CeO_2 varied depending on the presence or absence of NO. Another experiment was conducted to examine the effect of NO on CO oxidation. Figure 2-8 displays the steady-state CO conversion and accumulative NOx adsorption on Pd/CeO_2 during CO oxidation with NO pulse experiments. The steady-state CO conversion was measured as 100 ppm NO was injected as a pulse for 100 s periodically. Pd/CeO_2 is well known for its excellent low-temperature CO oxidation activity [50, 51]. As the number of NO pulse injections increased, the CO conversion decreased and the amount of accumulated NO adsorbed increased. Initially, the CO conversion exceeded 80 %, but after exposure to 12 NO pulses, it declined to below 40 %. At first glance, the competition between CO oxidation and NOx adsorption appeared contradictory because the addition of CO

promoted NOx adsorption. The increase in the amount of NOx adsorbed slowed as the CO oxidation activity decreased. It can be inferred that NOx adsorption increased at the expense of CO oxidation. One of the processes in which CO is oxidized facilitates NOx adsorption on the surface of the catalyst. After that, CO oxidation can no longer occur at that site.

H_2-TPR and NO adsorption performance tests were conducted after reductive pretreatment to elucidate the promoting effect in detail. Figure 2-9 illustrates the H_2-TPR results for Pd/CeO_2, CeO_2, and Pd/Al_2O_3. The peak at approximately 500 °C in the H_2-TPR profile of CeO_2 corresponded to the reduction of surface CeO_2, and the high-temperature peak above 800 °C originated from the reduction of bulk CeO_2 [52]. When CeO_2 was impregnated with Pd, the surface reduction peak at 500 °C disappeared, and a new peak ascribed to the reduction of PdO appeared at approximately 25 °C. Quantitative analysis indicated that the amount of H_2 consumed below 100 °C (0.30 mmol/g_{cat}) was greater than the total PdO amount loaded on CeO_2 (0.19 mmol/g_{cat}). This was explained by the hydrogen spillover from Pd to CeO_2 [53, 54]. The hydrogen adsorbed on the Pd surface facilitates the reduction of surface CeO_2 even at low temperatures. The H_2-TPR results indicated that the temperature of 120 °C was sufficient to reduce the Pd/CeO_2 and Pd/Al_2O_3 surface. Therefore, the H_2 treatment was performed at 120 °C, the same temperature as the adsorption performance test, and the adsorption performance test was conducted.

Figure 2-10A and 2-10B illustrate the NOx adsorption performance data after Pd/CeO_2 was pretreated with H_2 at 120 °C. The surface of Pd/CeO_2 was expected to be reduced after H_2 pretreatment. After reductive treatment, the NOx adsorption ability increased significantly in the absence of CO, just as it did when CO was present in the reactant feed (Figure 2-4). It has been reported that NOx adsorption increased on the surface of reduced CeO_2 [55, 56]. Filtschew and Hess reported that the ability of CeO_2 to change the oxidation state of cerium and create oxygen vacancies (V_Os) was crucial for NOx adsorption [56]. Likewise, V_Os on the reduced CeO_2 surface can participate in the series of NOx adsorption reaction steps or function as direct NOx adsorption sites [56].

Figure 2-10C and 2-10D display the NOx adsorption performance data after Pd/Al_2O_3 was pretreated with H_2 at 120 °C. The amount of NOx adsorbed for 10 min significantly increased by more than 4 times (Table 2). Although not as drastic as in Pd/CeO_2, it is a notable increase considering the dispersion of Pd in Pd/Al_2O_3. This is in good agreement with previous literature. Theis and Lambert reported that as the oxidation state of PdOx was decreased, the NOx adsorption ability was increased in Pd/CZO [39]. However, when the Pd/Al_2O_3 was not reductively treated, the promoting effect of CO was hardly seen, unlike Pd/CeO_2 (Figure 2-4A and Figure 2-6C). In addition, the total amount of NOx desorbed (16.6 μmol/g) is less than the amount of NOx adsorbed (31.4 μmol/g), which can be seen when

Pd was reduced, the reduction reaction of NOx occurred together. This phenomenon was not observed when NO and CO flowed together in NOx adsorption test over Pd/CeO_2 (Figure 2-4). Therefore, it is reasonable to interpret that reduction of PdO by CO is not the main factor of the promoting effect of CO under the current reaction conditions over Pd/CeO_2. Not only the effect of Pd oxidation state change but also the interaction between Pd and CeO_2 are very important in explaining the promoting effect of CO on NOx adsorption over Pd/CeO_2. One important role of Pd is to facilitate the reduction of the CeO_2 surface, as can be seen from the H_2-TPR results (Figure 2-9).

During the NOx adsorption performance test in the presence of CO over Pd/CeO_2, it was considered that CO oxidation created V_Os. During H_2 pretreatment, V_Os were generated as the entire surface was reduced. The NOx adsorption performance test was conducted under oxidative conditions; however, even under these conditions, V_Os could be generated near the Pd–CeO_2 interface. Although the exact CO oxidation mechanism over Pd/CeO_2 has not been elucidated yet, low-temperature CO oxidation is generally considered to follow the Mars–van Krevelen (M–vK) mechanism [57, 58]. In detail, Wu et al. [58] revealed the reaction pathways and reaction intermediates of CO oxidation over CeO_2 nanoshapes using *in situ* IR and Raman spectroscopy experiments. They observed that carbonate species were formed through the adsorption of CO on the CeO_2 nanoshapes

at room temperature and revealed that CO_2 was generated via the direct reaction of CO with lattice oxygen. CO adsorbed on Pd readily reacted with the surface lattice oxygen of CeO_2 to form an active carbonate-like intermediate. As CO_2 left the catalyst surface, V_Os were generated on the Pd/CeO_2 surface.

A schematic illustration of the NOx adsorption mechanism promoted by CO oxidation over Pd/CeO_2 is presented in Figure 2-11. The NOx adsorption ability could be promoted by recovering the V_Os upon NOx adsorption. The Pd–CeO_2 interface, where the V_Os are generated, acted as a promoted adsorption site. Pd, CeO_2, and the interaction between Pd and CeO_2 played crucial roles in the CO-promoted NOx adsorption: (i) CO readily adsorbed on Pd, (ii) CeO_2 exhibited oxygen adsorption capacity to provide lattice oxygen, (iii) CO oxidation was promoted by the interaction between Pd and CeO_2, and (iv) V_Os generated via CO oxidation served as NOx adsorption sites. CO promoted NOx adsorption through this series of processes, and the CO oxidation activity decreased because CO oxidation no longer occurred at the sites where NOx was adsorbed.

Table 2-1. Physical properties of CeO_2, Pd/CeO_2, Al_2O_3, and Pd/Al_2O_3.

Sample	BET surface area (m^2/g)	Pore volume (cm^3/g)	Pd dispersion[a] (%)	Average Pd particle size[a] (nm)
CeO_2	113	0.28	-	-
Pd/CeO_2	130	0.29	26.1	4.3
Pd/Al_2O_3	164	0.30	8.1	13.7

[a] measured using CO chemisorption

Table 2-2. Amount of NOx adsorbed as a function of time under different conditions.

	t (min)	NOx adsorbed (μmol/g)		
		Pd/CeO_2	**CeO_2**	**Pd/Al_2O_3**
NO only	10	7.7	2.5	3.2
	60	31.5	19.8	16.9
	180	85.5	-	-
NO + CO	10	48.9	2.6	5.6
	60	141.0	19.4	10.5
NO + H_2	10	16.3	-	-
	60	30.9	-	-
NO + C_3H_6	10	22.5	-	-
	60	57.6	-	-
After 120°C reduction	10	44.3	-	15.6
	60	104.9	-	31.4

Table 2-3. Steady-state CO conversion in the presence and absence NO at 120 ℃.

	CO conversion (%)		
	Pd/CeO_2	**CeO_2**	**Pd/Al_2O_3**
In the presence of NO	18	0	9
In the absence of NO	81	0	12

(1000 ppm CO, 10 % O_2, 5 % H_2O, 5 % CO_2, and 100 ppm NO, if added)

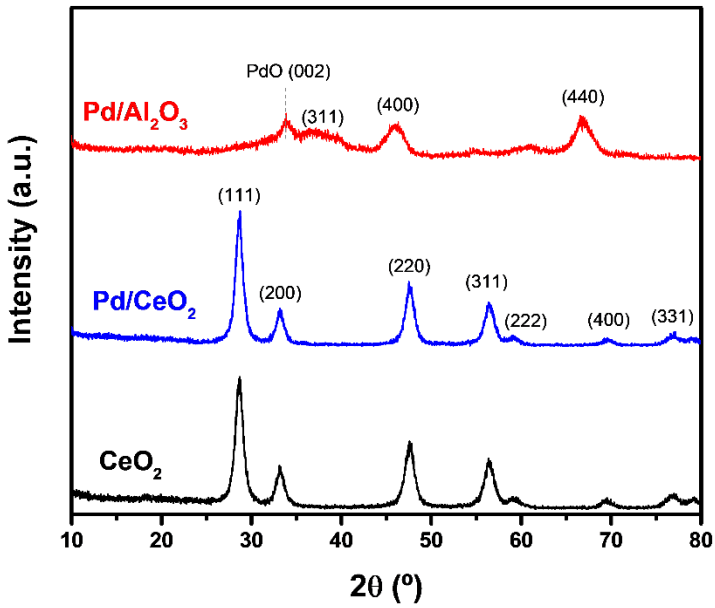

Figure 2-2. X-ray diffraction patterns of CeO_2, Pd/CeO_2, and Pd/Al_2O_3.

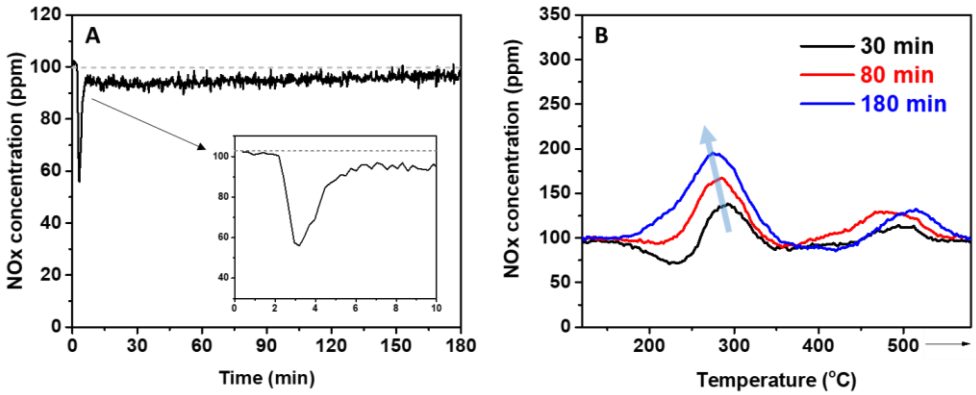

Figure 2-3. (A) NOx profiles of Pd/CeO_2 during the 180 min NOx adsorption performance test at 120 °C and (B) desorption curves over Pd/CeO_2 as a function of the NOx adsorption time (30, 80, and 180 min).

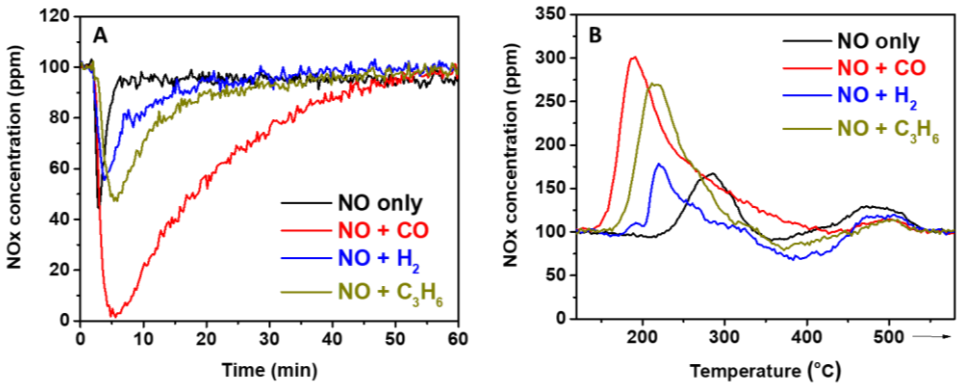

Figure 2-4. (A) NOx profiles of NOx adsorption performance test at 120 °C in the presence and absence of reducing agents (CO, H_2, C_3H_6) and (B) corresponding desorption curves over Pd/CeO_2.

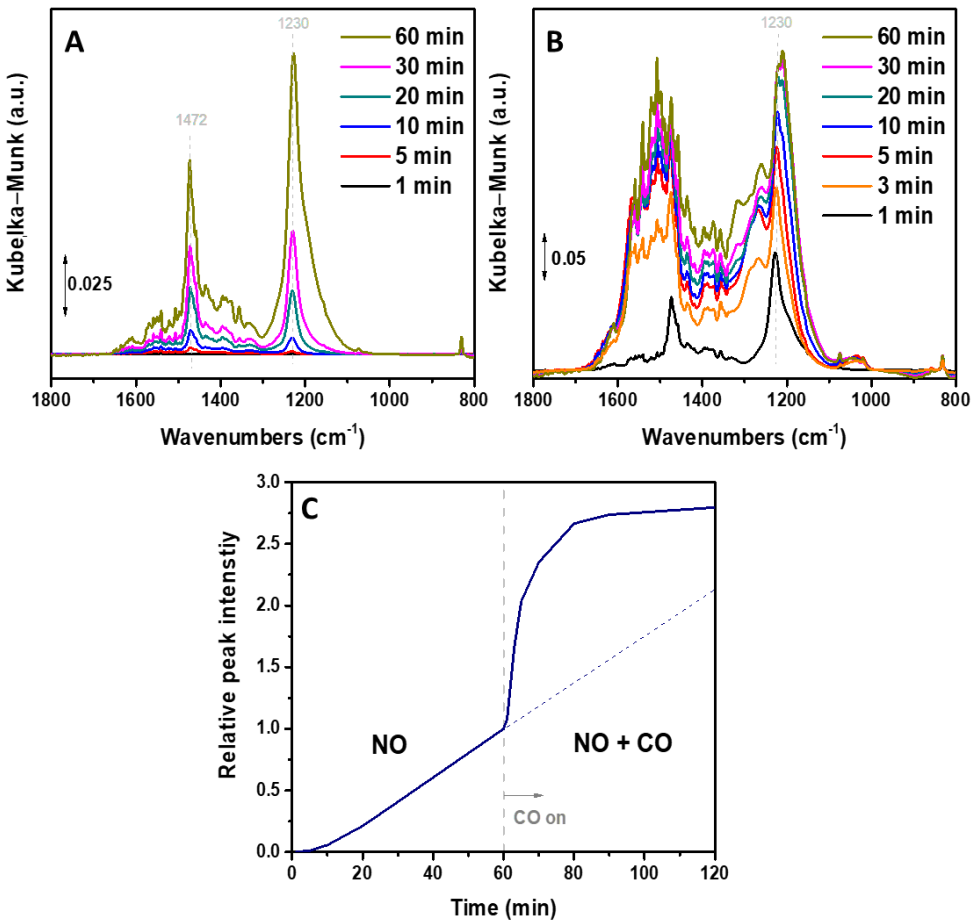

Figure 2-5. *In situ* diffuse reflectance infrared Fourier-transform spectroscopy profiles of (A) NO adsorption followed by (B) NO adsorption in the presence of CO on Pd/CeO_2 as a function of time in the wavenumber range of 1800-800 cm^{-1}. (C) Relative intensity of the peak at 1230 cm-1 over time during the adsorption of NO in the absence and presence of CO.

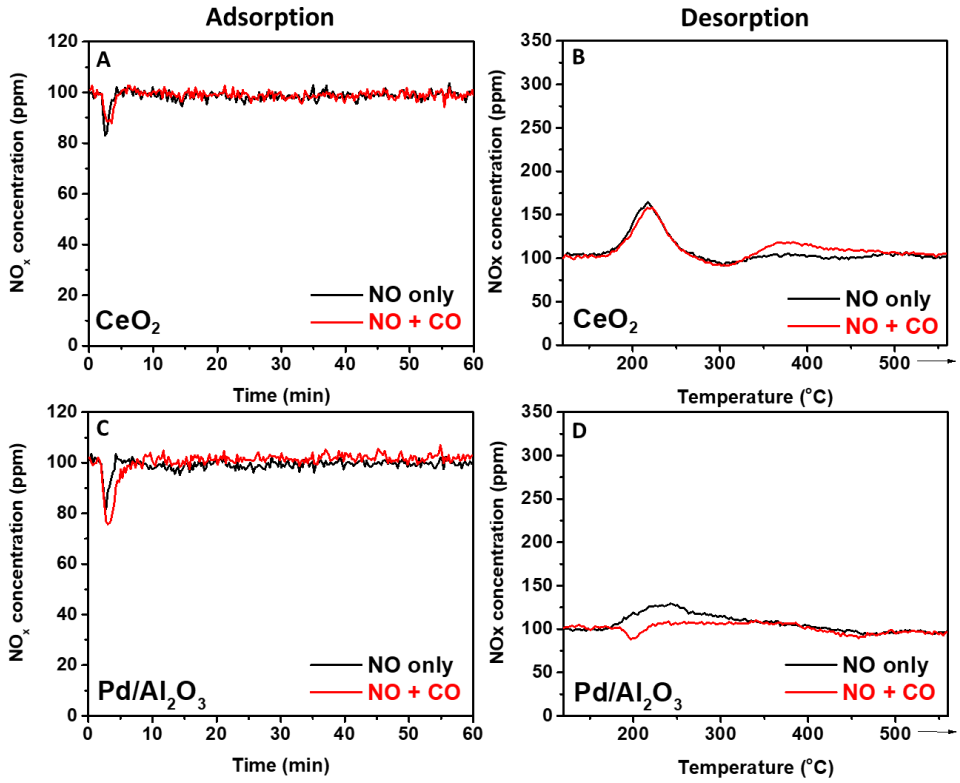

Figure 2-6. NOx profiles during NOx adsorption performance test at 120 °C and corresponding desorption curves over (A) and (B) CeO_2 and (C) and (D) Pd/Al_2O_3.

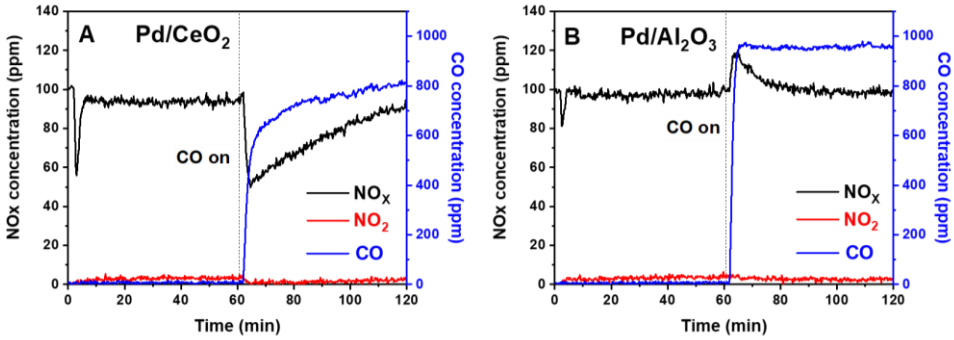

Figure 2-7. NOx and CO profiles of (A) Pd/CeO_2 and (B) Pd/Al_2O_3 upon CO addition to the feed stream after 60 min of NO adsorption.

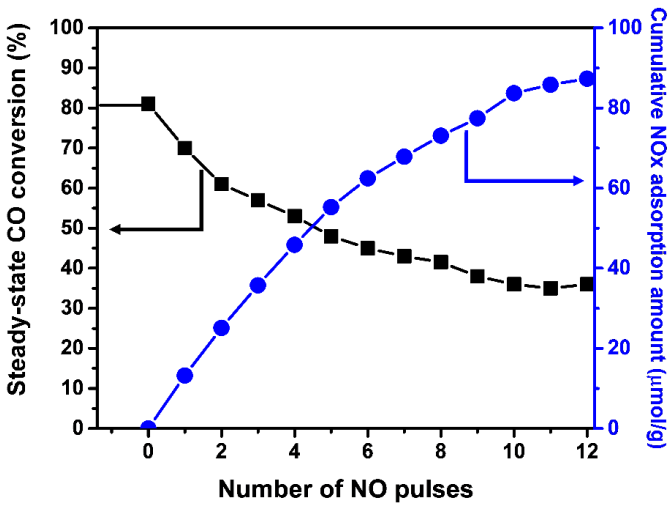

Figure 2-8. CO conversion and cumulative NOx adsorption during the steady-state CO oxidation test over Pd/CeO_2 at 120 °C; a 100 ppm NO pulse was repeatedly injected in the system.

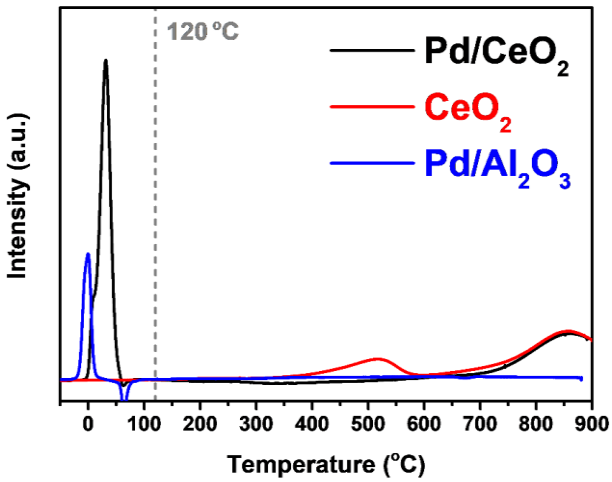

Figure 2-9. H_2 temperature-programmed reduction profiles of CeO_2, Pd/CeO_2, and Pd/Al_2O_3.

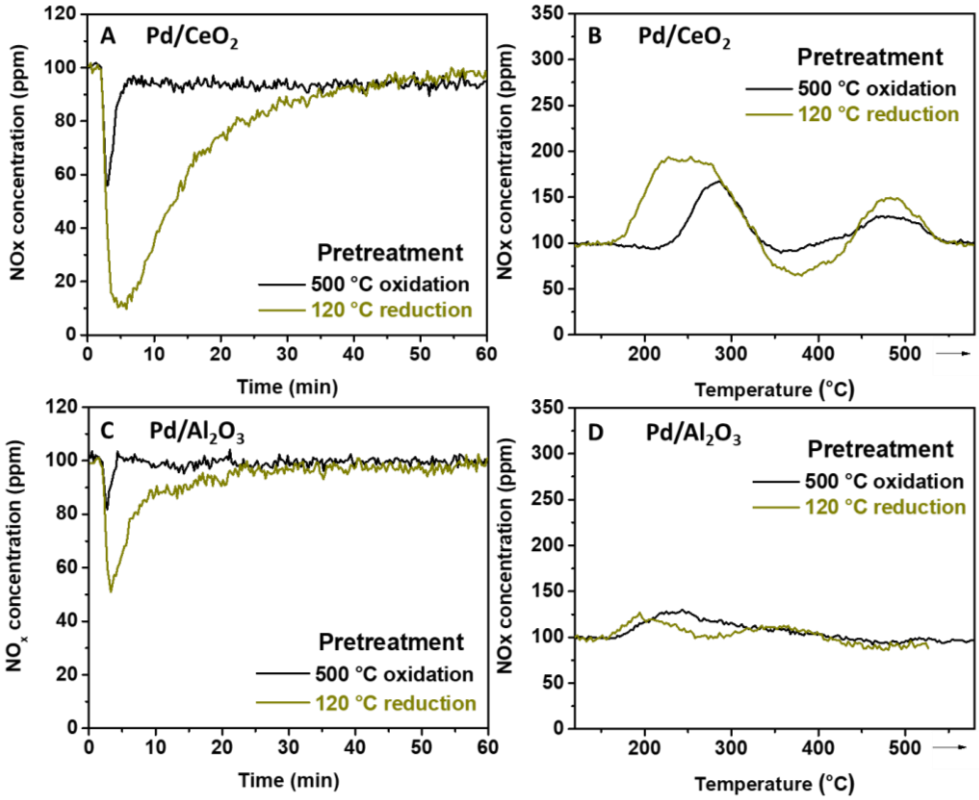

Figure 2-10. NOx profiles during NOx adsorption performance test after oxidative and reductive treatment and corresponding desorption curves over (A), (B) Pd/CeO_2 and (C), (D) Pd/Al_2O_3.

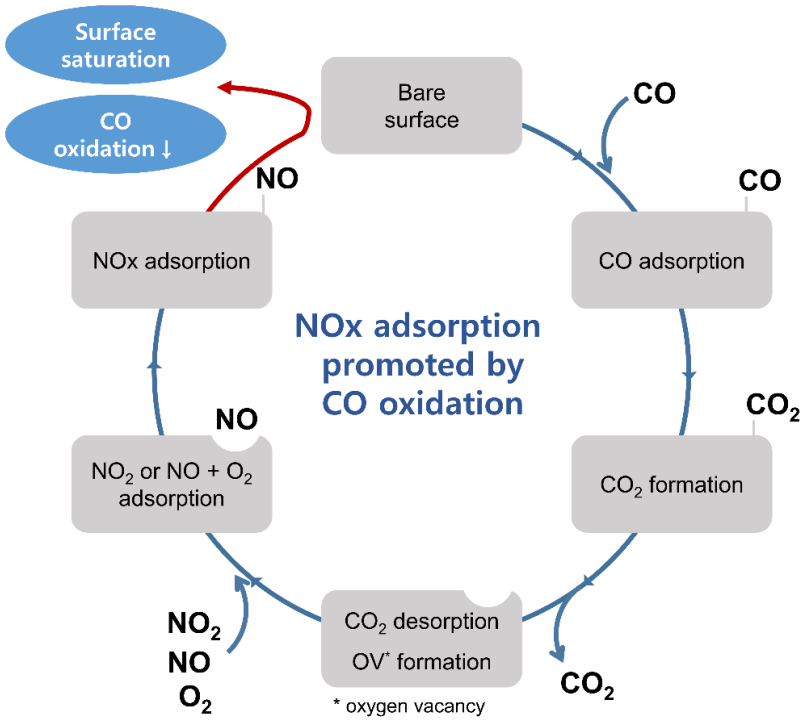

Figure 2-11. Schematic illustration of NOx adsorption promoted by CO oxidation on Pd/CeO_2.

Chapter 3. Optimizing NO reduction and storage for gasoline vehicle application

3.1. Introduction

Stringent toxic gas and CO_2 emission regulations are encouraging automakers to switch their propulsion systems from internal combustion engines to batteries or fuel cells [7, 60, 61]. The transition to battery and fuel cell electric vehicles (BEVs and FCEVs, respectively) could help achieve carbon neutrality, owing to the use of renewable energy sources. However, the pace of this transition in each country or region is highly dependent on their infrastructure, e.g., power mix and access to green energy. Therefore, complete worldwide transition to BEVs or FCEVs will likely take decades [7, 62, 63]. During this transition, highly efficient internal combustion engine vehicles, including hybrid vehicles or gasoline vehicles with downsized engines, will almost certainly remain relevant.

Although state-of-the-art TWCs can convert NO into N_2 at temperatures above 150 °C, stringent emissions regulations do not allow NO emissions even at temperatures below 150 °C, the cold-start period [7, 64]. Removing NO emitted during the cold-start of diesel vehicles has been

---

[#] This chapter cites the author's published journal article: J. Lee[1], Y. Kim[1], S. Hwang[1], G. S. Hong[1], E. Lee, H. Lee, C. Jeong, C. H. Kim, J. S. Yoo, and D. H. Kim, "Toward gasoline vehicles with zero harmful emissions by storing NO at Pd nanoparticle–CeO_2 interface during the cold-start period", Chem Catalysis, 2 (2022) 2289-2301 [59].

extensively investigated recently, but few studies have been conducted to remove NO emitted during the cold-start period of gasoline vehicles [65, 66]. This inspired our strategy to temporarily store NO at low temperatures (e.g., during the cold-start period) and then convert it to N_2 at high temperatures. In this study, CeO_2 as a NO storage material was studied, not only because CeO_2 is always present as an oxygen storage material in the TWC, but also because oxygen vacancies (V_Os) on the CeO_2 surface are reported to interact strongly with NO/NO_2 molecules [57, 67-71]. However, the reducibility of CeO_2 must be improved to utilize V_Os, because the pristine CeO_2 surface can only be reduced at high temperatures above the cold-start temperature (>200 °C) [72-75].

The catalytic properties of metal oxide can be significantly modified by the deposited metals [76-82]. Particularly, the unique interaction between CeO_2 and platinum group metals (PGMs) greatly enhances the reducibility of CeO_2 surface, allowing it to be reduced even below room temperature (Figure 3-1). In addition, Pd particles have high activity in NO oxidation reaction due to their high affinity for NO and O [83-85]. This would promote the formation of NO_2 at low temperature, which can interact with the V_Os of CeO_2 even more strongly than NO; this is another potential advantage of using PGM-loaded CeO_2. With this hypothesis, CeO_2-supported PGMs were devised to achieve nearly zero NO emissions from gasoline vehicles in this study. It is optimized that the

support and metal species, metal content, and air-fuel equivalence ratio (λ) to maximize the NO abatement ability and understand the NO storage and reduction mechanisms. Detailed characterizations and density functional theory (DFT) calculations demonstrate that the NO reduction to N_2 is promoted at low λ on the metallic Pd surface, whereas the NO storage is promoted in the form of NO_2 at high λ at the Pd nanoparticle (NP)–CeO_{2-x} interface. Therefore, the application of the combined adsorption and catalytic functions of CeO_2-supported PGMs could bring the NO emissions much closer to zero in gasoline vehicle exhaust gas.

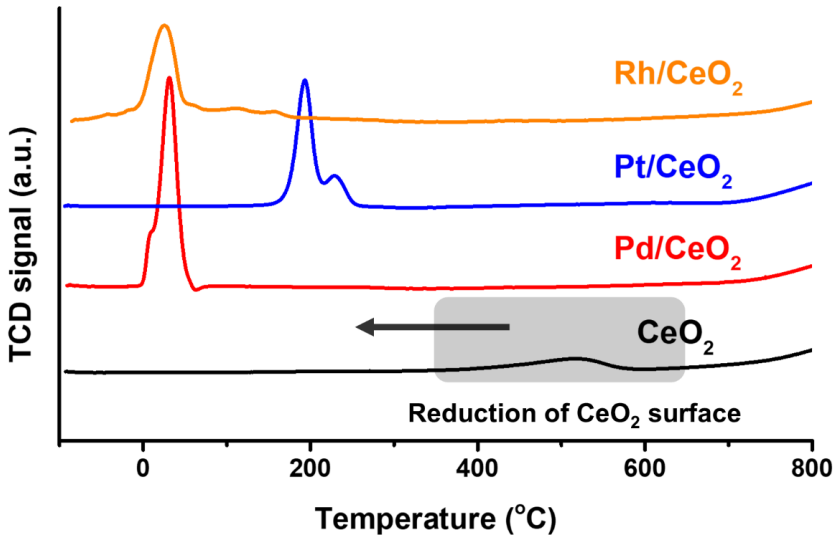

Figure 3-1. H_2-TPR profiles of CeO_2, and PGM-impregnated CeO_2.

The reduction of CeO_2 surface is facilitated by PGM, resulting in the much lower reduction temperature even below 100 °C.

3.2. Experimental

3.2.1. Catalyst preparation

The catalysts were prepared using the conventional incipient wetness impregnation method. Commercial CeO_2 (Solvay), and Al_2O_3 (Sasol) were used as support materials. Al_2O_3 was calcined at 550 °C for 3 h under air to obtain the γ-Al_2O_3 phase. All support powders were dried in an oven at 105 °C for 3 h before impregnating metal precursors. The desired amounts of Pd, Pt, and Rh were loaded onto the supports by impregnating aqueous solutions of $Pd(NO_3)_2 \cdot 2H_2O$ (Merck), $Pt(NH_3)_4(NO_3)_2$ (Alfa Aesar), or $Rh(NO_3)_3$ (10 wt.% Rh in solution, Merck) as the metal precursor, respectively. The amount of precursor solution was determined from the pore volume measured from the N_2 adsorption–desorption isotherms. To uniformly distribute the metal and increase the reproducibility, the entire solution was divided and loaded three times. The resulting powder was dried at 105 °C overnight and then calcined at 800 °C under a 100 mL/min gas flow of 15 vol.% O_2 with an N_2 balance for 2 h. The prepared catalysts were CeO_2, Pd(0.5)/CeO_2, Pd(1)/CeO_2, Pd(2)/CeO_2, Pd(3)/CeO_2, Pd(4)/CeO_2, Pt(2)/CeO_2, Pt(1)–Pd(1)/CeO_2, Rh(2)/CeO_2, and Pd(2)/γ-Al_2O_3. The metal loadings are shown in the parentheses. If metal loading was not specified, it is 2 wt.%. Commercial Pd(5)/γ-Al_2O_3 powder (Merck) was also used for comparison with the Pd(2)/CeO_2 catalyst with a similar Pd particle size.

3.2.2. Performance evaluation

The catalytic activities and NO storage abilities of the catalysts were evaluated using a continuous-flow quartz tubular reactor. First, 0.1 g of catalyst (80–100 mesh) was loaded in the reactor with 0.1 g of α-Al_2O_3 (80–100 mesh) to dissipate the heat produced during the experiments. The total flow rate was maintained at 200 mL/min (gas hourly space velocity, GHSV = 120,000 mL/h·g_{cat}) under atmospheric pressure, with various gas compositions (NO, H_2O, CO_2, O_2, CO, H_2, and C_3H_6) to simulate gasoline exhaust. The λ values, defined as $\lambda = ([O_2] + 0.5[CO] + 0.5[H_2O] + [CO_2] + 0.5[NO])/([CO] + 0.5[H_2] + 4.5[C_3H_6] + 0.5[H_2O] + [CO_2])$, was also controlled. Typically, 100 ppm NO, 5 vol.% H_2O, 5 vol.% CO_2, 6,000 ppm CO, 2,000 ppm H_2, 1,000 ppm C_3H_6, and N_2 (as the balance) were introduced, while the O_2 concentration was varied from 0.5 to 1.35 vol.%; this changed the λ from 0.95 to 1.05. The concentrations of the outlet gas components are analyzed using an online FT-IR spectrometer (Nicolet iS50, Thermo Fisher Scientific) with a mercury cadmium telluride (MCT) detector. The feed gas compositions and conditions are summarized in Table 3-1 and explained as follows:

(i) Steady-state activity test: The samples were pre-treated at 700 °C at a ramping rate of 10 °C/min for 30 min with 5 vol.% O_2, 5 vol.% H_2O, and 5 vol.% CO_2 (balanced with N_2), and then cooled down to 120 °C (Scheme 3-1A). After the pretreatment, the steady-state activities of the

catalysts were measured at 120, 140, 160, 180, 200, 240, 280, 320, 360, and 400 °C under the full-feed conditions. For the full-feed test, a feed gas containing 5 vol.% H_2O, 5 vol.% CO_2, 6,000 ppm CO, 2,000 ppm H_2, 1,000 ppm C_3H_6, and either 0.5 vol.% O_2 for fuel-rich conditions (λ=0.95) or 1.35 vol.% O_2 for fuel-lean conditions (λ=1.05) (balanced with N_2) was introduced to the feed. The outlet gas concentration was recorded after reaching a steady state at each temperature.

(ii) NO storage and reactivity tests at a fixed temperature of 120 °C (full feed and simple feed): For the NO storage and reactivity tests, the samples were pre-treated at 700 °C with a ramping rate of 10 °C/min for 30 min with 5 vol.% O_2, 5 vol.% H_2O, and 5 vol.% CO_2 (balanced with N_2), and then cooled down to 120 °C (Scheme 3-1B), and the temperature was maintained at 120 °C. For the full feed test, the feed gas containing 0.5 vol.% O_2 for fuel-rich conditions (λ=0.95) or 1.35 vol.% O_2 for fuel-lean conditions (λ=1.05), along with 5 vol.% H_2O, 5 vol.% CO_2, 6,000 ppm CO, 2,000 ppm H_2, 1,000 ppm C_3H_6, and N_2 as a balance was introduced for 20 min to stabilize the catalysts. Subsequently, 100 ppm of NO was introduced. The concentration of the outlet NO was measured for 100 min. After 100 min, the temperature was raised to 500 °C at a ramping rate of 10 °C/min. Unless otherwise noted, NO storage and reactivity tests were conducted under full feed conditions. Further tests were conducted under simple feed conditions (i.e., 100 ppm NO, 2,000 ppm H_2, 0.5 or 1.35 vol.% O_2, and N_2

as a balance) to study the NO storage mechanism.

The effect of H_2O, CO_2 and C_3H_6 on the NO storage ability was also investigated. To prevent unwanted H_2O and CO_2 production, the experiments were conducted by a different procedure from ordinary experiments. Specifically, oxygen vacancies were produced over Pd/CeO_2 by reducing it under 5 vol.% H_2/N_2 condition at 400 °C in advance. During the NO adsorption step, the feed gas contained 100 ppm of NO (balanced with N_2), while 5 vol.% H_2O, 5 vol.% CO_2, 1,000 ppm C_3H_6 was included if needed. Neither H_2 nor CO was introduced to prevent the unwanted formation of H_2O and CO_2.

Since both NO reduction and NO storage occurred at 120 °C, the evaluation method was set to differentiate them. Within 100 min of flowing NO, the NO storage was saturated, and the NO concentration reached the steady-state value. The amount of NO removed by the reaction did not change significantly. Then, the areas above and below the steady-state NO concentration were calculated as reacted NO and stored NO, respectively.

(iii) Effect of λ variation: O_2 concentration was varied from 0.5 to 1.35 vol.% to change λ from 0.95 to 1.05 to investigate how the NO storage capacities and reduction activities are influenced by the λ variation. The concentrations of the other feed gases were maintained as those used in the full feed conditions (5 vol.% H_2O, 5 vol.% CO_2, 6,000 ppm CO, 2,000 ppm

H_2, 1,000 ppm C_3H_6). The same test was repeated for Pd(1)/CeO_2, Pd(2)/CeO_2, and Pd(3)/CeO_2 catalysts.

(iv) Cold-start simulations (100 s NO storage and λ switching tests): The NO abatement tests were also conducted for 100 s at 120 °C. After pre-treatment (Scheme 3-1), catalysts were exposed to the full feed (without NO) for 20 min. Afterward, 100 ppm of NO was introduced to the sample for 100 s. The amount of NO abatement was calculated from the difference with the NO concentration profile of the blank test in the absence of a catalyst. After the concentration of NO reached 0 ppm, the reactor was heated to 500 °C at a ramping rate of 10 °C/min to measure the amount of NO slipped from the sample.

The effectiveness of the λ control strategy on the abatement of NO emissions was also examined in the lab-scale experiments. After pretreatment, the full feed gas composition was injected to the catalyst at 120 °C. At the same time, the reactor was heated to 500 °C at an average ramp rate of 45 °C/min. For comparison, the tests were conducted under three different λ controls: (1) maintaining λ at 1.05, (2) maintaining λ at 0.95, and (3) switching λ from 1.05 to 0.95 at 250 °C.

A more realistic experiment was conducted using the facilities in Hyundai Motor Group. The simulated gas, similar to the lab-scale experiments but with more diverse hydrocarbon species, was introduced to

the after-treatment system and the NO emission was tracked. The λ value was switched from slightly fuel-lean conditions (λ > 1) to slightly fuel-rich conditions (λ < 1) at 15 s, while two after-treatment systems with and without Pd/CeO_2 components were compared.

3.2.3. Catalyst characterization

N_2 adsorption–desorption isotherms were obtained using a BELSORP-mini II (MicrotracBEL Corp.). The sample was degassed under vacuum at 200 °C for 4 h to eliminate any impurities. Brunauer–Emmett–Teller (BET) theory was used to estimate surface area. Cryo-H_2-TPR was conducted using a BELCAT II (MicrotracBEL Corp.). Samples (0.05 g) were oxidized under O_2 flowing conditions at 500 °C for 1 h and then cooled to -90 °C. The changes in thermal conductivity were measured using a thermal conductivity detector (TCD), while the catalyst was exposed to a 5 vol.% H_2/Ar gas flow while elevating the temperature from -90 to 900 °C (ramping rate of 10 °C/min). High-purity CuO (99.999%, Merck) was used to calibrate the TCD signal. The outlet stream was analyzed with a mass spectrometer (Hiden Analytical, QGA) if needed. *In situ* DRIFTS spectra were collected using an FT-IR spectrometer (Nicolet 6700, Thermo Fisher Scientific) equipped with a diffuse reflectance cell (Praying Mantis, Harrick Scientific Products Inc.) and an MCT detector. Pd(2)/CeO_2 powder (130 mg) was loaded onto the DRIFTS cell. Pretreatment was conducted under three different conditions: **(i)** O_2 treatment for 30 min at 400 °C, **(ii)** H_2

treatment for 30 min at 400 °C, and **(iii)** N_2 treatment for 30 min at 400 °C followed by O_2 and H_2 treatment with an 8:1 O_2/H_2 gas mixture for 30 min at 120 °C. After pretreatment, the samples were purged with N_2 for 30 min and then cooled. The background spectrum was obtained at 20 °C after each pretreatment. The DRIFTS spectra were collected after flowing 1 vol.% CO/N_2 to the sample for 1 h at 20 °C, followed by N_2 purging for 1 min at 20 °C to remove gas phase CO signal. High-angle annular dark-field scanning transmission electron microscopy (HAADF-STEM) and energy-dispersive X-ray spectroscopy (EDS) images were obtained using a JEM-ARM200F (JEOL Ltd.) with an accelerating voltage of 200 kV. The specimens were prepared by dispersing the powder samples in ethanol and dropping the colloidal solutions onto copper grids. It was challenging to distinguish the Pd particles from CeO_2, even in the HAADF mode. Conversely, in the case of Pd(5)/γ-Al_2O_3, 250 Pd particles were counted to get the particle size distribution curve. Pulsed CO chemisorption was conducted using BELCAT II. Typically, 0.05 g of the sample was heated at 400 °C under a He gas flow and cooled to 120 °C under He. The sample was then reduced using a 5 vol.% H_2/Ar mixture at 120 °C for 30 min, followed by purging with a He flow and cooling to -78 °C with a liquid nitrogen spray. The CO pulse was dosed in a He stream until the catalyst was saturated with CO. Pulsed CO chemisorption was performed at -78 °C to suppress CO adsorption on the CeO_2 surface and avoid overestimating the Pd dispersion [86]. The stoichiometric factor (the ratio between Pd atoms to chemisorbed

CO molecules) was assumed to be 1. The number of Pd atoms exposed on the surface is assumed to be the same as the number of chemisorbed CO molecules. X-ray diffraction patterns were recorded on a powder X-ray diffractometer (Smartlab, Rigaku) with a current of 30 mA and voltage of 40 kV in the 2θ range from 10° to 90°.

3.2.4. Density function theory (DFT) calculations

Periodic DFT calculations were performed using the Vienna Ab-initio simulation package (VASP) with projector-augmented wave (PAW) pseudopotentials. The RPBE-GGA exchange-correlation functional were used for all calculations with the fast algorithm, accurate precision, energy cutoff of 500 eV, and Gaussian smearing of 0.1 eV [87]. To treat electron over-delocalization in the strongly correlated system, the DFT+U method was used with the U_{eff} value of 4.5 eV for Ce. The slab models for Pd(111), CeO_2(111), and the Pd NP–CeO_2(111) interface are shown in Scheme 3-2. Each surface was separated by > 20 Å of vacuum space perpendicular to the slab surface, and the top two layers of the slab models as well as the adsorbates were allowed to relax until the forces on each atom were less than 0.03 eV/A. A Monkhorst-Pack k-point mesh of 4×4×1, 2×4×1, and 2×4×1 was used for Pd(111), CeO_2(111), and the Pd/CeO_2 interface, respectively. Gibbs free energies were obtained by applying zero-point energy (ZPE) and entropic corrections to the calculated electronic energies, which were either taken from the NIST database for gas molecules or

derived by calculating harmonic vibrational frequencies for adsorbates. To obtain activation barriers, the Climbing Image Nudged Elastic Band (CI-NEB) calculations were performed, and the exact transition state was identified by confirming one imaginary frequency of the Hessian.

Table 3-1. Composition of the feed gases in the NO storage and reactivity test.

Reaction condition		**Gas composition**
Pretreatment		5% O_2, 5% H_2O, 5% CO_2
Full feed	$\lambda = 1.05$	100 ppm NO, 5% H_2O, 5% CO_2, 1.35% O_2, 6000ppm CO, 2000 ppm H_2, 1000 ppm C_3H_6
	$\lambda = 0.95$	100 ppm NO, 5% H_2O, 5% CO_2, 0.5% O_2, 6000ppm CO, 2000 ppm H_2, 1000 ppm C_3H_6
Simple feed	$\lambda = 1.05$	100 ppm NO, 1.35% O_2, 2000 ppm H_2
	$\lambda = 0.95$	100 ppm NO, 0.5% O_2, 2000 ppm H_2
NO and N_2		100 ppm NO
NO, H_2O, and N_2		100 ppm NO, 5% H_2O
NO, H_2O, CO_2 and N_2		100 ppm NO, 5% H_2O, 5% CO_2
NO, H_2O, CO_2, C_3H_6, and N_2		100 ppm NO, 5% H_2O, 5% CO_2, 1000 ppm C_3H_6

The total flow was maintained at 200 ml/min (GHSV = 120,000 ml/h·g_{cat}) and balanced with N_2.

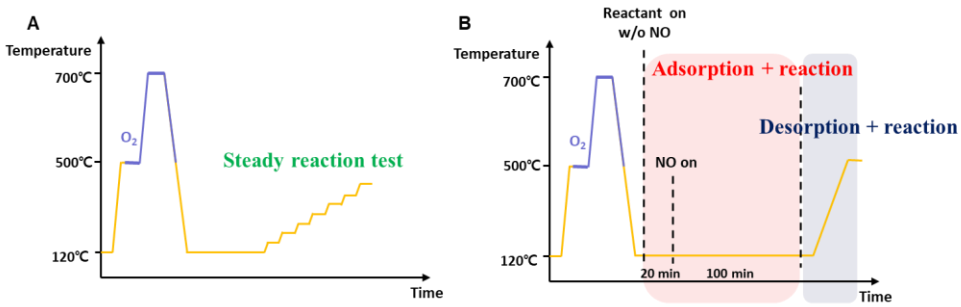

Scheme 3-1. The experimental protocols to evaluate (A) steady-state activity and (B) NO storage (during cold-start period) and NO reduction reactivity (while raising temperature) of the catalysts.

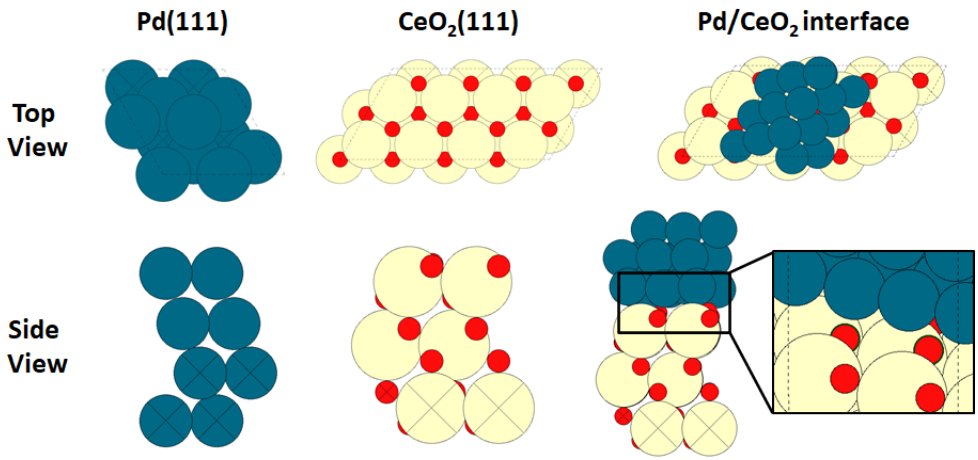

Scheme 3-2. The top and side views of the (2×2×4), (4×2×3), and (4×2×3) slab models for Pd(111), CeO_2(111), and the Pd NP–CeO_2(111) interface, respectively. The dark blue, yellow, and red indicate palladium, cerium, and oxygen atoms, respectively. Crossed atoms indicate fixed atoms during structural relaxations. Since it is difficult to know the exact structure of the Pd/CeO_2 interface, a quasi-one-dimensional Pd nanowire exposing a (111) facet supported on the CeO_2(111) surface was employed as a crude approximation of the actual complex Pd/CeO_2 interface. However, the quasi-one-dimensional periodicity largely avoids quantum size effects in the nanowire, and in contrast to sub-nanometer metal clusters, such nanowires may therefore serve as effective models of considerably larger Pd nanoparticles (diameter ≥ 2 nm, as in our experimental studies).[88] Many previous studies have shown the ability of these nanowire models to successfully describe and interpret crucial features of experimental kinetics.[89-91]

3.3. Results and Discussion

3.3.1. NO abatement abilities of catalysts

Figure 3-2 shows the amount of accumulated NO emitted from a commercial gasoline vehicle in time-on-stream along with the temperatures of engine-out gas and catalytic bed. During the cold-start period (< 20 s), the accumulated NO emissions increased drastically. However, the NO emission level barely increased above 500 °C, because the activated TWCs effectively converts NO into N_2. This shows that the majority (75.9%) of NO emissions from the gasoline vehicle occurs during the cold-start period.

One strategy for preventing NO emission during the cold-start is developing a catalyst active at low temperatures.[64, 92, 93] Various PGM-supported catalysts (Pd/γ-Al_2O_3, Pd/CeO_2, Pt-Pd/CeO_2, Pt/CeO_2, and Rh/CeO_2) were prepared and evaluated their NO reduction reactivities under steady-state operating conditions at the λ of 0.95 (Figure 3-3A). Note that the λ for gasoline vehicle exhaust should be less than 1.0 because the excess O_2 at λ > 1.0 completely oxidizes H_2 and CO, the reductants necessary for NO conversion [94]. Air to fuel ratio (AFR) is the mass ratio of air and fuel during the engine combustion. AFR determines several factors, such as the flammability of the fuel mixture, the amount of energy released, and the number of pollutants emitted during the combustion reaction. AFR that can burn all fuel mixtures without leaving excess air is called stoichiometric

AFR. Typically, the stoichiometric AFR is about 14.7:1 for gasoline fuel [95]. AFR greater than 14.7:1 is considered a fuel-lean condition, and AFR less than 14.7:1 is considered a fuel-rich condition. The engine's maximum power output is reached near the AFR of 12.6:1, whereas the AFR of about 15.4:1 is considered the maximum fuel economy ratio [96]. AFR changes continuously by engine control depending on the driving condition and environment, and this can be more simply expressed as air to fuel equivalence ratio, λ. λ is the ratio of actual AFR to stoichiometry for a given air and fuel mixture ($\lambda = AFR/AFR_{stoichiometric}$). For example, the maximum power can be achieved at a λ of 0.86 and best fuel economy can be achieved at a λ of 1.06. $\lambda = 1$ is at a stoichiometry, $\lambda > 1$ is a lean condition, and $\lambda < 1$ is a rich condition.

λ can be also determined by the composition of the exhaust gases from the engine outlet. There are several models to compare the idealized and the actual air to fuel ratio by comparing the molar ratio of oxygen molecules to carbon and hydrogen molecules in the exhaust gas components [97]. A simple expression using the volumetric concentration of each gases used in this study is as follows;

$$\lambda = \frac{[O_2] + 0.5[CO] + 0.5[H_2O] + [CO_2] + 0.5[NO]}{[CO] + 0.5[H_2] + 4.5[C_3H_6] + 0.5[H_2O] + [CO_2]}$$

For example, two representative λ value used in this study, 1.05 and 0.95, could be obtained by substituting the gas concentration values in the above

equation. Typically, the volumetric amount of H_2 emitted is about one third of that of CO emitted. The other gas concentrations were referred to the composition of gasoline exhaust provided by Hyundai Motor Group. C_3H_6 was used as a representative hydrocarbon component.

λ = 1.05: 100 ppm NO, 5% H_2O, 5% CO_2, 1.35% O_2, 6000ppm CO, 2000 ppm H_2, 1000 ppm C_3H_6

λ = 0.95: 100 ppm NO, 5% H_2O, 5% CO_2, 0.5% O_2, 6000ppm CO, 2000 ppm H_2, 1000 ppm C_3H_6

The λ value is important because it determines the operating window of three-way catalysts [98]. The highest conversion of CO, hydrocarbons, and NO_x can be achieved in a stoichiometric exhaust gas, λ = 1. Lean excursions with excess oxygen and lack of reductants decrease NO_x conversion. On the other hand, when λ is biased to a rich condition, the conversion of CO and hydrocarbons decreases. Since λ variation has a large impact on the performance of the catalytic converters, it is necessary to study how the after-treatment catalysts are affected by λ fluctuations. Based on this result, the engine control could be optimized to minimize pollutant emissions while increasing engine power and fuel efficiency. Therefore, a balance between catalyst activity and λ control by engine is crucial to ensure the high conversion of exhaust gas pollutants in gasoline vehicles.

In this context, Kim et al. previously investigated the effect of λ on the catalytic conversion of hydrocarbon, CO, NO, H_2 over Pt/Al_2O_3,

Pd/Al_2O_3, and $Pt\text{-}Pd/Al_2O_3$ [99]. Although the catalysts were different from the ones in this study, the trends in conversions of NO, CO, and hydrocarbons depending on the λ are similar. For example, regardless of catalyst species, NO conversions demonstrate volcano-shape at λ = 1.05 (Figure 3-4 and 3-5), whereas the light-off curves are observed at λ = 0.95 (Figure 3-3B). It is closely related to the oxidation of CO and C_3H_6, (Figure 3-5). Considering the adsorption energy of NO* (-2.05 eV) and O* (-0.86 eV) on Pd(111) surface, the oxidation of CO and C_3H_6 could occur by the reaction with NO, which would increase the NO conversion at low temperature. On the other hand, at the elevated temperatures, the number of dissociated O atoms would prevail at λ = 1.05. Hence, the NO conversion decreased at λ = 1.05, while the NO conversion continuously increased with temperature due to the lack of oxidant at λ = 0.95.

When discussing the oxidation activities of the catalysts, Pt surface is well known to be poisoned by CO, leading to the hampered oxidation activity for CO and C_3H_6 [99]. However, the incorporation of Pd to Pt clearly improved the oxidation ability [99]. Moreover, the active oxygen supplied by CeO_2 would further improve the oxidation activity of Pd/CeO_2 [100]. Meanwhile, Rh catalyst typically demonstrates the high NO conversion activity. However, the NO conversion over Rh/CeO_2 was lower than that of Pd/CeO_2, and the oxidation ability of Rh/CeO_2 was also lower than that of Pd/CeO_2. There should be more complex chemistries involved

with the activities of these catalysts, but they are out of scope of this study.

Figure 3-3A shows that almost 100% NO reduction is achieved over the Pd/CeO_2, Pt–Pd/CeO_2, and Rh/CeO_2 catalysts, but only above 250 °C. Considering that the time required to heat the catalytic bed to above 250 °C was longer than 11.5 s (Figure 3-2), a significant amount of NO would be slipped from the after-treatment system. Unfortunately, despite our efforts here, and those of others, to improve the low-temperature activity of TWCs, achieving 100% NO conversion below 150 °C remains considerably challenging [7, 64, 101].

Another strategy to remove NO emitted during the cold-start period is temporarily storing NO on the catalyst at low temperatures. Figure 3-3B displays the NO storage abilities of the PGM-supported catalysts (evaluated at 120 °C) at the λ of 0.95. Since both NO storage and reduction occur at 120 °C, the steady-state NO concentration at 120 °C was considered as the baseline to evaluate the NO storage ability (Figure 3-7). All CeO_2-based catalysts provided sufficient NO storage, while Pd/γ-Al_2O_3 did not store NO (Figure 3-3B). Moreover, when the catalyst bed temperature was increased, NO desorption and reduction simultaneously occurred within 170–300 °C (Figure 3-8). Note that the NO desorption curves in Figure 3-8 were obtained after exposure to NO for 100 min. When the samples were exposed to NO at 120 °C for 100 s, which is closer to realistic conditions (~ 20 s of the cold-start period), most of the desorbed NO was reduced to N_2 (Figure

3-9). Therefore, the NO emitted during the cold-start period can be temporarily stored and removed at the elevated temperature. Since Pd/CeO_2 exhibits the highest NO abatement ability among samples studied, its NO abatement behavior was further investigated.

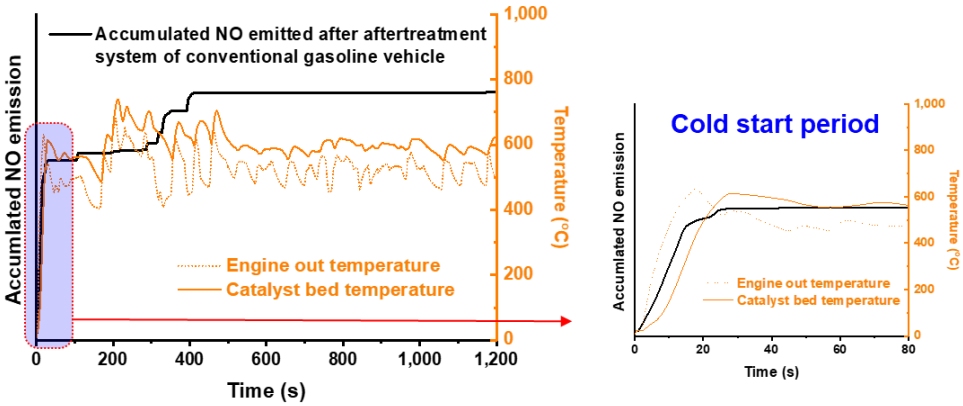

Figure 3-2. Accumulated NO emissions and the exhaust gas temperatures of the engine and catalyst bed during the first 1,200 s after starting the engine of a typical gasoline vehicle.

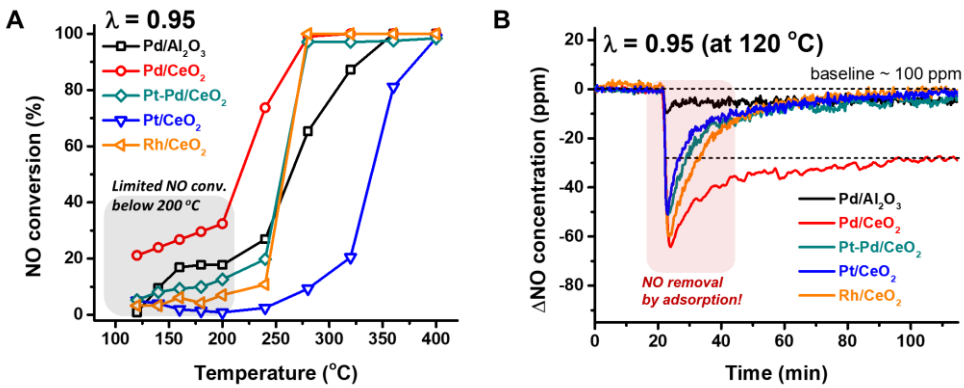

Figure 3-3. Cold-start NO emission and NO abatement activities of various catalysts. (A) Temperature-dependent NO reduction activities of the representative three-way catalyst (TWC) at an air-fuel equivalence ratio (λ) of 0.95. (B) NO abatement activities of various catalysts at a λ of 0.95 and temperature of 120 °C.

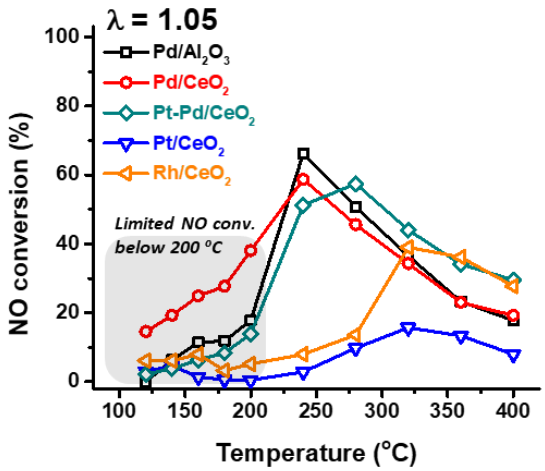

Figure 3-4. Steady-state NO reduction activities of the representative TWC catalysts at λ of 1.05.

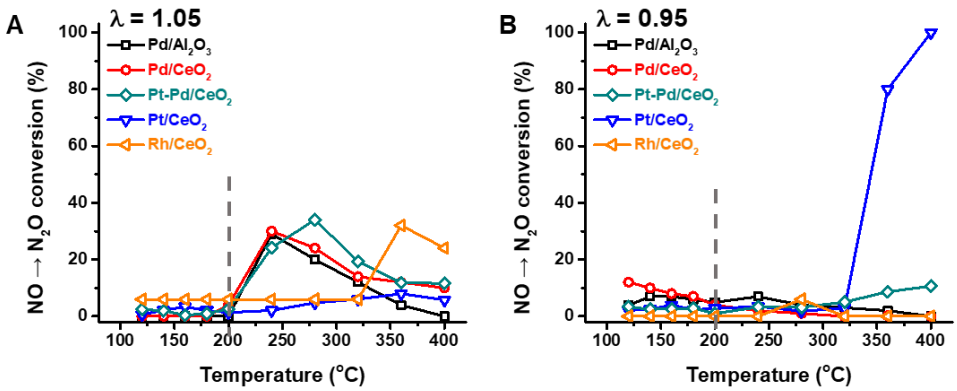

Figure 3-5. NO to N_2O conversion over various catalysts at (A) λ=1.05, and (B) λ=0.95.

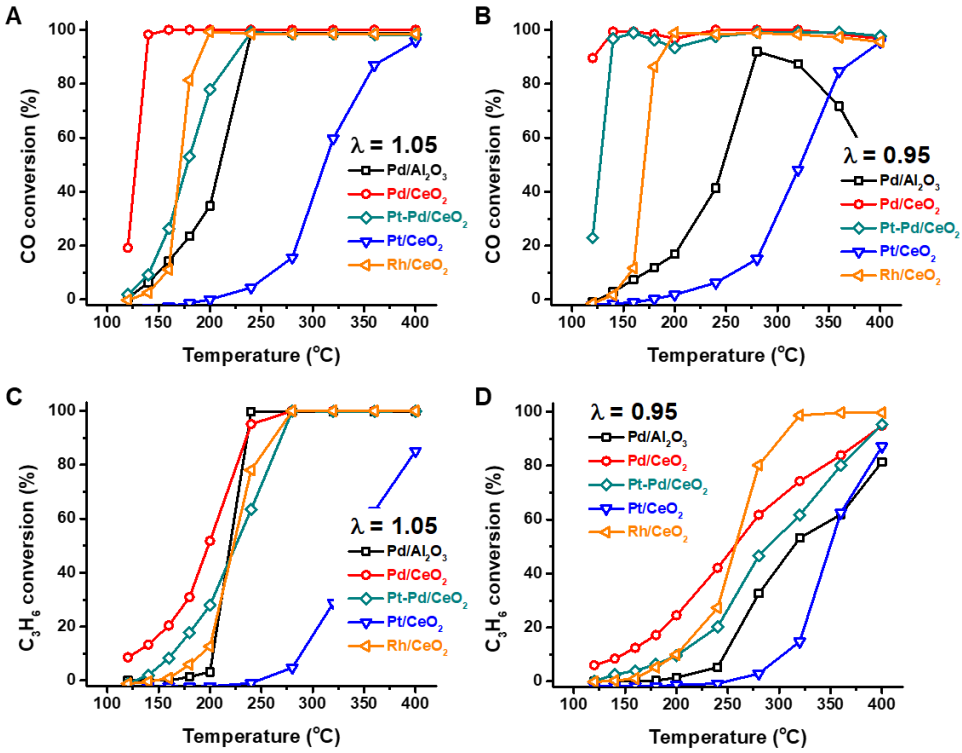

Figure 3-6. (A) CO conversion at λ=1.05, (B) CO conversion at λ=0.95, (C) C_3H_6 conversion at λ=1.05, and (D) C_3H_6 at λ=0.95 with temperature over various catalysts during the steady-state experiments.

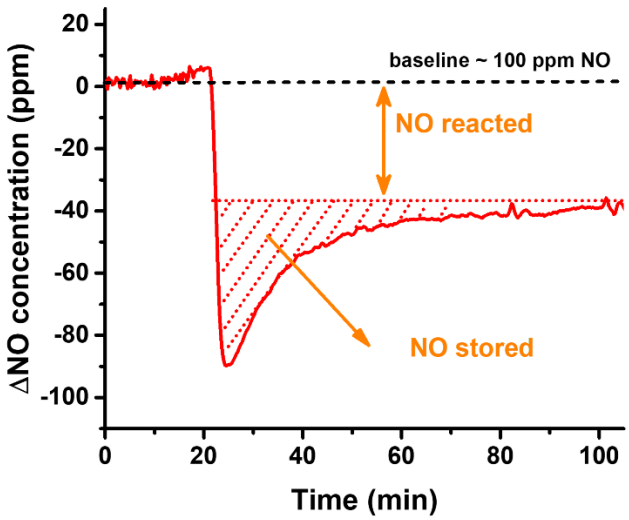

Figure 3-7. (A) CO conversion at λ=1.05, (B) CO conversion at λ=0.95, (C) C_3H_6 conversion at λ=1.05, and (D) C_3H_6 at λ=0.95 with temperature over various catalysts during the steady-state experiments.

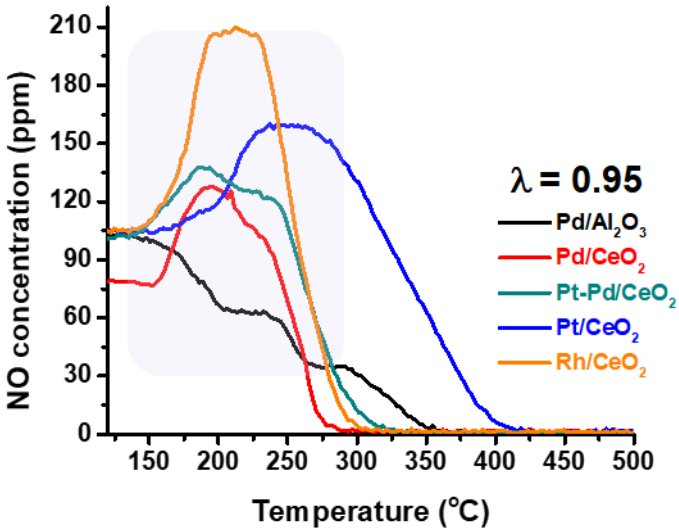

Figure 3-8. The changes in the NO concentration during temperature ramping after the NO storage at 120 °C for 100 min. The NO concentration is 100 ppm in the feed gas. Desorption and conversion of NO occur simultaneously when increasing the temperature.

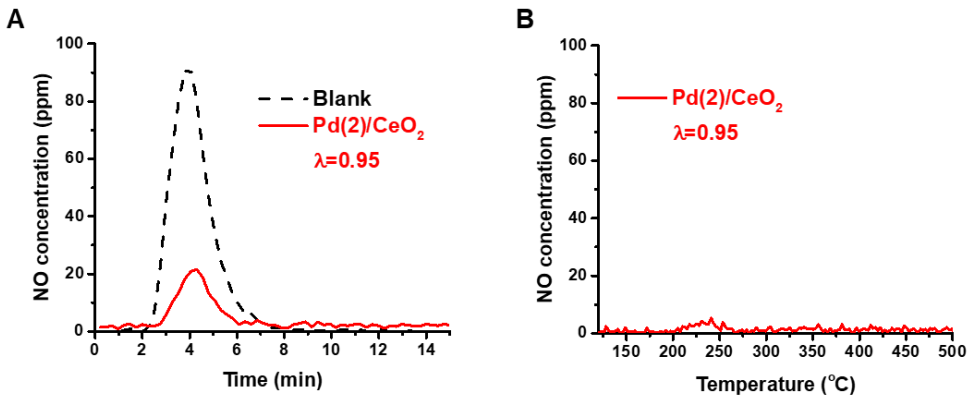

Figure 3-9. (A) The changes in NO concentration during the NO storage at 120 °C for 100 sec to simulate a cold-start period (generally within 20 sec), and (B) the desorbed NO while raising the temperature. NO_2, N_2O and NH_3 were not observed in adsorption and desorption processes.

3.3.2. Maximizing cold-start NO abatement via engine control

The development of gasoline vehicle technology over the past 50 years has enabled the facile manipulation of λ in exhaust gas by sophisticated engine control with a powertrain control module [102-104]. Therefore, although the λ in the exhaust gas is typically less than 1.0 during the typical operation of gasoline engine, it can be increased easily to above 1.0 if necessary. It is exploited that this advantage of engine technology in gasoline vehicles and investigated the effect of varying λ on the cold-start NO abatement ability of Pd/CeO_2.

When λ increased from 0.95 to 1.05, the NO storage amount increased from 24.5 to 30.7 μmol/g on Pd(1)/CeO_2 (the metal loading is shown in parentheses), and from 45.6 to 78.7 μmol/g on Pd(3)/CeO_2 (Figure 3-10A). Therefore, higher λ values benefit the catalyst NO storage ability. The effect of varying λ on the NO reduction activity is shown in Figures 3-10B and 3-10C. When λ increased from 0.95 to 1.05, the NO conversion decreased from 22.4% to 3.7% on Pd(1)/CeO_2, and from 64.5% to 17.8% on Pd(3)/CeO_2 (Figure 3-10B). Simultaneously, the N_2O selectivity decreased from 62.5% to 0% on Pd(1)/CeO_2 and from 57.9% to 10.5% on Pd(3)/CeO_2 (Figure 3-10C). Hence, although high NO conversion could be achieved at low λ, this conversion involved the conversion of NO to N_2O, which is an undesirable greenhouse gas with a stronger effect than CO_2 [105]. The NO abatement ability of Pd/CeO_2 at 120 °C can thus be summarized as follows:

NO storage was promoted at λ = 1.05. Conversely, NO reduction was promoted at λ = 0.95, but resulted in N_2O production. Maximizing the NO storage ability by increasing λ above 1.0 was found to be a suitable approach toward minimizing NO emissions during the cold-start period without producing N_2O (Figure 3-10). Moreover, λ should be switched from 1.05 to 0.95 when the exhaust temperature reaches 200 °C (Figure 3-11). This would maximize the NO storage capacity of Pd/CeO_2 at λ = 1.05 during the cold-start period (Figure 3-10A) and achieve high NO reduction activity at λ = 0.95 at elevated temperatures (Figure 3-3A and 3-4). This strategy, employing both engine control and catalytic reactivity to achieve zero NO emissions over the wide temperature range (Figure 3-12A), further reduced the amount of emitted NO by 25% by simply shifting λ from 1.05 to 0.95 at 250 °C, compared to the case where λ is constant at 0.95 (Figure 3-12B). Real-scale experiments were also conducted at the Hyundai Motor Group to confirm the feasibility of our approach under the simulated exhaust conditions of a typical gasoline vehicle (Figure 3-12C; see Experimental for details). Using our λ-switch strategy and incorporating the Pd–CeO_2 components in the TWC of a gasoline vehicle maximized the temporal NO storage, and successfully reduced NO emissions by 67.6% during the cold-start period.

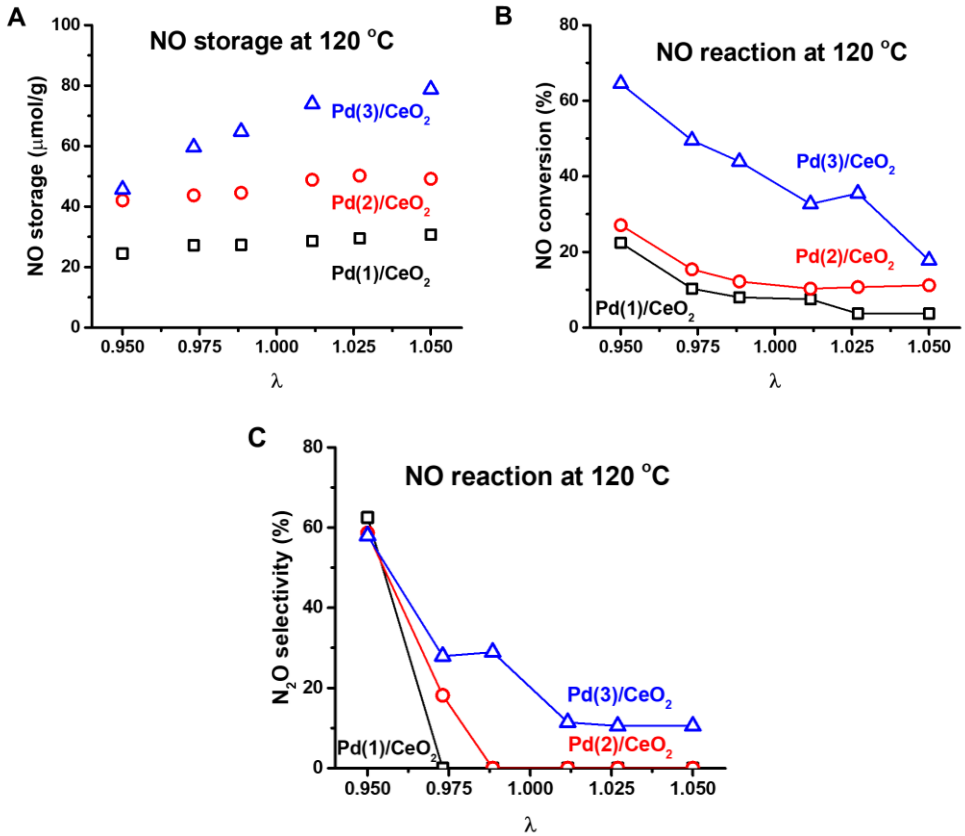

Figure 3-10. Effect of λ variation on the NO abatement abilities of Pd/CeO_2 catalysts. Effect of λ variation on (A) NO storage abilities, (B) NO conversion by reduction, and (C) N_2O selectivity of Pd/CeO_2 catalysts with different Pd loadings (1–3 wt.%) at 120 °C. The λ value was varied from 0.950 to 1.050.

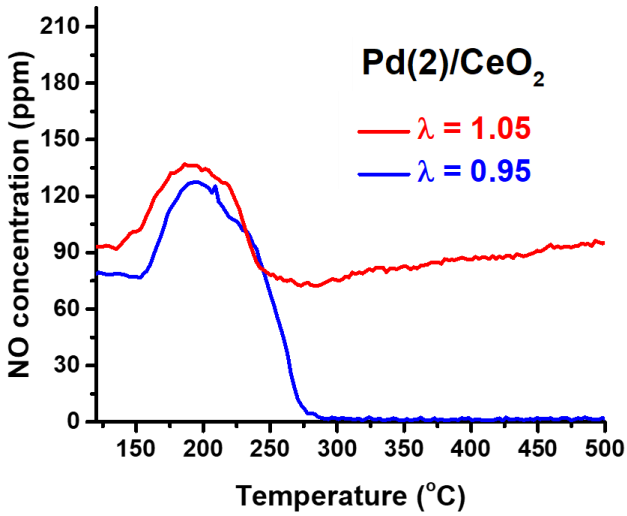

Figure 3-11. NO concentration profile while raising the temperature from 120 to 500 °C at a ramping rate of 10 °C/min after flowing NO at 120 °C for 100 min to Pd(2)/CeO_2 at the λ of 0.95 and 1.05.

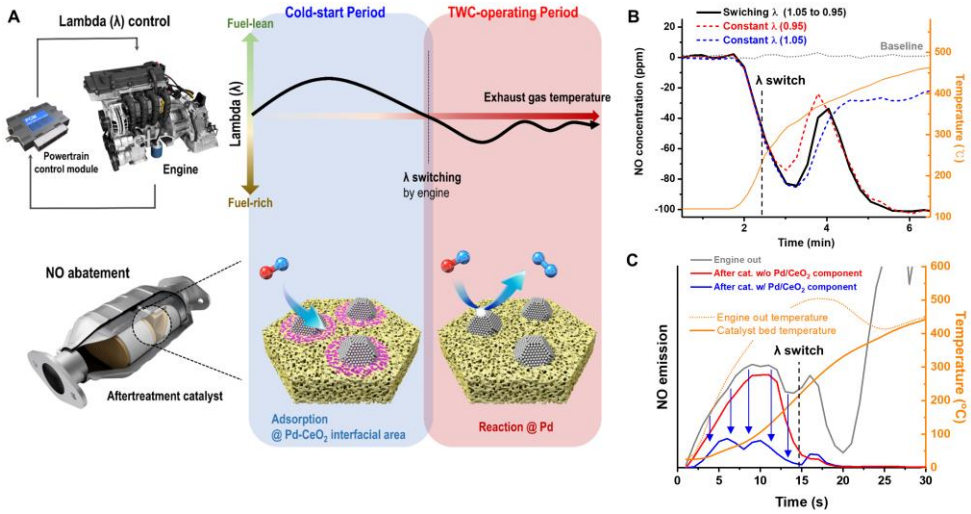

Figure 3-12. Maximizing the NO abatement ability of Pd/CeO_2 catalyst through the engine control. (A) Schematic illustration of the λ control under slightly fuel-lean conditions during the cold-start period and under slightly fuel-rich conditions in the TWC-operating region. The powertrain control module was used to manipulate the λ value of the gasoline combustion, maintaining it above 1 during the cold-start period to facilitate NO adsorption and prevent N_2O formation. As the exhaust gas temperature rises, the λ was switched to slightly below 1 (i.e., near-stoichiometric conditions) to promote NO reduction. (B) Lab-scale NO abatement ability of Pd(2)/CeO_2 was evaluated under the simulated cold-start period by switching λ from 1.05 to 0.95 at ~250 °C and comparing the resultant NO abatement to that evaluated under constant-λ conditions (1.05 or 0.95). (C) Real-scale NO abatement ability of Hyundai Motor Group catalyst with and without Pd–CeO_2 components. Here, the λ switching strategy was applied to maximize the NO abatement ability of the CeO_2 component.

3.3.3. Identification of the NO storage sites on Pd/CeO_2

The NO storage sites on Pd/CeO_2 were further investigated to elucidate their NO abatement ability. A series of experiments were conducted to identify the primary NO storage site on Pd/CeO_2 among the Pd surface, CeO_2 surface, or Pd–CeO_2 interface.

The NO amount stored on Pd/CeO_2 with Pd loadings of 0.05, 0.5, 1, 2, 3, and 4 wt.% was evaluated at $\lambda = 1.05$ and 0.95 and under both a simple feed (i.e., NO, O_2, H_2, and N_2 (balance)) and a simulated full feed (i.e., NO, O_2, H_2, CO_2, H_2O, C_3H_6, and N_2 (balance)). Pd exists as metallic Pd even at $\lambda = 1.05$ as will be discussed in 3.3.4. The amount of stored NO was quantitatively compared to the number of exposed metallic Pd sites, which was estimated by CO chemisorption (Figure 3-13). The amount of stored NO exceeded the number of exposed Pd sites on Pd/CeO_2 under the simple feed (Figure 3-14A), but it was lesser than the number of exposed Pd sites on Pd/CeO_2 under the full feed (Figure 3-14B). This indicates that the full feed components that were not present in the simple feed inhibit the NO storage on Pd/CeO_2. Further, in both cases, the NO amount stored on Pd/CeO_2 increased as the number of exposed Pd sites increased.

The correlation between the stored NO amounts and the number of exposed Pd sites implies that Pd plays an important role in storing NO. However, the 4 nm-sized Pd NPs of Pd(5)/γ-Al_2O_3 showed low NO storage

ability at $\lambda = 1.05$ unlike Pd(2)/CeO_2 (Figure 3-15). These results indicate that, although Pd surfaces are important for NO adsorption, the support material also plays a significant role in completing the NO storage mechanism. It is believed that the adsorbed NO is not simply kept on Pd, but gets converted to N_2, N_2O, or NO_2 depending on reaction conditions. In addition, the Pd surface may also indirectly contribute to the NO storage process by promoting V_O formation at the Pd-NP–CeO_2 interface. This will be discussed in detail below based on extensive DFT calculations.

The NO storage ability of Pd(2)/CeO_2 was also investigated under feeds consisting of (i) NO and N_2, (ii) NO, H_2O, and N_2, (iii) NO, H_2O, CO_2, and N_2 (iv) NO, H_2O, CO_2, C_3H_6, and N_2. The stored NO amount decreased from 77.3 to 63.7 μmol/g when H_2O was added to the feed, but further decreased to 20.2 μmol/g when CO_2 was added (Figure 3-14C). CO_2 is known to strongly interact with the CeO_2 surface; therefore, the significant inhibitory effect of CO_2 on the NO storage ability implies that the CeO_2 surface stores NO or NO_2 at low temperatures [106, 107]. Notably, despite its reduced NO storage ability in the presence of CO_2 (as well as H_2O and C_3H_6), Pd/CeO_2 exhibited a sufficient NO storage ability to remove most of the NO released during the cold-start period (i.e., < 20 s) (Figure 3-12C).

As the Pd–CeO_2 interactions seem to be key contributors in NO storage, a method of estimating the Pd–CeO_2 interfacial area was devised to quantitatively evaluate its NO storage ability. After oxidative treatment at

500 °C, the surface areas of CeO_2 and Pd(2)/CeO_2 were 125 m^2/g (Figure 3-14D). However, after oxidative treatment at 800 °C, the surface area of Pd(2)/CeO_2 (108 m^2/g) was larger than that of CeO_2 (70 m^2/g). This indicates that the Pd–CeO_2 interface prevents the thermal sintering of CeO_2 support [43, 108, 109]. The surface area of Pd/CeO_2 measured after oxidation at 800 °C increased as the Pd loading increased from 0.05 to 4 wt.% (Figure 3-14E). This improvement in the thermal stability of Pd/CeO_2 can be attributed to a larger Pd–CeO_2 interfacial area at higher Pd loading. Indeed, Figures 3-14D and 3-14E imply that the interfacial area of Pd/CeO_2 can be quantitatively deduced from the change in the surface area after 800 °C-treatment.

As the surface area of Pd/CeO_2 increased, the amount of NO stored on the sample also linearly increased (Figure 3-14F); this linear correlation strongly indicates that the CeO_2 surface is the storage site for NO at a low temperature. Interestingly, the x-intercept of the linear correlation line in Figure 3-14F was non-zero (70 m^2/g). The non-zero x-intercept suggests that the CeO_2 surface alone does not store NO and is consistent with our experimental observation that bare CeO_2 does not store NO (Figure 3-15). In other words, Pd of Pd/CeO_2 plays a major role in the NO storage mechanism. Note that some deviation from the linear correlation was observed at the higher Pd loadings (3 and 4 wt. %, Figure 3-14F), probably due to the formation of significantly larger Pd clusters (Figure 3-13).

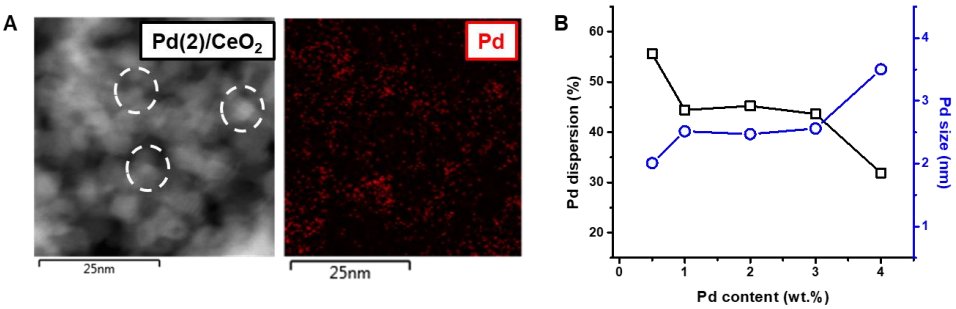

Figure 3-13. (A) HAADF-STEM image and EDS mapping showing the Pd distribution of Pd(2)/CeO_2, and (B) Pd dispersion and NP size of Pd/CeO_2 catalysts obtained from CO chemisorption at -78 °C.

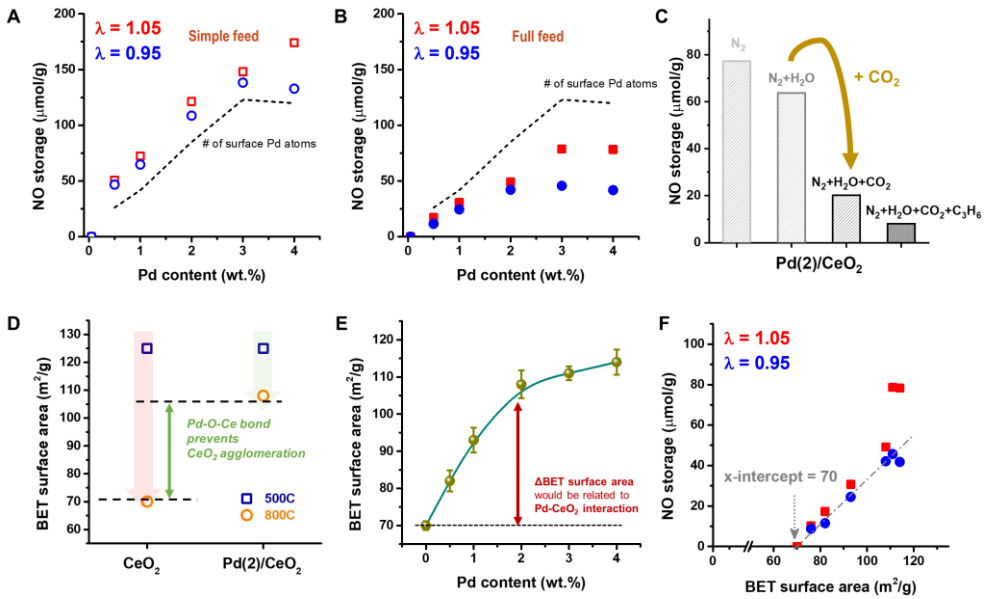

Figure 3-14. CeO_2 surface interacting with Pd nanoparticles (NPs) stores NO during the cold-start period. NO storage abilities of the Pd/CeO_2 samples with different Pd loadings under (A) simple feed (NO, H_2, O_2, N_2) and (B) full feed (NO, H_2, O_2, CO, C_3H_6, N_2) conditions; the Pd loading was increased from 0 to 4 wt.%. (C) Effect of adding H_2O, CO_2 or C_3H_6 to the feed on the NO storage ability of Pd(2)/CeO_2. (D) Change in the Brunauer–Emmett–Teller (BET) surface area of the CeO_2 and Pd(2)/CeO_2 samples when the oxidation temperature was increased from 500 to 800 °C. (E) The dependence of the BET surface area of Pd/CeO_2 samples, which were oxidized at 800 °C, on the Pd loading. (F) Correlation between the NO storage abilities at the λ of 1.05 and 0.95 and the BET surface areas of Pd/CeO_2 samples with different Pd loadings.

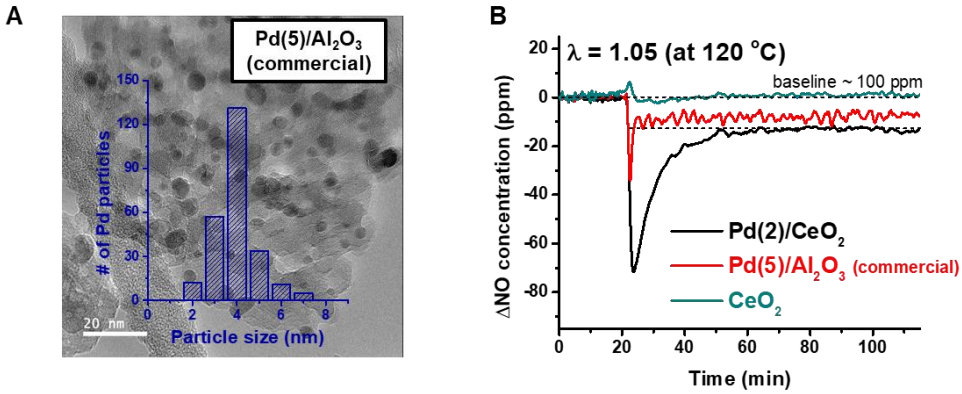

Figure 3-15. (A) TEM image and Pd size distribution of commercial Pd(5)/Al_2O_3, and (B) the comparison of NO storage abilities of Pd(5)/Al_2O_3, CeO_2 with Pd(2)/CeO_2. Only Pd(2)/CeO_2 demonstrates the NO storage ability, indicating that interfaces between Pd and CeO_2 play a crucial role in storing NO.

3.3.4. State of Pd/CeO_2 catalyst's surface under working conditions

The state of the Pd/CeO_2 surface under working conditions was investigated to further reveal the active sites for NO storage. Both O_2 and H_2 are present in the exhaust gas of gasoline vehicles. The color of oxidized Pd/CeO_2 changed from yellow to dark brown after treatment with H_2 at 400 °C (Figure 3-16A). Interestingly, the color of oxidized Pd/CeO_2 also became dark even after treatment with an 8:1 O_2/H_2 mixture at 120 °C (Figure 3-16A).

In situ CO adsorption diffuse reflectance infrared Fourier-transform spectroscopy (DRIFTS) spectra of Pd(2)/CeO_2 were collected after pretreatment with O_2 at 400 °C, with H_2 at 400 °C, or with O_2/H_2 (8:1) at 120 °C. The sample was then cooled to 35 °C under N_2 before collecting the spectra. After O_2 treatment, Pd existed as Pd^{2+}; however, after H_2 treatment, Pd existed as Pd^0 (Figure 3-16B) [110-112]. Interestingly, even after treatment with O_2/H_2 (8:1) at low temperatures, oxidized Pd was reduced by the minor H_2 component despite the presence of the excess amount of O_2. Thus, the Pd in Pd/CeO_2 catalysts would exist in the reduced state at λ = 1.05 during the cold-start period.

The H_2-temperature-programmed reduction (TPR) curve of Pd(2)/CeO_2 reduced and re-oxidized at 120 °C was compared to those of pristine CeO_2 and bulk PdO. Unlike CeO_2, the Pd(2)/CeO_2 surface was

reduced even below room temperature (Figure 3-16C). This would be ascribed to metallic Pd NPs (Figure 3-16B) promoting the partial reduction of the CeO_2 surface by activating H_2 at the lower temperature. Mass spectrometry measurements also show that the consumed H_2 produces H_2O leaving V_Os on CeO_2 (Figure 3-17). This role of Pd NP is also studied by DFT calculations. Upon comparing the free-energy diagrams for V_O formation by H_2 on the pristine CeO_2 surface and at the Pd-NP–CeO_2 interface, the presence of metallic Pd NPs considerably promote the homolytic dissociation of H_2 (Figure 3-16D) [113, 114]. Consequently, the highest free-energy barrier for V_O formation by H_2 decreases significantly from 2.04 eV (homolytic H_2 activation to 2H* is considered as rate determining step (RDS) on pure CeO_2 surface) to 1.16 eV (RDS is H_{Pd}* + H_O* → H_2O + V_O at the Pd-NP–CeO_2 interface).

Figure 3-16D compares the calculated free energy diagrams for hydrogen reacting with lattice oxygen of CeO_2 to form an oxygen vacancy and water at the Pd/CeO_2(111) interface vs on the pristine CeO_2(111) surface. It can be seen that both the homolytic dissociation of hydrogen and the diffusion of hydrogen atoms are particularly difficult on the pristine CeO_2(111) surface. This is because, their transitions states are found to be fairly unstable due to a relatively long distance (4 Å) between the lattice oxygens. Thus, it is believed that V_O formation by H_2 would be promoted particularly near the Pd nanoparticles. For the CeO_2(111) surface far away

from the Pd nanoparticles, V_O formation may occur by a different reductant such as CO particularly at high temperature.

Since V_O formation by H_2 is found to be highly feasible at the Pd/CeO_2(111) interface, the free-energy diagram for the second V_O formation have obtained (Figure 3-18). It can be seen that the second V_O formation is thermodynamically quite feasible with the highest reaction energy of 0.71 eV, indicating that the V_O concentration at the interface can be as high as 2/2 = 100% under the reaction condition. This is the reason why the Pd/CeO_2 interfaces with different V_O concentrations are considered (Interface*X* represents the Pd/CeO_2 interface with X % of Vo concentration). In addition, once H_2 is activated on the Pd surface, the activated H atoms readily spill over onto the CeO_2 surface to react with oxygen to form an oxygen vacancy and water, in agreement with previous reports [75, 115-118]. In summary, the combined *in situ* CO-DRIFTS spectra, H_2-TPR curves, and DFT calculations indicate that both Pd and CeO_2 surfaces would exist in the reduced state during the cold-start period, even at λ = 1.05, owing to the presence of H_2.

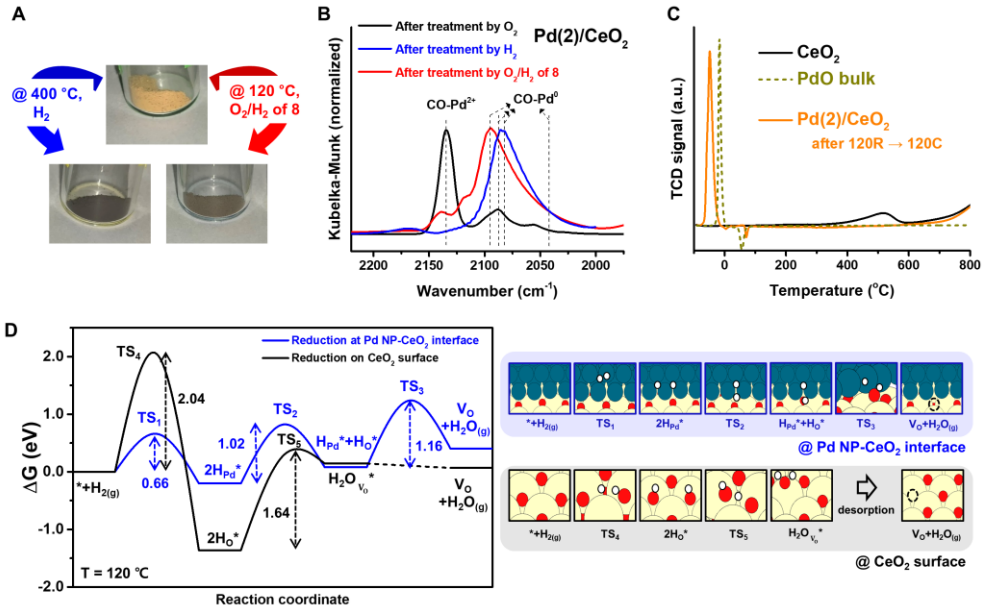

Figure 3-16. Identifying the state of the Pd NPs and CeO_2 surface under working conditions. (A) Color of Pd(2)/CeO_2 after H_2 treatment at 400 °C or after O_2/H_2 (8:1 in volumetric ratio) treatment at 120 °C. (B) *In situ* CO-diffuse reflectance infrared Fourier-transform spectroscopy (DRIFTS) spectra of Pd(2)/CeO_2 after treatment by O_2 or H_2 at 400 °C or by O_2/H_2 at 120 °C. (C) H_2-temperature-programmed reduction (TPR) curve of Pd(2)/CeO_2 (reduced and re-oxidized at 120 °C) compared to those of pristine CeO_2 and PdO bulk. Reduction of CeO_2 surface, bulk PdO, and Pd(2)/CeO_2 surface consumed 0.22, 0.24, and 0.44 mmol/g_{cat} of H_2, respectively. Here, the reduction of Pd/CeO_2 surface would include the reduction of PdO and CeO_2 surface. (D) The calculated free-energy diagram for oxygen vacancy (V_O) formation by H_2 on the pristine CeO_2 surface vs. at the Pd-NP–CeO_2 interface at 120 °C with the configurations of each step during reduction.

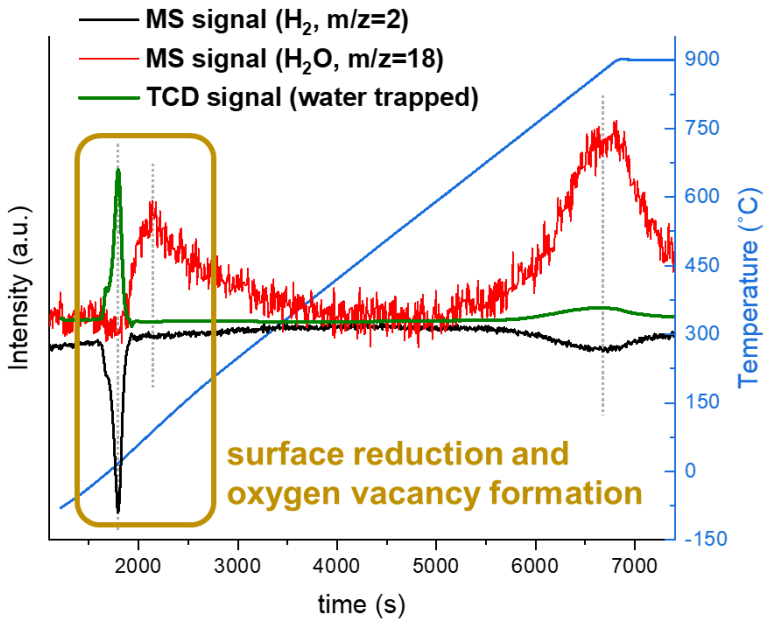

Figure 3-17. H_2-TPR curve of Pd(2)/CeO_2 after oxidative pretreatment at 400 °C. TCD and mass spectrometer were used together to analyze the outlet stream. Since TCD can only detect the consumption of H_2, a mass spectrometer was used to confirm the formation of H_2O and V_Os. Although quantitative analysis cannot be accurately performed using a mass spectrometer, it can be seen that H_2O was generated by the reaction of H_2 and O of CeO_2 based on the peak position.

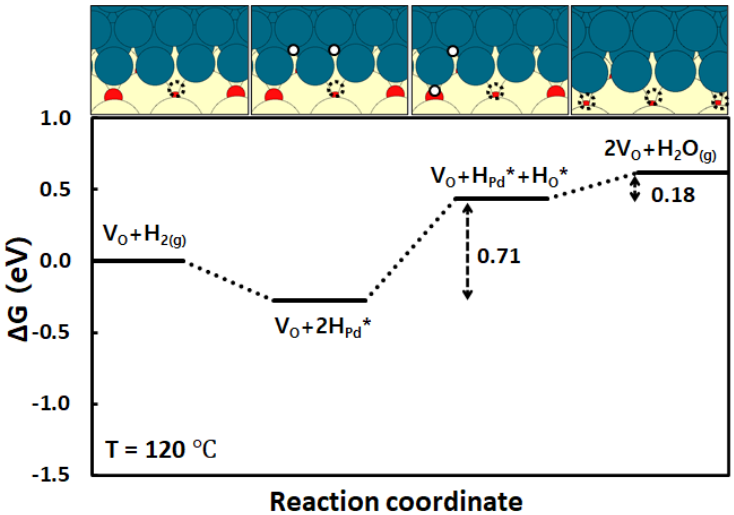

Figure 3-18. The free energy diagram of second oxygen vacancy (V_O) formation at the Pd/CeO_2 interface under the reaction condition (T = 120 °C). The dark blue, yellow, and red indicate palladium, cerium, and oxygen atoms, respectively. The subscripts "Pd" and "O" represent the Pd and lattice oxygen sites at the Pd/CeO_2 interface.

3.3.5. Investigation of the NO storage mechanism at the Pd NP–CeO_2 interface

Because PGMs have high NO oxidation ability, NO adsorbed on Pd/CeO_2 has the potential to be oxidized to NO_2. DFT calculations were employed to investigate the competition between NO* desorption and NO* oxidation to NO_2 on the Pd(111) surface vs. at the Pd NP–CeO_2(111) interface with different V_O concentrations. Figure 3-19A shows that NO* oxidation to NO_2 is favored over NO* desorption at the Pd-NP–CeO_2(111) interface with V_O concentrations of 50 % and 100 %, probably because the free energies of all the transition states involved in the former pathway are lower than that required to desorb NO* thermodynamically. Interestingly, the Pd NP–CeO_2 interface modified by the V_Os created slightly under the Pd atoms significantly stabilizes NO_2* compared to other intermediates such as NO* and O* (Figure 3-20 and 3-21). This is because of a unique adsorption configuration of NO_2* at the Pd NP–CeO_2 interface, which adsorbs through two oxygen atoms forming a bidentate structure at the interface whereas it adsorbs through one nitrogen atom forming a monodentate structure on Pd(111) (Figure 3-22). Therefore, the Pd NP–CeO_2 interface modified by V_Os promote NO* + O* → NO_2* by significantly stabilizing the final and transition states (Figure 3-19A). Once NO_2* is formed and accumulated at the Pd NP–CeO_2 interface, it will desorb as NO_2 since adsorbate-adsorbate interactions will weaken its adsorption strength. A couple of questions then

arise as to what happens to NO_2 produced at the Pd NP–CeO_2 interface, why NO_2 was not detected as final products in our experiments, and why the NO storage ability was slightly better at higher λ (Figure 3-10A) where less V_Os would be formed at the interface. It is possible to suggest that, at low temperatures (T < 120 °C), the NO_2 would be easily captured by V_O formed by H_2 near the Pd clusters (Figure 3-16D). At elevated temperature (T > 300 °C), the captured NO_2 will be released as NO, leaving its one oxygen atom to fill V_O, as shown in our DFT calculations (Figure 3-23). The improved NO storage ability of Pd/CeO_2 at higher λ can then be explained as follows. Although more V_O will generally promote NO* + O* → NO_2*, higher λ is desired to promote O_2 → 2O*, which is found to be the RDS for NO oxidation to NO_2 at the Pd/CeO_2 interface with e.g. 100% of V_O concentration (Figure 3-19A).

In addition to the NO storage on Pd/CeO_2, NO* reduction to N_2O (mainly at low λ) or N_2 (mainly at high λ) was also observed at 120 °C (Figure 3-10). Hence, the reaction energetics of NO* reduction to N_2 via H-assisted NO dissociation mechanism (Figures 3-24 and 3-25) on the Pd(111) surface vs. at the Pd NP–CeO_2(111) interface with a V_O concentration of 100% (Figure 3-19B) were investigated [92]. Evidently, V_Os created at the interface increased the highest free-energy barrier for NO* reduction to N_2 from 1.91 eV (RDS is 2N* → N_2 on the Pd(111) surface) to 2.10 eV (RDS is HNO* → NH* + O* at the Pd-NP–CeO_2 interface). This is because a

relatively stable adsorption configuration was possible for HNO* only at the Pd/CeO_2 interface. Figure 3-26 shows that HNO* adsorbs through its nitrogen and oxygen atoms forming a bidentate structure at the interface, whereas it adsorbs through one nitrogen atom forming a monodentate structure on Pd(111). Thus, the effect of V_O is to suppress NO reduction by significantly stabilizing HNO*, which increases the activation barrier for H-assisted NO dissociation (HNO* → NH* + O*).

The proposed mechanism for NO abatement by Pd NP–CeO_2 is schematically illustrated in Figure 3-19C. Overall, DFT calculations showed that NO* oxidation to NO_2 mainly occurs at the Pd NP–CeO_2 interface promoted by the V_Os created at the interface (i.e., slightly under Pd atoms). Meanwhile, NO* reduction to N_2O or N_2 primarily occurs on metallic Pd and is promoted by H* adsorbed on the Pd surface. This is consistent with the observation of NO storage only on ceria-supported samples, but not on alumina-supported sample (Figure 3-3B). It is worth mentioning that the concentration of V_O was not measured experimentally in this study. Thus, future studies will require experimental validation of the proposed mechanism. Here, *in-situ* studies (e.g., *in-situ* XPS) will be needed to measure V_O concentration as reduced CeO_2 can be rapidly re-oxidized by ambient air.

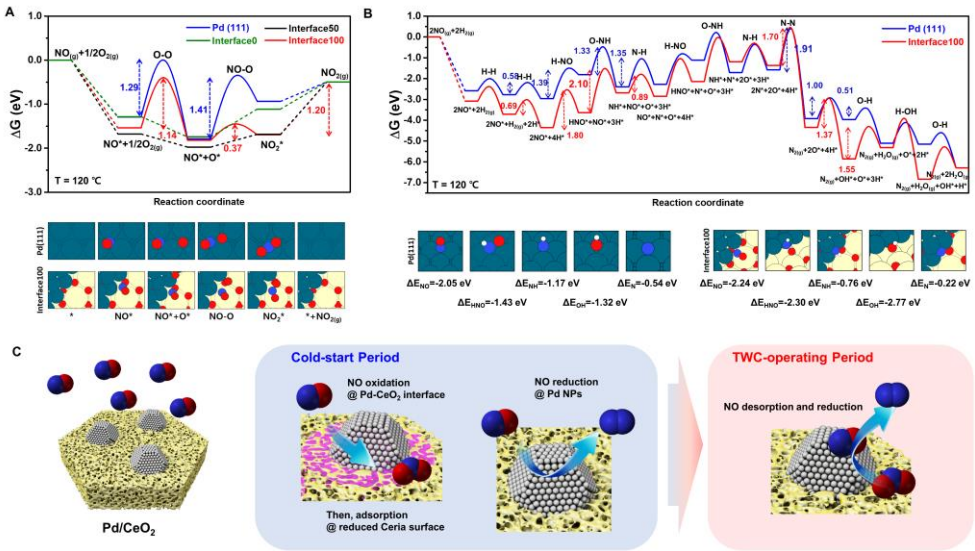

Figure 3-19. NO storage and reduction mechanism of Pd/CeO_2 with V_Os. (A) The calculated free-energy diagrams for NO oxidation on the Pd(111) surface vs. at the Pd NP–CeO_2 interface with different V_O concentrations (InterfaceX represents the Pd NP–CeO_2 interface with a Vo concentration of X%). (B) The free-energy diagram for NO reduction to N_2 via H-assisted NO dissociation on the Pd(111) surface vs. at the Pd-NP–CeO_2 interface with a V_O concentration of 100%. The configuration for each reaction step and the adsorption energy for each reaction intermediate are shown below the free-energy diagram. (C) The schematic illustration of the NO abatement mechanism for Pd/CeO_2 with V_Os.

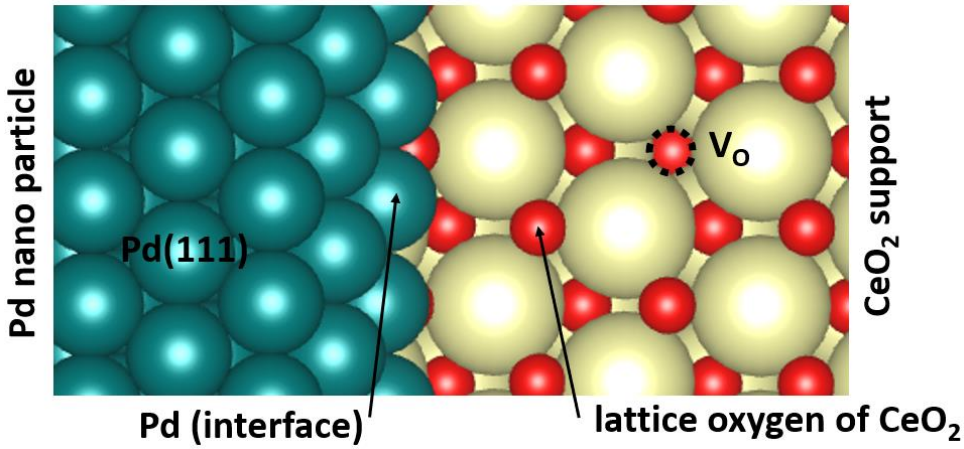

Figure 3-20. A cartoon showing various adsorption sites for Pd/CeO_2: the Pd site of Pd(111) and at the interface, the lattice oxygen site at the interface and on CeO_2(111), and the oxygen vacancy (V_O) site of CeO_2(111). The dark blue, yellow, and red indicate palladium, cerium, and oxygen atoms, respectively.

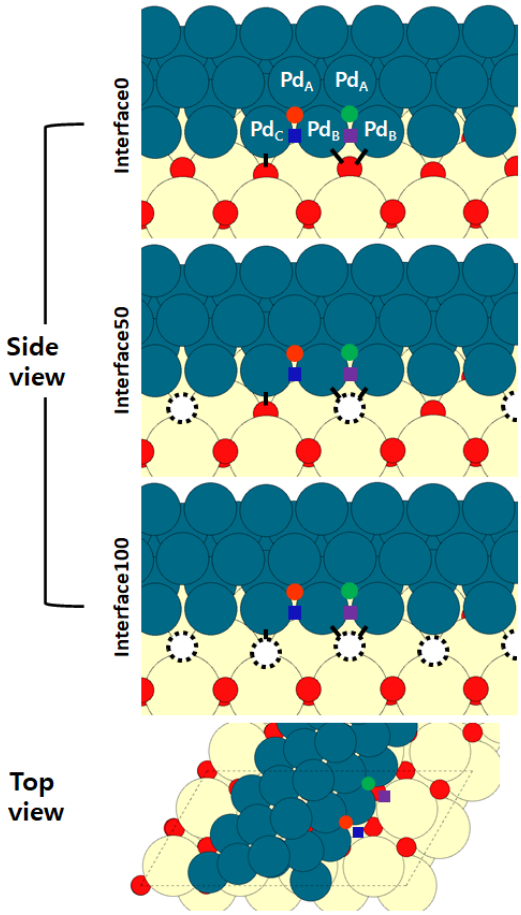

Surface	Adsorbate	Adsorption site	ΔE (eV)
Pd(111)	NO*	3fold	-2.05
	NO_2*	On top	-1.08
	N*	3fold	0.82
	O*	3fold	-0.86
	H*	3fold	-0.37
	CO*	3fold	-1.51
Interface0	NO*	Orange	-2.07
	NO_2*	Purple	-1.25
	N*	Orange	0.87
	O*	Orange	-0.83
	H*	Orange	-0.40
	CO*	Orange	-1.62
Interface50	NO*	Purple	-2.38
	NO_2*	Purple	-1.80
	N*	Orange	1.06
	O*	Orange	-0.66
	H*	Purple	-0.55
	CO*	Purple	-1.82
Interface100	NO*	Purple	-2.24
	NO_2*	Purple / Blue	-1.86
	N*	Green / Orange	1.14
	O*	Green / Orange	-0.62
	H*	Purple	-0.55
	CO*	Purple	-1.69

Figure 3-21. The top and side views of the slab models for the Pd/CeO_2 interface with different concentrations of oxygen vacancies (V_O). The *X* in Interface*X* indicates the % of Vo concentration at the interface (*X* = 0/2, 1/2, and 2/2). The table on the right shows the calculated adsorption energies of different adsorbates at different adsorption sites. The orange and green circles indicate the 3-fold sites, and the blue and purple squares indicate the bridge sites. Pd_A, Pd_B, and Pd_C indicate the Pd atoms coordinated by different atoms.

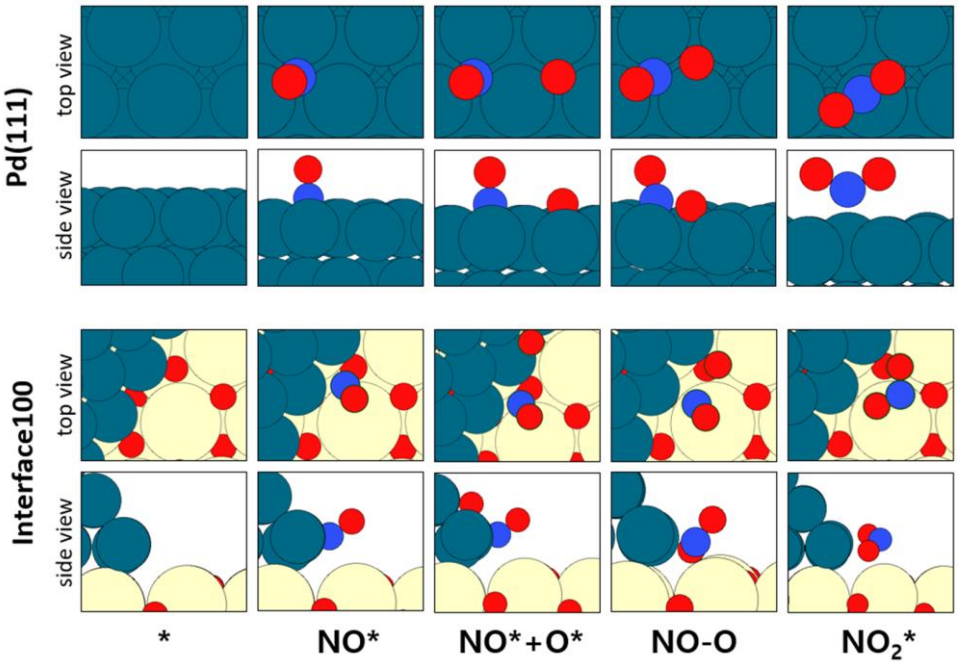

Figure 3-22. Cartoons showing the NO oxidation pathway on Pd(111) surface vs Interface100.

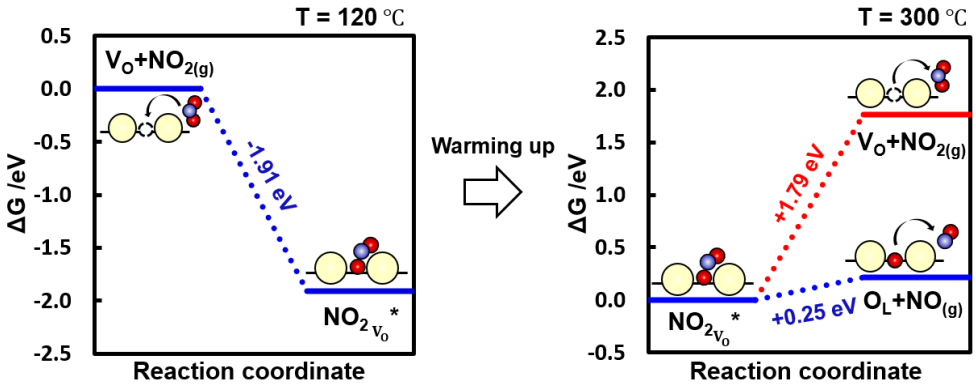

Figure 3-23. NO_2 strong adsorbs on V_O of CeO_2 during the cold-start period. When the temperature is elevated, the adsorbed NO_2* is desorbed as NO leaving oxygen atom at the oxygen vacancy. Free energy diagram indicates that NO desorption is thermodynamically favorable than NO_2 desorption on CeO_2. The yellow, blue, and red indicate Cerium, Nitrogen, and Oxygen atoms, respectively.

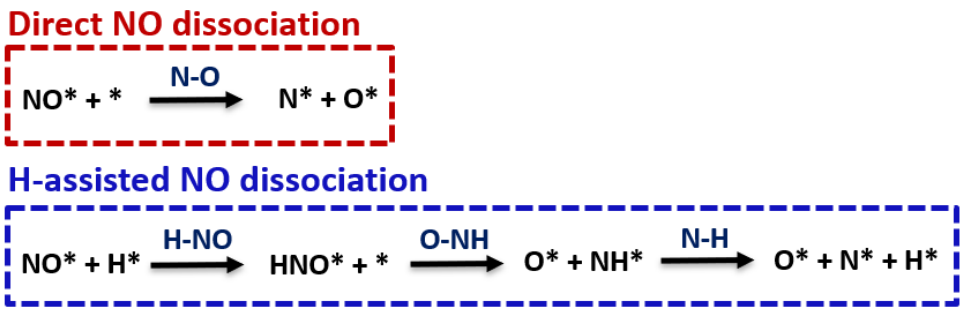

Figure 3-24. Direct NO dissociation vs. H-assisted NO dissociation mechanisms. A comparison between Figure 6B in the main text and Figure S20 indicates that the H-assisted mechanism is more favorable on both the Pd(111) surface and at the Pd NP–CeO_2(111) interface with oxygen vacancies.

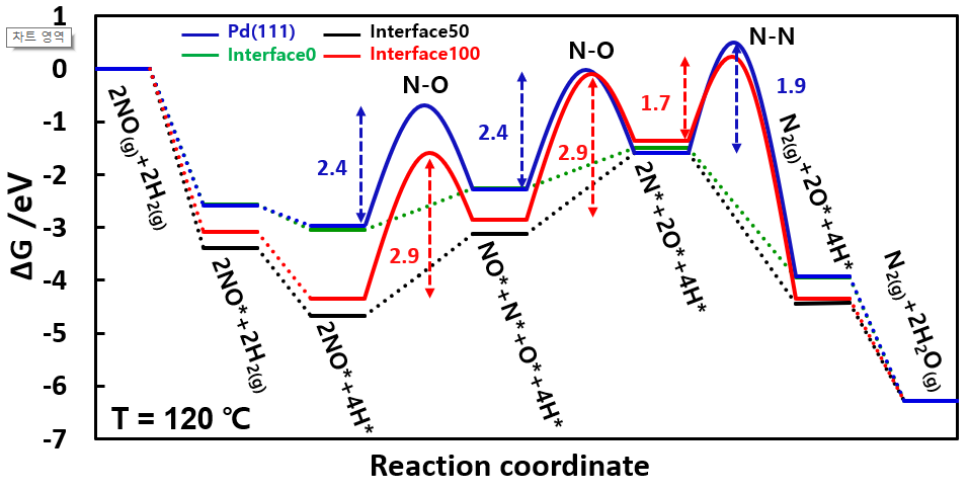

Figure 3-25. Gibbs free energy diagram for NO reduction to N_2 via direct NO dissociation.

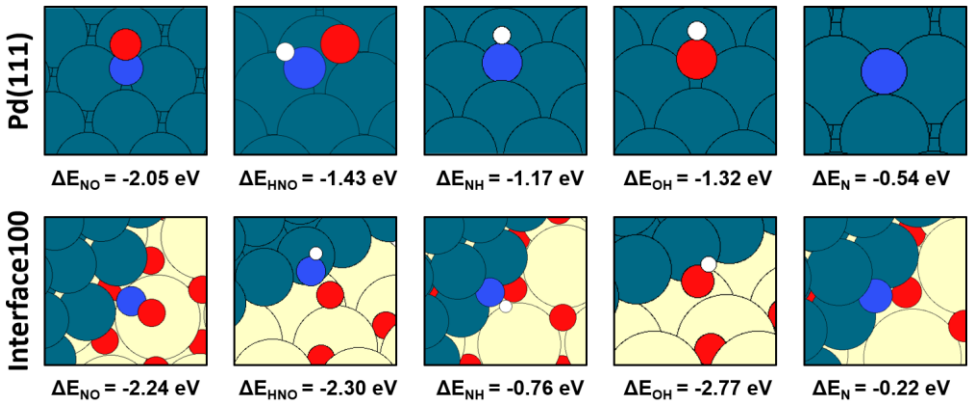

Figure 3-26. The calculated adsorption configurations and energies for all the reaction intermediates involved in NO reduction to N_2 on Pd(111) and Interface100. All adsorption energies were referenced to gas-phase NO, H_2, and O_2.

Chapter 4. Developing light hydrocarbon abatement catalyst for gasoline system

4.1. Introduction

Due to concerns about environmental pollution emitted from automobiles, governments have been strengthening their emission regulations for several decades [1]. One of the upcoming regulations is the combined regulation of non-methane organic gas and NOx (NMOG + NOx) [119]. Therefore, reducing NO emissions and decreasing unburned hydrocarbon (HC) species in exhaust gas is crucial. In particular, it is key to reduce the emission during the cold-start period before the catalytic converters reach a sufficient temperature. Several studies utilize zeolite-based catalysts as an HC trap to alleviate cold-start HC emissions [5]. However, the zeolite-based HC traps have several drawbacks that it is difficult to apply directly without any modification for gasoline application [5].

Because of the easily adsorbable larger molecular weight molecules, the lower aging temperatures, and the lean operating conditions, the hydrocarbon trap has been widely investigated and successfully applied in diesel applications [5]. Beta zeolite and ZSM-5 are the most effective for trapping C_6 and higher hydrocarbons. However, zeolite-based hydrocarbon

traps may not be the best option for gasoline applications. The trap is placed upstream of the TWC and right after the engine. In this condition, zeolites are not stable enough to withstand the high temperatures of gasoline engines [59]. Also, the low oxygen concentration in gasoline vehicles may be partly responsible for the poor conversion of the released hydrocarbon and lower-emitting temperature than the light-off temperature of TWC [5]. Therefore, there is a need for a new system that can compensate for the shortcomings of the current zeolite-based hydrocarbon trap and work well in a gasoline environment. To this end, this chapter investigated the Pd/CeO_2 catalyst as a potential hydrocarbon mitigation catalyst for gasoline cold-start applications.

When combined NMOG+NOx regulation is applied, it is crucial to reduce NOx and hydrocarbon together, especially during the cold-start period. Studying the interaction with NOx when developing a hydrocarbon trap in this context is necessary. Here, the effect of NOx when using Pd/CeO_2 as a hydrocarbon trap was investigated. Recently, it has been reported that NOx emitted in the cold-start period in a gasoline vehicle can be successfully abated using Pd/Ce-based catalysts [59]. Oxygen vacancy of the catalysts played an essential role in NOx storage. To analyze and compare the interaction between the abatement of NOx and hydrocarbon, we selected propene (C_3H_6) as a model hydrocarbon compound and compared the abatement ability of each substance of Pd/CeO_2 at low temperatures.

In this chapter, the applicability of Pd/CeO_2 for gasoline HC trap is

carefully reviewed as part of designing the low-temperature catalytic converter for gasoline engine vehicles. Based on the experimental results, a possible storage mechanism is proposed. In addition, it also investigated how the use of Ce–Zr mixed oxide (Ce–Zr–O) affects the thermal stability of the catalyst to develop an advanced catalytic converter with better durability. Since the trapping catalyst is mainly located right after the engine, stability against high temperatures is essential.

4.2. Experimental

4.2.1. Catalyst preparation

The catalysts were prepared using the conventional incipient wetness impregnation method. Commercial CeO_2, $Ce_{0.4}Zr_{0.5}La_{0.05}Y_{0.05}O_2$ (S1), $Ce_{0.31}Zr_{0.45}La_{0.06}Y_{0.12}Nd_{0.06}O_2$ (S2), $Ce_{0.21}Zr_{0.72}La_{0.02}Nd_{0.05}O_2$ (S3), $Ce_{0.4}Zr_{0.55}Pr_{0.05}O_2$ (S4) were obtained from Solvay. γ-Al_2O_3 (Sasol) was obtained from Sasol. All support powders were dried in an oven at 105 °C for 3 h before impregnating metal precursors. The desired amounts of Pd, Pt, and Rh were loaded onto the supports by impregnating aqueous solutions of $Pd(NO_3)_2 \cdot 2H_2O$ (Merck), $Pt(NH_3)_4(NO_3)_2$ (Alfa Aesar), or $Rh(NO_3)_3$ (10 wt.% Rh in solution, Merck) as the metal precursor, respectively. The resulting powder was dried at 105 °C overnight and then calcined at 800 °C under a 100 mL/min gas flow of 15 vol.% O_2 with an N_2 balance for 2 h.

The prepared catalysts were named as Pt(1)Pd(1)/CeO_2, Pt(2)/CeO_2, Rh(2)/CeO_2, CeO_2, Pd(2)/Al_2O_3, Pt(2)/Al_2O_3, Rh(2)/Al_2O_3, Pd(2)/TiO_2, Pd(1)/CeO_2, Pd(2)/CeO_2, Pd(3)/CeO_2, Pd(4)/CeO_2, Pd(5)/CeO_2, Pd(2)/S1, Pd(2)/S2, Pd(2)/S3, Pd(2)/S4. The number in the parentheses shows the metal loading.

4.2.2. Catalyst characterization

N_2 physisorption was conducted to measure the Brunauer–Emmett–Teller (BET) surface areas and pore volumes using a BELSORP-mini II (MicrotracBEL, Japan) instrument. The samples were pretreated at 150 °C for 4 h under a vacuum. *In situ* DRIFTS spectra were collected using an FT-IR spectrometer (Nicolet 6700, Thermo Fisher Scientific) equipped with a diffuse reflectance cell (Praying Mantis, Harrick Scientific Products Inc.) and an MCT detector. Pd(2)/CeO_2 powder (130 mg) was loaded onto the DRIFTS cell. Pretreatment was conducted under O_2 treatment for 30 min at 400 °C. After pretreatment, the samples were purged with N_2 for 30 min and then cooled. The background spectrum was obtained at 20 °C after each pretreatment. Pulsed CO chemisorption was conducted using BELCAT II. Typically, 0.05 g of the sample was heated at 400 °C under a He gas flow and cooled to 120 °C under He. The sample was then reduced using a 5 vol.% H_2/Ar mixture at 120 °C for 30 min, then purging with a He flow and cooling to -78 °C with a liquid nitrogen spray. The CO pulse was dosed in a He stream until the catalyst was saturated with CO. Pulsed CO

chemisorption was performed at -78 °C to suppress CO adsorption on the CeO_2 surface and avoid overestimating the Pd dispersion [86]. The stoichiometric factor (the ratio between Pd atoms to chemisorbed CO molecules) was assumed to be 1. The number of Pd atoms exposed on the surface is supposed to be the same as the number of chemisorbed CO molecules. X-ray diffraction patterns were recorded on a powder X-ray diffractometer (Smartlab, Rigaku) with a current of 30 mA and voltage of 40 kV in the 2θ range from 10° to 90°.

4.2.3. Performance evaluation

The catalytic activities and NO storage abilities of the catalysts were evaluated using a continuous-flow quartz tubular reactor. First, 0.1 g of catalyst (80–100 mesh) was loaded in the reactor with 0.1 g of α-Al_2O_3 (80–100 mesh) to dissipate the heat produced during the experiments. The total flow rate was maintained at 200 mL/min (gas hourly space velocity, GHSV = 120,000 mL/h·g_{cat}) under atmospheric pressure, with various gas compositions (NO, H_2O, CO_2, O_2, CO, H_2, and C_3H_6) to simulate gasoline exhaust. The λ values, defined as $\lambda = ([O_2] + 0.5[CO] + 0.5[H_2O] + [CO_2] + 0.5[NO])/([CO] + 0.5[H_2] + 4.5[C_3H_6] + 0.5[H_2O] + [CO_2])$, was also controlled. Typically, 100 ppm NO, 5 vol.% H_2O, 5 vol.% CO_2, 6,000 ppm CO, 2,000 ppm H_2, 1,000 ppm C_3H_6, and N_2 (as the balance) were introduced, while the O_2 concentration was varied from 0.5 to 1.35 vol.%; this changed the λ from 0.95 to 1.05. The concentrations of the outlet gas

components are analyzed using an online FT-IR spectrometer (Nicolet iS50, Thermo Fisher Scientific) with a mercury cadmium telluride (MCT) detector.

The samples were pre-treated at 700 °C with a ramping rate of 10 °C/min for 30 min under 5 vol.% O_2, 5 vol.% H_2O, and 5 vol.% CO_2 (balanced with N_2). After that, they were cooled down to 120 °C and maintained. The gas composition of 5 vol.% H_2O, 5 vol.% CO_2, 6,000 ppm CO, 2,000 ppm H_2, and 1,000 ppm C_3H_6, with and without 100 ppm NO and N_2 as a balance was introduced to evaluate the C_3H_6 abatement ability of catalyst.

4.3. Results and discussion

Figure 4-1 shows the result of catalyst screening on the C_3H_6 abatement performance of various CeO_2-supported and Al_2O_3-supported catalysts. Among them, Pd(2)/CeO_2 showed the best performance and was adopted as the standard catalyst in this study. This result is probably due to the strong interaction of Pd and CeO_2 [120]. The Pd−CeO_2 interaction is often very important in many catalytic reactions. For example, the Pd−CeO_2 interaction was essential in NOx storage in our previous research [22, 59]. NOx storage performance was not shown when only one of Pd or CeO_2 was present. Similar results were obtained in the C_3H_6 abatement activity test,

indicating that the interaction between Pd and CeO_2 is important. The catalytic abatement activity was higher at λ of 1.05 with higher oxygen concentration than at λ of 0.95 with low oxygen concentration in Pd/CeO_2. This phenomenon indirectly shows that oxygen involves itself in the C_3H_6 abatement ability of Pd/CeO_2.

Next, several abatement activity tests were performed to see if Pd/CeO_2 shows the abatement activity of HCs other than C_3H_6 (Figure 4-2). In case of the λ value of each experiment, the hydrocarbon concentration was adjusted according to the slightly lean condition. There was little abatement effect for iso-pentane, while toluene had some abatement effect. There was no abatement activity at all in the case of C_3H_8 and CH_4. From this point of view, it can be seen that functional groups such as double bonds are very important for surface adsorption.

Next, the effect of Pd loading was investigated (Figure 4-3). Up to 4 wt.%, the abatement activity increased as Pd loading increased, but 5wt.% showed the same result as 4 wt.%. The amount of adsorption for the total number of Pd decreased with loading, but the amount of adsorption for Pd exposed on the surface increased with loading. It can be inferred that larger-size Pd nanoparticles exhibit better C_3H_6 abatement performance. Further analysis is required as this may result from maintaining a high surface area due to stronger metal-supporter interaction with higher loading [43].

In order to find out about the relationship between NO abatement and C_3H_6 abatement, a few activity tests were conducted according to the presence or absence of each gas component (Figure 4-4). When NO is adsorbed in advance or introduced together with C_3H_6, the C_3H_6 abatement ability is significantly reduced. However, in the opposite case, the decrease was relatively small. This decrease is because NO can preferentially bind to oxygen vacancy sites [22]. However, this phenomenon may vary depending on the oxygen concentration. In fuel-lean environments such as diesel combustion, the oxygen concentration is excessive, and in this case, the presence of C_3H_6 has an enhancing effect on the NO abatement ability (Figure 4-5A). Even in this case, the presence of NO suppressed the C_3H_6 abatement ability of Pd/CeO_2 (Figure 4-5B). It can be seen that the C_3H_6 abatement ability was significantly decreased when NO was present, but the abatement ability was activated again when NO was turned off (Figure 4-6).

It can also be confirmed from the results of *in-situ* DRIFT experiments that oxygen greatly affects the C_3H_6 reduction ability (Figure 4-7). At around 120°C, C_3H_6 abatement includes the ability to adsorb on the Pd/CeO_2 surface and oxidize it on the surface. In Figure 4-7A, only a small amount of C_3H_6 had adsorbed before oxygen was turned on. It can be seen that oxidation occurred on the catalyst surface from the carbonate peak (1554 cm^{-1}, 1423 cm^{-1}), which increases when oxygen is turned on, and the adsorption amount also increases from the adsorption peak observed in the

2700-3000 cm^{-1} wavenumber region (Figure 4-7B). However, it can be confirmed that the growth of the carbonate peak was not observed in the 90 °C test result because oxidation did not occur (Figure 4-7C). However, even at 90 °C, it can be seen that the C_3H_6 adsorption capacity was increased when oxygen was turned on (Figure 4-7D).

From another DRIFT experiment result, the interaction between NO and C_3H_6 can also be confirmed (Figures 4-5 and 4-8). Based on these results, the following C_3H_6 abatement mechanism over Pd/CeO_2 can be suggested (Figure 4-9). Without NO, C_3H_6 can be combined with the surface lattice oxygen and be stored or oxidized on the catalyst surface. At this time, the oxygen concentration in the atmosphere plays an important role in replenishing the lattice oxygen. However, when NO is present, C_3H_6 can no longer be adsorbed because NO is stored in oxygen vacancy. However, if NO is removed, C_3H_6 can be reduced again because the adsorption and desorption of NO are under dynamic equilibrium.

Lastly, the NO abatement ability and C_3H_6 abatement ability of Pd/CeO_2 and Pd/Ce–Zr–O were evaluated after reductive aging at 800 and 900 °C, as the exhaust temperature of gasoline vehicles can rise above 800 °C in the presence of reducing gases (Figures 4-10 and 4-11). From the XRD data, it can be seen that all the samples well maintained the crystalline fluorite structure (Figure 4-12). Due to the size difference between the Ce atom and the Zr atom, the higher the Zr content, the smaller the lattice

parameter, resulting in a more significant peak shift in the XRD pattern [57]. Pd/S1 maintained the highest activity ratio compared to the initial activity even after reductive aging (Figure 4-10A). Ce–Zr–O-based catalyst also showed better C_3H_6 oxidation ability than Pd/CeO_2 without the Zr component. This oxidation ability is attributed to improved oxygen mobility [57]. In the case of Ce–Zr–O mixed oxide, the ability to diffuse out lattice oxygen is better than pure CeO_2.

The NO storage ability of Pd/CeO_2 was severely degraded after reductive aging at high temperatures; this can be attributed to CeO_2 sintering, as it decreases the Pd-NP–CeO_2 interfacial area (Figure 4-11). Previous research demonstrated that the NO is stored near the oxygen vacancies of the CeO_2 surface interacting with Pd NP. However, after the reductive aging at 800 and 900 °C, the NO storage ability of Pd/CeO_2 was severely diminished by the reduction of NO storage sites (Pd–CeO_2 interfaces). Because of the structural distortion during the reduction of CeO_2 bulk, the surface area of CeO_2 was significantly decreased after reduction at 800 and 900 °C (Figure 4-11C). Moreover, the strong metal-support interaction (SMSI) would also decrease the Pd–CeO_2 interfaces by CeO_2 covering Pd particles [121-124]. To overcome the deactivation occurring by the reductive aging, we adopted Ce–Zr mixed oxide (Ce–Zr–O) as support. As previously mentioned, the thermal stability of Ce–Zr–O is much superior to pure CeO_2, as the intercalation of Zr, which has a smaller atomic size than

Ce, into CeO_2 lattice improves the oxygen mobility and structural stability of Ce–Zr–O [125-127]. As a result, Ce–Zr–O only negligibly agglomerates even after reductive aging at 900 °C. This enables the reduction of bulk oxygen in the Ce–Zr–O without the collapse of the bulk structure. Consequently, even after the reductive aging at 800 and 900 °C, Pd/Ce–Zr–O showed minor changes in the crystalline structure and surface area, resulting in only a slightly reduced NO storage efficiency. For this reason, Ce–Zr–O-type materials should be used in practical applications rather than pure CeO_2.

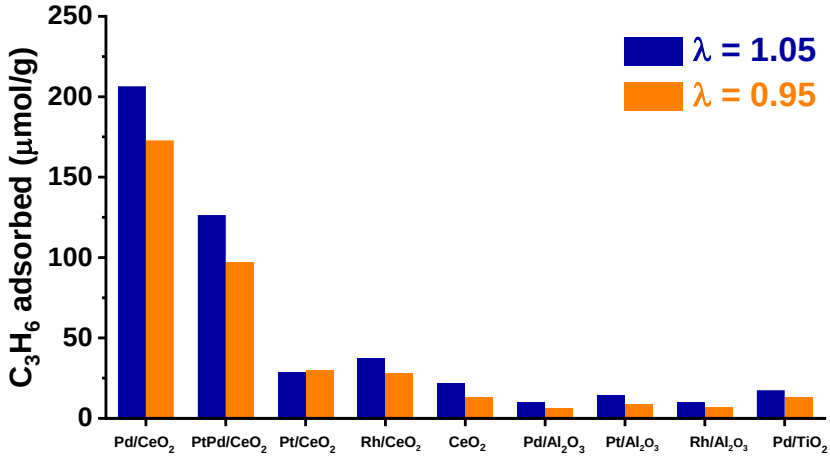

Figure 4-1. Amount of C_3H_6 abatement for first 10 min over Pd/CeO_2, $PtPd/CeO_2$, Pt/CeO_2, Rh/CeO_2, CeO_2, Pd/Al_2O_3, Pt/Al_2O_3, Rh/Al_2O_3, Pd/TiO_2 catalysts. The amount of total C_3H_6 injected was 614 μmol/g.

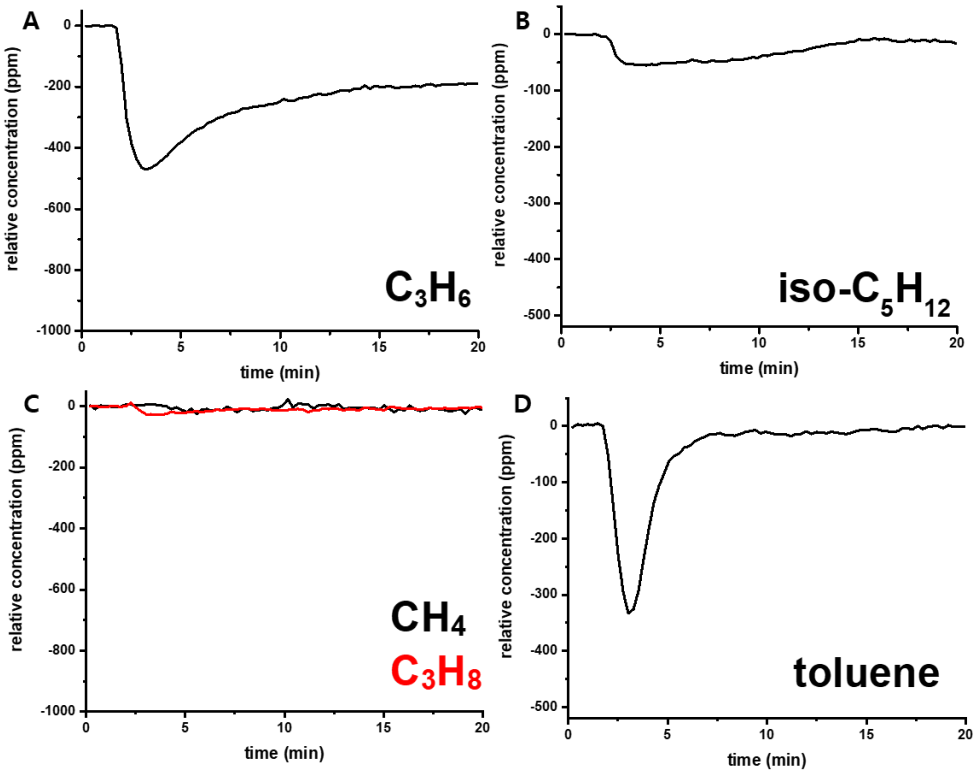

Figure 4-2. Abatement test of various hydrocarbons over Pd(2)/CeO_2 catalyst. 5% H_2O, 5% CO_2, 1.35% O_2, 6000 ppm CO, 2000 ppm H_2 were commonly injected. (A) 1000 ppm C_3H_6 (B) 520 ppm iso-C_5H_{12} (C) 1000 ppm CH_4 or 830 ppm C_3H_8 (D) 500 ppm toluene was injected.

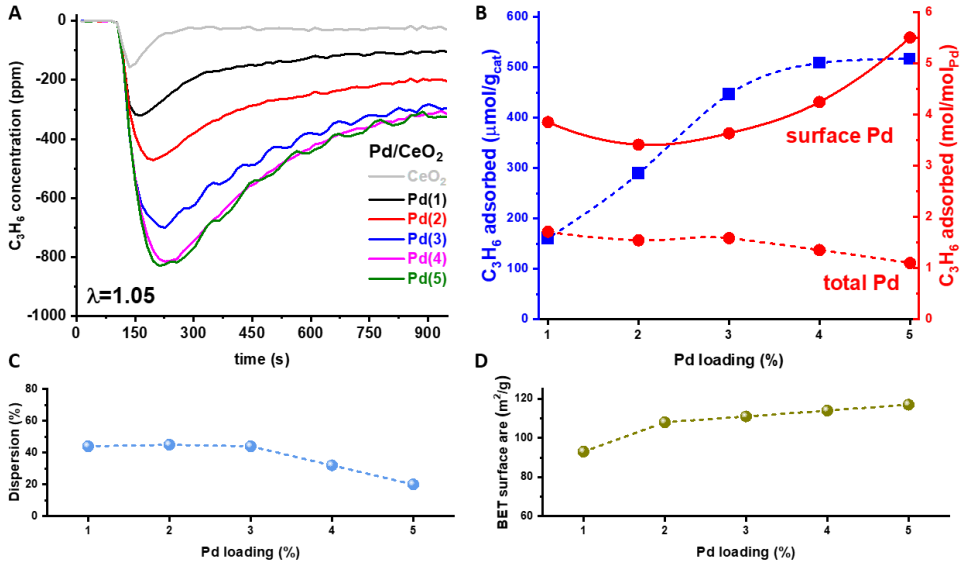

Figure 4-3. (A) Cold-start C_3H_6 abatement activities of Pd/CeO_2 with various loadings. (B) Amount of C_3H_6 abatement according to the amount of catalyst, the amount of exposed Pd, and the amount of total Pd. (C) Pd dispersion of Pd/CeO_2 catalysts obtained at -78 °C. (D) The BET surface area of Pd/CeO_2 samples.

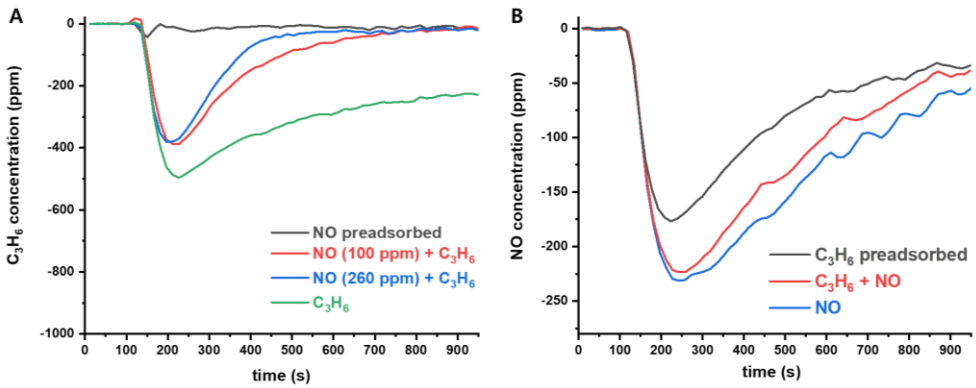

Figure 4-4. (A) C_3H_6 abatement activities of Pd/CeO_2 with and without NO or after pre-adsorption of NO. (B) NO abatement activities of Pd/CeO_2 with and without C_3H_6 or after pre-adsorption of C_3H_6.

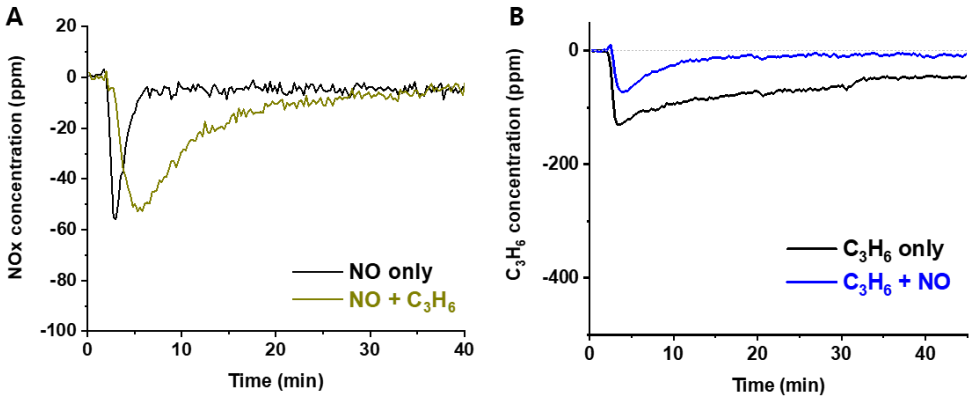

Figure 4-5. (A) NO abatement activities of Pd/CeO_2 with and without C_3H_6 under fuel-lean condition with excess oxygen. (B) C_3H_6 abatement activities of Pd/CeO_2 with and without NO under fuel-lean condition with excess oxygen.

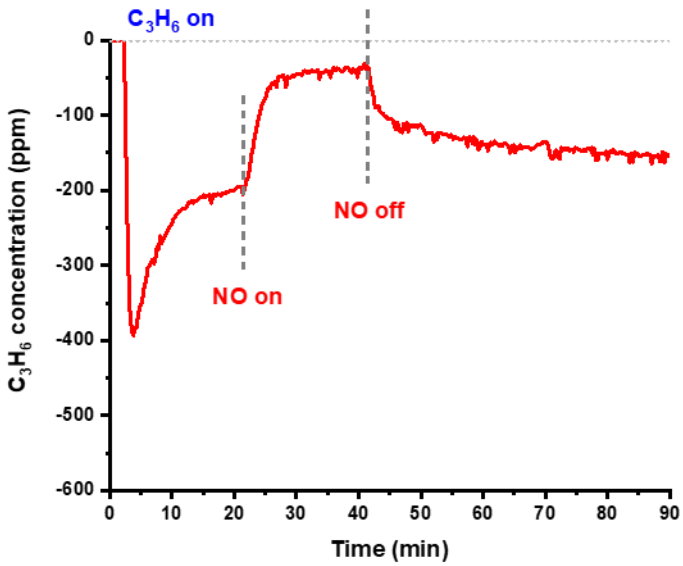

Figure 4-6. C_3H_6 abatement activities of Pd(2)/CeO_2 upon NO addition and removal of NO in the feed stream.

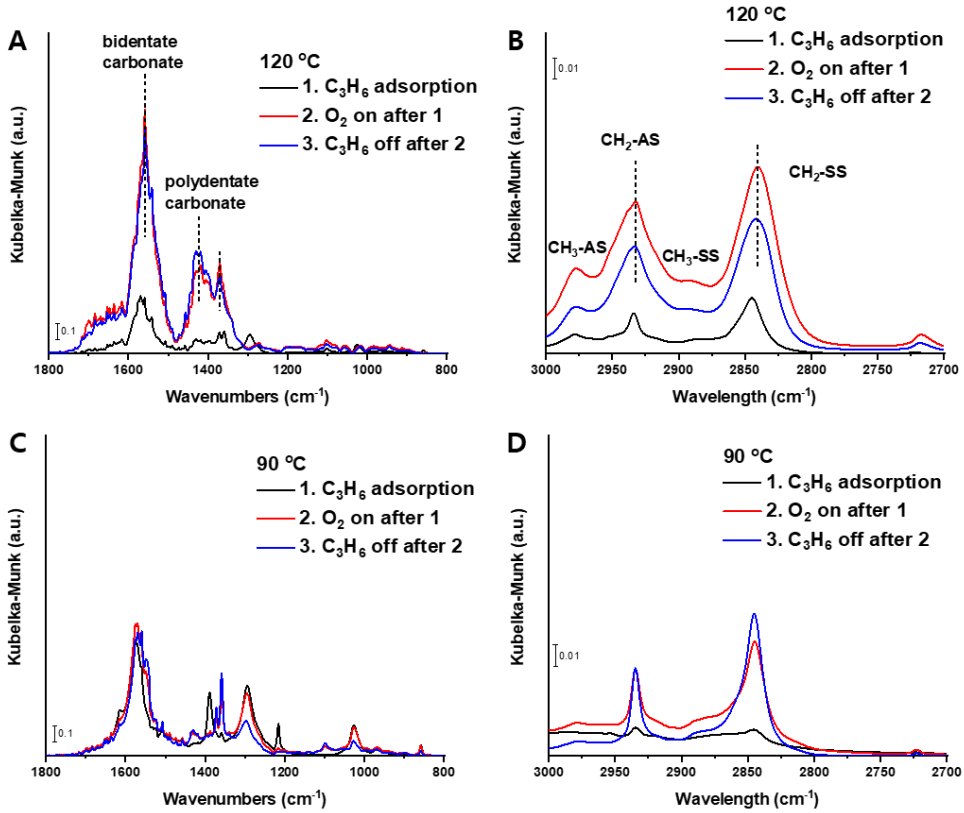

Figure 4-7. *In-situ* C_3H_6-diffuse reflectance infrared Fourier-transform spectroscopy spectra of Pd(2)/CeO_2 after C_3H_6 adsorption with and without O_2. (A) wavenumber 1800 – 800 cm^{-1} at 120 °C (B) wavenumber 3000 – 2700 cm^{-1} at 120 °C (C) wavenumber 1800 – 800 cm^{-1} at 90 °C (D) wavenumber 3000 – 2700 cm^{-1} at 90 °C

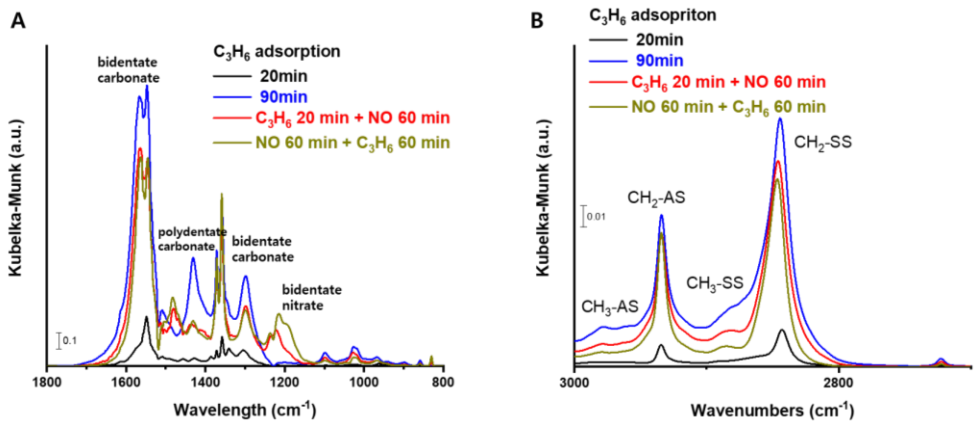

Figure 4-8. *In-situ* DRIFT spectra of Pd(2)/CeO_2. Spectra were collected after 20 min, 90 min adsorption of C_3H_6, 20 min adsorption of C_3H_6 followed by 60 min NO adsorption, and 60min NO adsorption followed by 60 min C_3H_6 adsorption. (A) wave number 1800 – 800 cm^{-1} (B) wave number 3000 – 2700 cm^{-1}

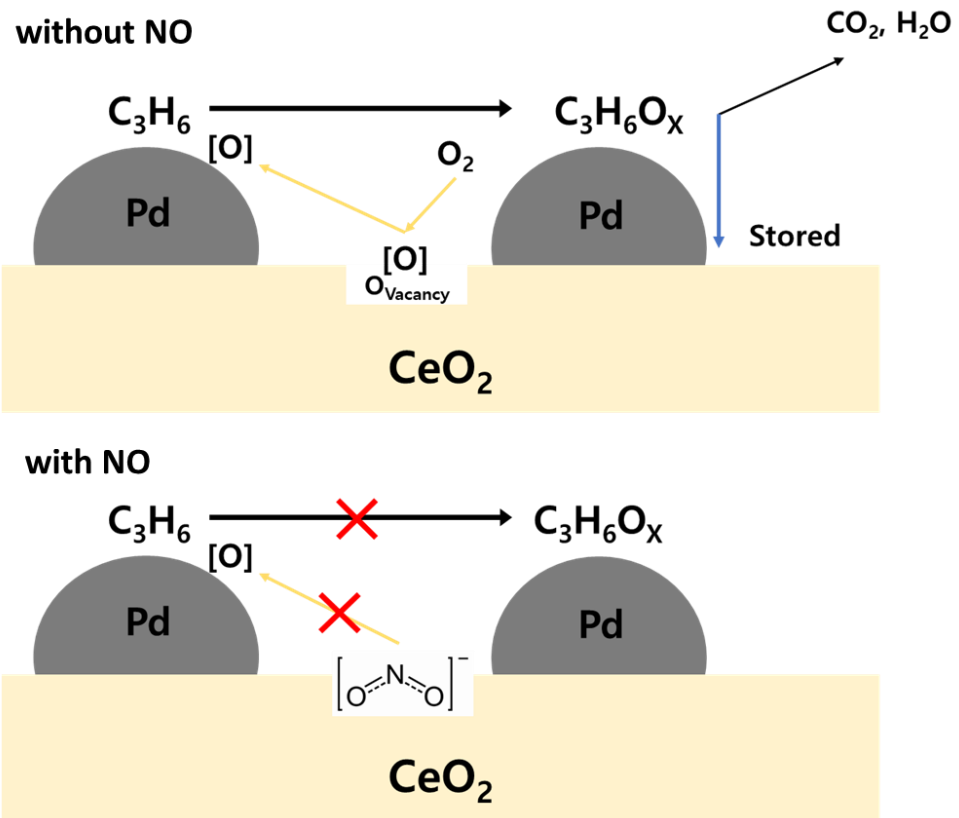

Figure 4-9. Schematic illustration of C_3H_6 adsorption on Pd/CeO_2 with and without NO.

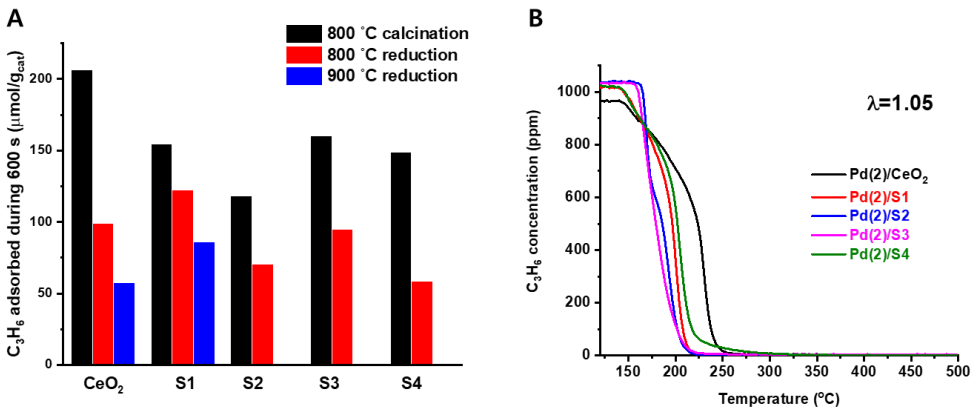

Figure 4-10. (A) Amount of C_3H_6 abatement activities of Pd(2)/CeO_2, Pd(2)/S1, Pd(2)/S2, Pd(2)/S3, Pd(2)/S4 after 800 °C calcination, 800 °C reduction, 900 °C reduction treatment. (B) Light-off curve of C_3H_6 oxidation over Pd(2)/CeO_2, Pd(2)/S1, Pd(2)/S2, Pd(2)/S3, Pd(2)/S4.

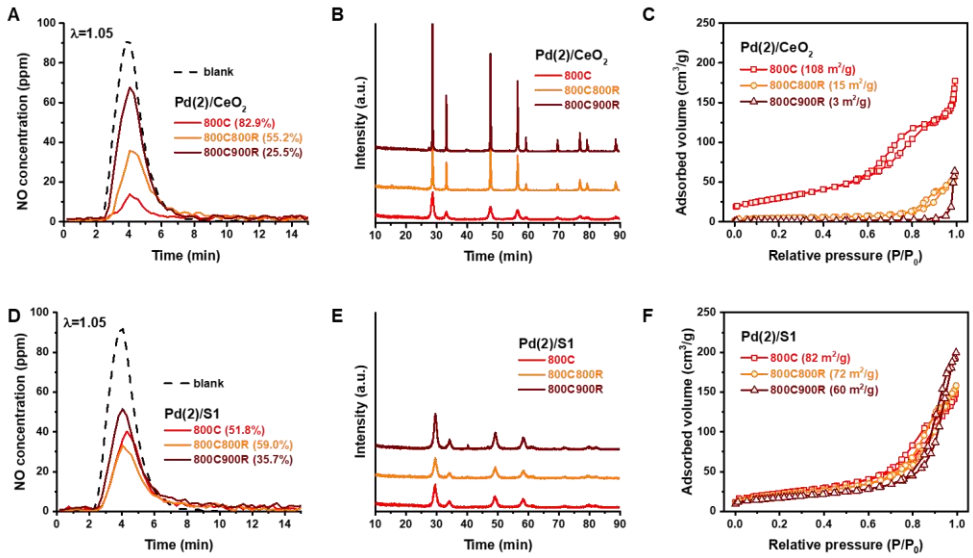

Figure 4-11. (A) NO storage ability, (B) XRD patterns, and (C) N_2 adsorption-desorption profiles with BET surface areas of Pd/CeO_2 before and after the reductive aging at 800 and 900 °C. (D) NO storage ability, (E) XRD patterns, and (F) N_2 adsorption-desorption profiles with BET surface areas of Pd/S1 before and after the reductive aging at 800 and 900 °C. NO flowed for 100 sec at 120 °C.

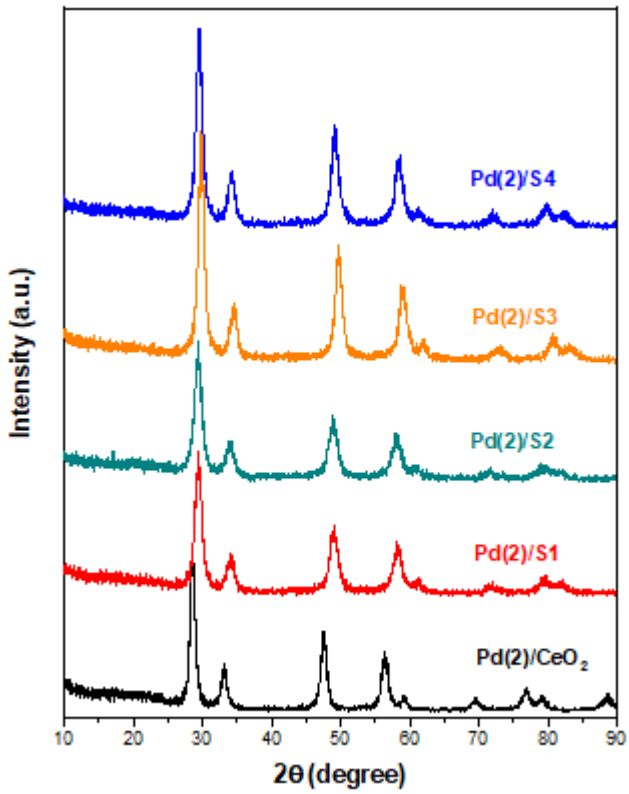

Figure 4-12. XRD patterns of Pd/CeO2, Pd/S1, Pd/S2, Pd/S3 and Pd/S4.

Chapter 5. Summary and Conclusions

Pd/CeO_2 was investigated to evaluate the possibility of low-temperature NOx and C_3H_6 abatement application under various environments.

The promoting effect of CO on the NOx adsorption ability of Pd/CeO_2 was investigated. Furthermore, the study compared the adsorption performances of CeO_2, Pd/CeO_2, and Pd/Al_2O_3 and determined that the promoting effect of CO was observed only for Pd/CeO_2. This promoting effect was attributed to the unique low-temperature CO oxidation ability of Pd/CeO_2. When the Pd/CeO_2 surface was reduced by reductive pretreatment, NOx adsorption was promoted. In this respect, NOx adsorption could be facilitated by CO oxidation. When CO oxidation occurred via the M–vK mechanism at low temperatures, oxygen vacancies were generated on the catalyst surface, and NOx could be further adsorbed. The promotion of NOx adsorption by CO oxidation can be extended to other ceria-based PNA systems.

In the following study, a strategy geared toward achieving zero NO emissions from gasoline vehicles was devised through the joint implementation of catalyst and engine functions. The combined application of adsorptive and catalytic functionalities of Pd-incorporated CeO_2 catalyst enabled zero NO emissions over the entire temperature range of gasoline

vehicle operation. To the best knowledge, this is the first attempt to eliminate NO emissions during the cold-start period of a gasoline vehicle by harmonizing the adsorption and catalytic converting functions through engine control. However, further studies to increase the number of active Pd NP–CeO_2 interface sites, improve the thermal stability of the CeO_2 domain in a reducing atmosphere, and optimize the synchronization of catalytic function and engine control will be needed to maximize the commercial advantage of this strategy.

Finally, the possibility of applying Pd/CeO_2 to store C_3H_6 at low temperatures is reviewed to address future regulations on unburned hydrocarbons. The relationship between NO adsorption and C_3H_6 adsorption over Pd/CeO_2 surface was also investigated. A possible mechanism for the propene adsorption on Pd/CeO_2 surface was suggested based on the experimental and characterization data. In addition, Ce–Zr–O was successfully introduced to improve thermal stability and overcome deactivation by reductive aging at high temperatures.

Bibliography

[1] C.H. Kim, H.S. Han, Emiss. Control Sci. Technol., 4 (2018) 1-3.

[2] A.K. Datye, M. Votsmeier, Nat. Mater., 20 (2021) 1049-1059.

[3] C.K. Lambert, Nat. Catal., 2 (2019) 554-557.

[4] S. Dey, N.S. Mehta, Resources, Environment and Sustainability, 2 (2020) 100006.

[5] R.J. Farrauto, M. Deeba, S. Alerasool, Nat. Catal., 2 (2019) 603-613.

[6] H.-Y. Chen, S. Mulla, E. Weigert, K. Camm, T. Ballinger, J. Cox, P. Blakeman, SAE Int. J. Fuels Lubr., 6 (2013) 372-381.

[7] R.J. Farrauto, M. Deeba, S. Alerasool, Nat. Catal., 2 (2019) 603-613.

[8] G. Beulertz, M. Votsmeier, R. Moos, Appl. Catal. B Environ., 165 (2015) 369-377.

[9] T. Wang, Y. Zhang, J. Zhang, G. Shu, Z. Peng, Appl. Therm. Eng., 53 (2013) 414-419.

[10] H. Wei, T. Zhu, G. Shu, L. Tan, Y. Wang, Appl. Energy, 99 (2012) 534-544.

[11] A.G. Des Buttes, B. Jeanneret, A. Kéromnès, L. Le Moyne, S. Pélissier, Appl. Energy, 266 (2020) 114866.

[12] J.A. Cole, US5656244A, Energy and Environmental Research Corp (1997).

[13] Y. Ryou, J. Lee, H. Lee, C.H. Kim, D.H. Kim, Catal. Today, 307 (2018) 93-101.

[14] Y.Y. Ji, S.L. Bai, M. Crocker, Appl. Catal. B Environ., 170 (2015) 283-292.

[15] Y. Ryou, J. Lee, S.J. Cho, H. Lee, C.H. Kim, D.H. Kim, Appl. Catal. B Environ., 212 (2017) 140-149.

[16] H.Y. Chen, J.E. Collier, D.X. Liu, L. Mantarosie, D. Duran-Martin, V. Novak, R.R. Rajaram, D. Thompsett, Catal. Lett., 146 (2016) 1706-1711.

[17] İ.A. Reşitoğlu, K. Altinişik, A. Keskin, Clean Technol. Environ. Policy, 17 (2015) 15-27.

[18] Y. Ryou, J. Lee, Y. Kim, S. Hwang, H. Lee, C.H. Kim, D.H. Kim, Appl. Catal. A Gen., 569 (2019) 28-34.

[19] J. Lee, J.R. Theis, E.A. Kyriakidou, Appl. Catal. B Environ., 243 (2019) 397-414.

[20] E. Jang, L. Choi, J. Kim, Y. Jeong, H. Baik, C.Y. Kang, C.H. Kim, K.Y. Lee, J. Choi, Appl. Catal. B Environ., 287 (2021) 119951.

[21] F. Migliardini, F. Iucolano, D. Caputo, P. Corbo, J. Chem., 2015 (2015) 269694.

[22] S. Hwang, Y. Kim, J. Lee, E. Lee, H. Lee, C. Jeong, C.H. Kim, D.H. Kim, Catal. Today, 384-386 (2022) 88-96.

[23] A.K. Datye, M. Votsmeier, Nat. Mater., (2020).

[24] F. Gao, J. Szanyi, Appl. Catal. A Gen., 560 (2018) 185-194.

[25] S.D. Yim, S.J. Kim, J.H. Baik, I.S. Nam, Y.S. Mok, J.H. Lee, B.K. Cho, S.H. Oh, Ind. Eng. Chem. Res., 43 (2004) 4856-4863.

[26] F. Gao, D. Mei, Y. Wang, J. Szanyi, C.H. Peden, J. Am. Chem. Soc., 139 (2017) 4935-4942.

[27] J.A. Cole, U.S. Patent 5656,244, Energy and Environmental Research Corporation (1997).

[28] Y. Murata, T. Morita, K. Wada, H. Ohno, SAE Int. J. Fuels Lubr., 8 (2015) 454-459.

[29] Y.T. Gu, W.S. Epling, Appl. Catal. A Gen., 570 (2019) 1-14.

[30] A. Gupta, S.B. Kang, M.P. Harold, Catal. Today, 360 (2021) 411-425.

[31] M. Ambast, K. Karinshak, B.M.M. Rahman, L.C. Grabow, M.P. Harold, Appl. Catal. B Environ., 269 (2020) 118802.

[32] Y. Kim, S. Hwang, J. Lee, Y. Ryou, H. Lee, C.H. Kim, D.H. Kim, Emission Control Science and Technology, 5 (2019) 172-182.

[33] K. Khivantsev, F. Gao, L. Kovarik, Y. Wang, J. Szanyi, J. Phys. Chem. C, 122 (2018) 10820-10827.

[34] O. Mihai, L. Trandafilovic, T. Wentworth, F.F. Torres, L. Olsson, Top. Catal., 61 (2018) 2007-2020.

[35] A. Vu, J.Y. Luo, J.H. Li, W.S. Epling, Catal. Lett., 147 (2017) 745-750.

[36] K. Khivantsev, N.R. Jaegers, L. Kovarik, S. Prodinger, M.A. Derewinski, Y. Wang, F. Gao, J. Szanyi, Appl. Catal. A Gen., 569 (2019) 141-148.

[37] K. Khivantsev, N.R. Jaegers, L. Kovarik, J.C. Hanson, F.F. Tao, Y. Tang, X.

Zhang, I.Z. Koleva, H.A. Aleksandrov, G.N. Vayssilov, Y. Wang, F. Gao, J. Szanyi, Angew. Chem. Int. Ed., 57 (2018) 16672-16677.

[38] J.R. Theis, C. Lambert, SAE Int. J. Engines, 10 (2017) 1627-1637.

[39] J.R. Theis, C.K. Lambert, Emiss. Control Sci. Technol., 5 (2019) 215-244.

[40] A. Kvasničková, P. Kočí, Y. Ji, M. Crocker, Catal. Lett., 150 (2020) 3223-3233.

[41] A.B. Sifontes, B. Gutierrez, A. Monaco, A. Yanez, Y. Diaz, F.J. Mendez, L. Llovera, E. Canizales, J.L. Brito, Biotechnol. Rep,, 4 (2014) 21-29.

[42] A.I.Y. Tok, F.Y.C. Boey, Z. Dong, X.L. Sun, J. Mater. Process. Technol., 190 (2007) 217-222.

[43] J. Lee, Y. Ryou, X. Chan, T.J. Kim, D.H. Kim, J. Phys. Chem. C, 120 (2016) 25870-25879.

[44] J. Lee, J. Kim, Y. Kim, S. Hwang, H. Lee, C.H. Kim, D. Kim, Appl. Catal. B Environ., 277 (2020) 119190.

[45] G.H. Wu, B.B. Chen, Z.F. Bai, Q. Zhao, Z.H. Wang, C.S. Song, X.W. Guo, C. Shi, Catal. Commun., 149 (2021) 106203.

[46] G.K. Reddy, C. Ling, T.C. Peck, H.F. Jia, RSC Adv., 7 (2017) 19645-19655.

[47] Y.Y. Ji, D.Y. Xu, S.L. Bai, U. Graham, M. Crocker, B.B. Chen, C. Shi, D. Harris, D. Scapens, J. Darab, Ind. Eng. Chem. Res., 56 (2017) 111-125.

[48] I. Nakamura, Y. Kobayashi, H. Hamada, T. Fujitani, Surf. Sci., 600 (2006) 3235-3242.

[49] M. Daté, H. Okuyama, N. Takagi, M. Nishijima, T. Aruga, Surf. Sci., 350 (1996) 79-90.

[50] H. Jeong, J. Bae, J.W. Han, H. Lee, ACS Catal., 7 (2017) 7097-7105.

[51] J.R. Ye, Y. Xia, D.G. Cheng, F.Q. Chen, X.L. Zhan, Int. J. Hydrogen Energy, 44 (2019) 17985-17994.

[52] M.G. Sanchez, J.L. Gazquez, J. Catal., 104 (1987) 120-135.

[53] Y.Y. Zhou, N.J. Lawrence, T.S. Wu, J. Liu, P. Kent, Y.L. Soo, C.L. Cheung, ChemCatChem, 6 (2014) 2937-2946.

[54] S. Alayoglu, K. An, G. Melaet, S. Chen, F. Bernardi, L.W. Wang, A.E. Lindeman, N. Musselwhite, J. Guo, Z. Liu, M.A. Marcus, G.A. Somorjai, J. Phys. Chem. C, 117 (2013) 26608-26616.

[55] A. Filtschew, D. Stranz, C. Hess, Physical Chemistry Chemical Physics, 15

(2013) 9066-9069.

[56] A. Filtschew, C. Hess, Appl. Catal. B Environ., 237 (2018) 1066-1081.

[57] A. Trovarelli, Catal. Rev. Sci. Eng., 38 (1996) 439-520.

[58] Z.L. Wu, M.J. Li, S.H. Overbury, J. Catal., 285 (2012) 61-73.

[59] J. Lee, Y. Kim, S. Hwang, G.S. Hong, E. Lee, H. Lee, C. Jeong, C.H. Kim, J.S. Yoo, D.H. Kim, Chem Catalysis, 2 (2022) 2289-2301.

[60] C. Brand, Energy Policy, 97 (2016) 1-12.

[61] A. Jenn, I.M. Azevedo, J.J. Michalek, Environ. Sci. Technol., 50 (2016) 2165-2174.

[62] J. Riesz, C. Sotiriadis, D. Ambach, S. Donovan, Appl. Energy, 180 (2016) 287-300.

[63] B.K. Sovacool, R.F. Hirsh, Energy Policy, 37 (2009) 1095-1103.

[64] A.B. Getsoian, J.R. Theis, W.A. Paxton, M.J. Lance, C.K. Lambert, Nat. Catal., 2 (2019) 614-622.

[65] H.-Y. Chen, S. Mulla, E. Weigert, K. Camm, T. Ballinger, J. Cox, P. Blakeman, SAE Int. J. Fuels Lubr., 6 (2013) 372-381.

[66] H.-Y. Chen, J.E. Collier, D. Liu, L. Mantarosie, D. Durán-Martín, V. Novák, R.R. Rajaram, D. Thompsett, Catal. Lett., 146 (2016) 1706-1711.

[67] Z. Yang, T.K. Woo, K. Hermansson, Surf. Sci., 600 (2006) 4953-4960.

[68] Y. Li, M. Kottwitz, J.L. Vincent, M.J. Enright, Z. Liu, L. Zhang, J. Huang, S.D. Senanayake, W.D. Yang, P.A. Crozier, R.G. Nuzzo, A.I. Frenkel, Nat. Commun., 12 (2021) 1-9.

[69] P.J. Naik, Y. An, S.L. Sedinkin, H. Masching, D. Freppon, E.A. Smith, V. Venditti, I.I. Slowing, ACS Catal., 11 (2021) 10553-10564.

[70] R. Kopelent, A. Tereshchenko, A. Guda, G. Smolentsev, L. Artiglia, V.L. Sushkevich, A. Bugaev, I.I. Sadykov, T. Baidya, M. Bodnarchuk, J.A. van Bokhoven, M. Nachtegaal, O.V. Safonova, ACS Catal., 11 (2021) 9435-9449.

[71] L. Li, N. Zhang, R. Wu, L. Song, G. Zhang, H. He, ACS Appl. Mater. Interfaces, 12 (2020) 10350-10358.

[72] Y. Lykhach, T. Staudt, M. Vorokhta, T. Skála, V. Johánek, K.C. Prince, V. Matolín, J. Libuda, J. Catal., 285 (2012) 6-9.

[73] G.N. Vayssilov, Y. Lykhach, A. Migani, T. Staudt, G.P. Petrova, N. Tsud, T.

Skala, A. Bruix, F. Illas, K.C. Prince, V. Matolin, K.M. Neyman, J. Libuda, Nat. Mater., 10 (2011) 310-315.

[74] J. Lee, Y. Ryou, X. Chan, T.J. Kim, D.H. Kim, J. Phys. Chem. C, 120 (2016) 25870-25879.

[75] W. Lin, A. Herzing, C. Kiely, I. Wachs, J. Phys. Chem. C, 112 (2008) 5942-5951.

[76] T.W. van Deelen, C.H. Mejía, K.P. de Jong, Nat. Catal., 2 (2019) 955-970.

[77] I. Ro, J. Resasco, P. Christopher, ACS Catal., 8 (2018) 7368-7387.

[78] V. Muravev, G. Spezzati, Y.-Q. Su, A. Parastaev, F.-K. Chiang, A. Longo, C. Escudero, N. Kosinov, E.J. Hensen, Nat. Catal., 4 (2021) 469-478.

[79] A. Bruix, J.A. Rodriguez, P.J. Ramírez, S.D. Senanayake, J. Evans, J.B. Park, D. Stacchiola, P. Liu, J. Hrbek, F. Illas, J. Am. Chem. Soc., 134 (2012) 8968-8974.

[80] A. Beck, X. Huang, L. Artiglia, M. Zabilskiy, X. Wang, P. Rzepka, D. Palagin, M.-G. Willinger, J.A. van Bokhoven, Nat. Commun., 11 (2020) 1-8.

[81] N.C. Nelson, M.-T. Nguyen, V.-A. Glezakou, R. Rousseau, J. Szanyi, Nat. Catal., 2 (2019) 916-924.

[82] Y.B. Lu, S.L. Zhou, C.T. Kuo, D. Kunwar, C. Thompson, A.S. Hoffman, A. Boubnov, S. Lin, A.K. Datye, H. Guo, A.M. Karim, ACS Catal., 11 (2021) 8701-8715.

[83] B.M. Weiss, E. Iglesia, J. Catal., 272 (2010) 74-81.

[84] Y. Nanba, M. Koyama, J. Phys. Chem. C, 123 (2019) 28114-28122.

[85] M. Todorova, K. Reuter, M. Scheffler, J. Phys. Chem. B, 108 (2004) 14477-14483.

[86] T. Tanabe, Y. Nagai, T. Hirabayashi, N. Takagi, K. Dohmae, N. Takahashi, S. Matsumoto, H. Shinjoh, J.N. Kondo, J.C. Schouten, H.H. Brongersma, Appl. Catal. A Gen., 370 (2009) 108-113.

[87] B. Hammer, L.B. Hansen, J.K. Nørskov, Phys. Rev. B: Condens. Matter, 59 (1999) 7413.

[88] P. Ghanekar, J. Kubal, Y. Cui, G. Mitchell, W.N. Delgass, F. Ribeiro, J. Greeley, Top. Catal., 63 (2020) 673-687.

[89] Z.-J. Zhao, Z. Li, Y. Cui, H. Zhu, W.F. Schneider, W.N. Delgass, F. Ribeiro, J. Greeley, J. Catal., 345 (2017) 157-169.

[90] L.M. Molina, B. Hammer, Phys. Rev. Lett., 90 (2003) 206102.

[91] Z. Duan, G. Henkelman, ACS Catal., 5 (2015) 1589-1595.

[92] L. Zhang, G. Spezzati, V. Muravev, M.A. Verheijen, B. Zijlstra, I.A.W. Filot, Y.Q. Su, M.W. Chang, E.J.M. Hensen, ACS Catal., 11 (2021) 5614-5627.

[93] Z. Savva, K.C. Petallidou, C.M. Damaskinos, G.G. Olympiou, V.N. Stathopoulos, A.M. Efstathiou, Appl. Catal. A Gen., 615 (2021) 118062.

[94] S.i. Matsumoto, Cattech, 4 (2000) 102-109.

[95] V.A.W. Hillier, P. Coombes, Hillier's fundamentals of motor vehicle technology, Nelson Thornes2004.

[96] A. Khajepour, M.S. Fallah, A. Goodarzi, Electric and hybrid vehicles: technologies, modeling and control-a mechatronic approach, John Wiley & Sons2014.

[97] S.H. Chan, Proc. Inst. Mech. Eng. D: J. Automob. Eng., 210 (1996) 273-280.

[98] S. Matsumoto, Cattech, 4 (2000) 102-109.

[99] J. Kim, Y. Kim, M.H. Wiebenga, S.H. Oh, D.H. Kim, Appl. Catal. B Environ., 251 (2019) 283-294.

[100] W. Lang, P. Laing, Y. Cheng, C. Hubbard, M.P. Harold, Appl. Catal. B Environ., 218 (2017) 430-442.

[101] A.K. Datye, M. Votsmeier, Nat. Mater., (2020) 1-11.

[102] R. Moos, M. Spörl, G. Hagen, A. Gollwitzer, M. Wedemann, G. Fischerauer, TWC: Lambda control and OBD without lambda probe-an initial approach, SAE International, 2008.

[103] U. Kiencke, L. Nielsen, Meas. Sci. Technol., 11 (2000) 1828.

[104] J. Lauber, T.-M. Guerra, M. Dambrine, Int. J. Syst. Sci., 42 (2011) 277-286.

[105] S.K. Hoekman, SAE Int. J. Fuels Lubr., 13 (2020) 79-98.

[106] L.G. Appel, J.G. Eon, M. Schmal, Catal. Lett., 56 (1998) 199-202.

[107] T. Takeguchi, S. Manabe, R. Kikuchi, K. Eguchi, T. Kanazawa, S. Matsumoto, W. Ueda, Appl. Catal. A Gen., 293 (2005) 91-96.

[108] J. Jones, H. Xiong, A.T. DeLaRiva, E.J. Peterson, H. Pham, S.R. Challa, G. Qi, S. Oh, M.H. Wiebenga, X.I. Pereira Hernandez, Y. Wang, A.K. Datye, Science, 353 (2016) 150-154.

[109] R. Alcala, A. DeLaRiva, E.J. Peterson, A. Benavidez, C.E. Garcia-Vargas, D. Jiang, X.I. Pereira-Hernandez, H.H. Brongersma, R. ter Veen, J. Stanek, J.T. Miller,

Y. Wang, A. Datye, Appl. Catal. B Environ., 284 (2021) 119722.

[110] F. Zaera, Int. Rev. Phys. Chem., 21 (2002) 433-471.

[111] H. Tiznado, S. Fuentes, F. Zaera, Langmuir, 20 (2004) 10490-10497.

[112] H. Jeong, J. Bae, J.W. Han, H. Lee, ACS Catal., 7 (2017) 7097-7105.

[113] W. Zhang, M. Pu, M. Lei, Langmuir, 36 (2020) 5891-5901.

[114] F. Zaera, ACS Catal., 7 (2017) 4947-4967.

[115] W. Karim, C. Spreafico, A. Kleibert, J. Gobrecht, J. VandeVondele, Y. Ekinci, J.A. van Bokhoven, Nature, 541 (2017) 68-71.

[116] M. Xiong, Z. Gao, Y. Qin, ACS Catal., 11 (2021) 3159-3172.

[117] A. Ruiz Puigdollers, P. Schlexer, S. Tosoni, G. Pacchioni, ACS Catal., 7 (2017) 6493-6513.

[118] N.M. Briggs, L. Barrett, E.C. Wegener, L.V. Herrera, L.A. Gomez, J.T. Miller, S.P. Crossley, Nat. Commun., 9 (2018) 1-7.

[119] D. Robertson, C. Chadwell, T. Alger, J. Zuehl, R. Gukelberger, B. Denton, I. Smith, SAE Int. J. Engines, 10 (2017) 898-907.

[120] S. Hinokuma, H. Fujii, M. Okamoto, K. Ikeue, M. Machida, Chem. Mater., 22 (2010) 6183-6190.

[121] S. Bernal, F.J. Botana, J.J. Calvino, G.A. Cifredo, J.A. Pe´rez-Omil, J.M. Pintado, Catal. Today, 23 (1995) 219-250.

[122] M. Abid, V. Paul-Boncour, R. Touroude, Appl. Catal. A Gen., 297 (2006) 48-59.

[123] J. Zhu Chen, A. Talpade, G.A. Canning, P.R. Probus, F.H. Ribeiro, A.K. Datye, J.T. Miller, Catal. Today, 371 (2021) 4-10.

[124] S.E. Golunski, H.A. Hatcher, R.R. Rajaram, T.J. Truex, Appl. Catal. B Environ., 5 (1995) 367-376.

[125] A. Trovarelli, F. Zamar, J. Llorca, C.d. Leitenburg, G. Dolcetti, J.T. Kiss, J. Catal., 169 (1997) 490-502.

[126] M. Ozawa, M. Kimura, A. Isogai, J. Alloys Compd., 193 (1993) 73-75.

[127] E. Mamontov, T. Egami, R. Brezny, M. Koranne, S. Tyagi, J. Phys. Chem. B, 104 (2000) 11110-11116.

초 록

배기가스에 포함된 오염물질을 저감하는 것은 가장 중요한 사회적 문제 가운데 하나이다. 이에 따라 전 세계적으로 배기가스 배출 관련 규제가 강화되고 있다. 이러한 엄격한 규제를 충족시키기 위해서 다양한 후처리 촉매 전환 기술들이 개발되어 사용되고 있다. 일반적으로 가솔린 엔진 후처리 시스템에는 삼원촉매(TWC)와 같은 촉매 변환장치가 사용되고 디젤 엔진 후처리 시스템에서는 디젤산화촉매(DOC)와 선택적 촉매 환원(SCR)같은 기술들이 사용된다. 그러나 이러한 후처리 시스템이 정상적으로 작동하기 위해서는 일정 수준 이상의 온도(일반적으로 200 °C 이상)가 유지되어야 한다. 따라서 상온에 있던 차량에서 처음 시동을 걸 때는 촉매 전환을 거치지 않은 질소산화물(NOx), 프로펜 등의 오염물질이 다량으로 배출되어 냉간 시동 배출가스가 발생하게 된다.

디젤 엔진 운전 시에 냉간 시동 구간에서의 NOx 배출 문제를 해결하기 위한 유망한 촉매 기술 가운데 하나로 Passive NOx adsorber (PNA)가 제안되어 연구되고 있다. PNA는 저온에서 NOx를 흡착하고 고온에서 NOx를 방출하여 후단에 있는 후처리 시스템이 정상적으로 기능하도록 한다. 이와 유사하게, 제올라

이트를 기반으로 한 저온 탄화수소 트랩의 개발이 활발하게 진행되고 있다. 대부분의 연구는 디젤 엔진에 적용하기 위한 응용을 대상으로 진행되고 있다. 가솔린 엔진의 배기가스는 디젤과 운전 방식, 온도, 조성 등이 다르기 때문에 내구성 측면에서 제올라이트를 효과적으로 적용하기 어렵고, 따라서 가솔린 엔진에 적용하기 위한 저온 촉매 개발이 필요하다.

먼저 저온에서 일산화탄소(CO)가 Pd/CeO_2 촉매의 NOx 흡착 능력을 증진하는 효과를 조사하였다. CO가 배기가스에 첨가되었을 때 흡착된 NOx의 양이 상당히 증가하였다. 구체적으로, 처음 10분 동안 CO가 있을 때 NOx 흡착량이 6배 이상 증가하였다. NOx 흡착량이 증가함에 따라 CO 산화 능력이 감소하는 결과로부터 저온 NOx 흡착에 대한 CO의 증진 효과에 대한 모델을 제안하였다. CO와 NO 상호작용에 대한 더 나은 이해는 CeO_2 기반 저온 NOx 흡착 물질 개발에 이바지할 것으로 기대된다.

다음으로, 가솔린 차량에서 거의 무배출에 가까운 NO 배출량을 달성하기 위해 CeO_2-지지 Pd 촉매가 고안되었다. 삼원촉매를 작동 온도 (>200° C)로 예열하는 동안 선진 기술의 가솔린 차량에서 상당한 양의 NO가 방출된다. Pd 나노입자(NP)를 CeO_2에 담지하여 냉간 시동 구간에서 NO 배출을 완화하기 위한 NO 저감

물질로 연구하였다. 공연비를 냉간 시동 구간에서 시스템적으로 점차 높은 값에서 낮은 값으로 조절하면 삼원촉매의 작동 온도 이하에서는 NO 저장을 촉진하고 고온에서는 NO 환원 반응을 촉진할 수 있다는 결과를 도출하였다. 실험 결과와 계산화학 연구 결과를 결합하여 V_O에 의해 개질 된 Pd-NP-CeO_2 계면이 NO*를 NO_2로 전환하는 데 중요한 역할을 한다는 결과를 제시하였다. NO_2는 CeO_2 표면에 형성된 V_O에 의해 포착되어 Pd/CeO_2를 NO 저장 물질로 사용할 수 있게 된다. 결과적으로 기존 삼원촉매만으로는 달성할 수 없었던 작동 조건에서 냉간 시동 구간에서의 NO 배출이 67.6% 감소하여 유해가스 무배출에 한걸음 더 다가설 수 있었다.

마지막으로 미연소 탄화수소에 대한 향후 규제에 대응하기 위해 가솔린 엔진에 사용할 수 있는 저온 프로펜 배출 저감 용도로 Pd/CeO_2 적용할 수 있는 가능성을 검토하였다. 프로펜은 가솔린 엔진 배기가스에서 가장 대표적인 미연소 경량 탄화수소 중 하나이다. 실험 및 특성화 데이터를 고려하여 Pd/CeO_2 표면에 대한 프로펜 흡착 메커니즘을 제안하였다. 또한 Ce-Zr 혼합 산화물을 도입하여 열적 안정성을 향상했다. 엔진 바로 뒤에 위치한 트랩의 특성상 높은 열적 안정성이 요구되기 때문이다.

본 논문에서는 Pd/CeO_2 촉매를 이용하여 저온에서 NOx와 프로펜을 효과적으로 저장하는 방법과 Pd와 CeO_2의 역할을 규명하였다. 또한, 이러한 발견을 바탕으로 고온 환원 분위기에서 안정성이 더 우수한 촉매를 설계하였다. 이 연구를 통해 저온 배출을 다루는 차세대 후처리 시스템 개발에 기여할 수 있을 것으로 기대된다.

주요어: 질소산화물; 경질 탄화수소; Pd/CeO_2; 냉간 시동 배기가스; 흡착자리; 후처리 장치

학번: 2017-28948